Title
Heat Transfer in Graphene and Anisotropic/Nonlinear Systems: Experimental and Theoretical Studies

Author
Chen, Zhen

Publication Date
2014

Peer reviewed|Thesis/dissertation

Heat Transfer in Graphene and Anisotropic/Nonlinear Systems: Experimental and Theoretical Studies

By

Zhen Chen

A dissertation submitted in partial satisfaction of the

Requirements for the degree of

Doctor of Philosophy

in

Engineering - Mechanical Engineering

in the

Graduate Division

of the

University of California, Berkeley

Committee in charge:

Professor Chris Dames, Chair

Professor Costas Grigoropoulos

Professor Zi Q. Qiu

Spring 2014

Heat Transfer in Graphene and Anisotropic/Nonlinear Systems:

Experimental and Theoretical Studies

Zhen Chen

Abstract

Heat Transfer in Graphene and Anisotropic/Nonlinear Systems:

Experimental and Theoretical Studies

by

Zhen Chen

Doctor of Philosophy in Engineering - Mechanical Engineering

University of California, Berkeley

Professor Chris Dames, Chair

Various modern devices involve highly anisotropic materials. For example, Bi_2Te_3 is used in thermoelectrics, and graphene finds broad applications ranging from microelectronics to optoelectronics. The heat transfer in these materials can deviate significantly from classical isotropic transport theory. Nonlinear thermal devices have also drawn a great deal of attention for such applications as thermal regulation of building envelopes, and thermal protection of delicate components in electrical hardware, spacecraft thermal shielding, and satellite radiators.

In this thesis, heat transfer in nonlinear devices and anisotropic materials, in particular graphene, is investigated using both experimental and theoretical methods. Measurements on graphene sheets encased by silicon dioxide layers show the strong effect of the encasing oxide in disrupting the thermal conductivity of adjacent graphene layers, leading to more than one order of magnitude suppression as compared to the freely-suspended graphene experiment reported in literature. Modeling thermal properties of anisotropic materials reveals an unexpected guideline to engineer heat transport: due to phonon focusing effects, in many cases the heat transfer can be enhanced by reducing a phonon velocity component perpendicular to the transport direction. Finally, a nonlinear thermal diode, based on a new mechanism exploiting asymmetric scattering of ballistic energy carriers by pyramidal reflectors, is demonstrated experimentally. Experiments underline that all thermal rectifiers require nonlinearity in addition to asymmetry.

Table of Contents

List of Figures

List of Tables

Acknowledgements

This thesis places a full stop to a seven-year-journey in pursuing my PhD, which starts at UC Riverside and ends here at UC Berkeley. I use this opportunity to thank the many people who have helped along the long journey.

It's my great fortune to be the first PhD student of Professor Chris Dames, so that I had the opportunity to learn his research style at first hand, especially during the UC Riverside period. I have great respect for his insistence on doing solid work, his critical thinking, his attitude to appreciate other people's work, and his patience in training students. I hope to use these values in my future career. I am also grateful to Professor Zi Q. Qiu for teaching me the importance of physical pictures in research. I would like to thank Professor Grigoropoulos for serving in both my qualifying exam and dissertation committee.

I have benefited a great deal from both the formal and informal discussions with my labmates at Berkeley. In particular, I enjoyed building experiment with Shannon Yee, talking physics with Sean Lubner, taking Quantum Mechanics with Vivek Mishra, and solving heat conduction equations with Geoff Wehmeyer.

I would not have been able to finish my PhD if it were not for my family. In particular, my father gave me unusual freedom, love, and support as I grew up. Xiaodong loved me unconditionally. She sacrificed her career in China in order for me to pursue my PhD in US. Most importantly, she gave birth to Niels, who has the magic power to make me forget anything unhappy. I love you all, and you are the reason I look forward to every day.

Chapter 1: Introduction

This thesis covers three major topics: thermal properties of graphene, heat transfer in highly anisotropic materials, and a photon thermal diode. At first sight, these three topics may appear independent of each other. We will show in the following chapters that they are closely related, and indeed form a complete and logical story. In short, the theoretical work of the heat transfer in anisotropic materials is motivated by the experimental work on the thermal properties of graphene which itself is a highly anisotropic material. The photon thermal diode is a device built to study nonlinear heater transfer, which, of course, transports thermal energy anisotropically as well.

This chapter gives a very brief and broad survey to all the three topics, leaving the detailed technical literature review to the following designated chapters.

1.1 Graphene

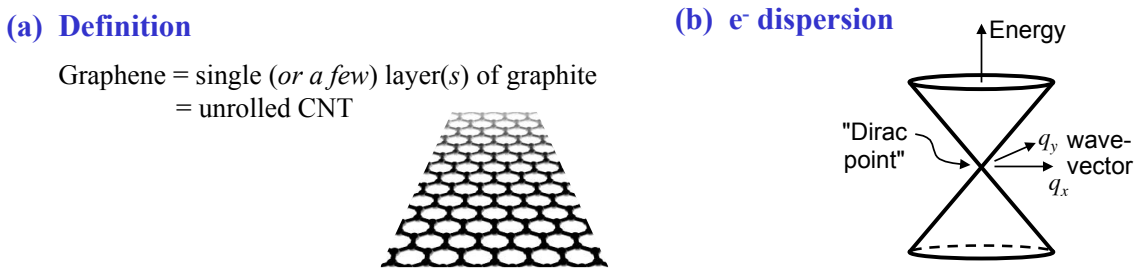

Figure 1-1. Introduction to graphene.

Graphene is a single- or few-layer graphite sheet, or an unrolled carbon nanotube [Fig. 1-1(a)]. The theoretical study of graphene can be traced back to the 1940s [1-3]. However, experimental study has lagged far behind due to the great difficulties in preparing graphene samples. The breakthrough was made in 2004 by Novoselov and Geim who successfully isolated and measured single-layer graphene on insulating substrates [4], which enabled a rapid exponential growth in graphene research.

Graphene has attracted a great deal of interest from researchers studying both fundamental physics and industrial applications. On the fundamental side, due to a linear instead of the normal parabolic electron dispersion relationship [Fig. 1-1(b)], graphene is a prototype system to study "massless," pseudo-relativistic electrons. On the application side, due to its superior electrical [5-6] and thermal properties [7-8], graphene is a promising candidate for transparent electrodes for displays and optoelectronic devices. Key challenges include opening an adequate band gap, and preparing large wafer-scale graphene flakes.

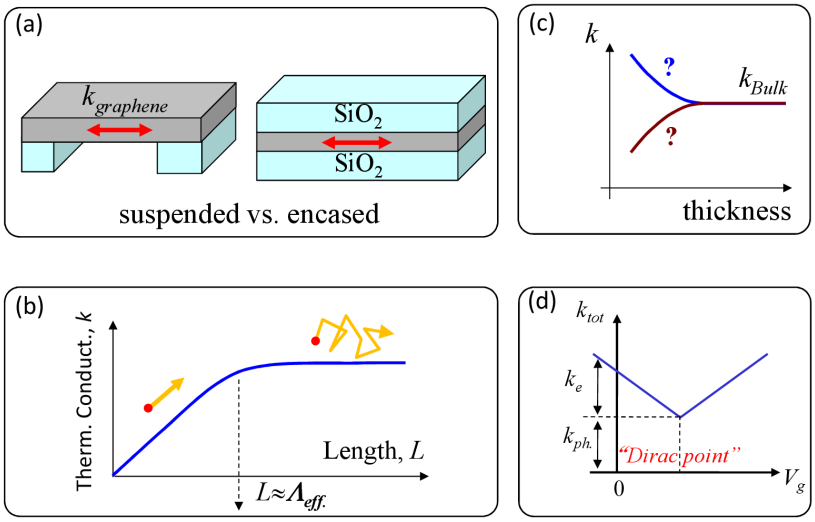

Figure 1-2. Proposed studies on graphene. (a) Suspended vs. encased. (b) Ballistic vs. diffusive transport. (c) Thickness dependence of *k*. (d) Electron vs. phonon contribution. (a) and (c) are pursued in this thesis, (b) and (d) are left for future.

In response to these fundamental and application interests, many questions need to be addressed. This thesis will focus on the following heat transfer aspects, in which A, B, and E will be addressed in Chapter 2, and C and D are left for future research directions.

A. Effect of dielectric layers on the thermal conductivity of graphene (k_g). While physicists are more interested in freely-suspended graphene (and often at very low temperature), which is an exceedingly simple and clean structure to study the fundamental physics of electrons, engineers care more about industrial applications in which graphene is usually encased by dielectric layers [Fig. 1-2(a)]. Intuitively, this encased structure will impose extra constraints on the thermal transport, but we need a quantitative experiment confirmation.

B. Length/width dependence of k_g. As indicated in Fig. 1-2(b), the energy carrier transitions from diffusive to ballistic behavior as the characteristic length/width approaches the dominant mean free path (MFP) of the carrier. Due to the high thermal conductivity of freely-suspended graphene (1000s W/m-K), the dominant MFP of graphene is thought to be in the micron range [7-8], making it possible to observe this diffusive-ballistic transition even at room temperature.

C. Thickness dependence of k_g. The thermal conductivity must recover the bulk graphite limit as the number of layers is increased, both for freely-suspended and encased graphene. The question is how this bulk limit is approached [Fig. 1-2(c)], and if there is any difference between the two scenarios.

D. Electron vs. phonon contributions to k_g. Phonons dominate the heat transfer at room temperature. However, electrons gradually manifest themselves as temperature decreases, especially if a back/top gate is applied to manipulate the sample's electrochemical potential E_F.

E. Thermal contact between graphene and dielectric layers. This parameter is especially important for industrial applications, in which graphene would need to interact with dielectrics.

1.2 Anisotropic heat transfer

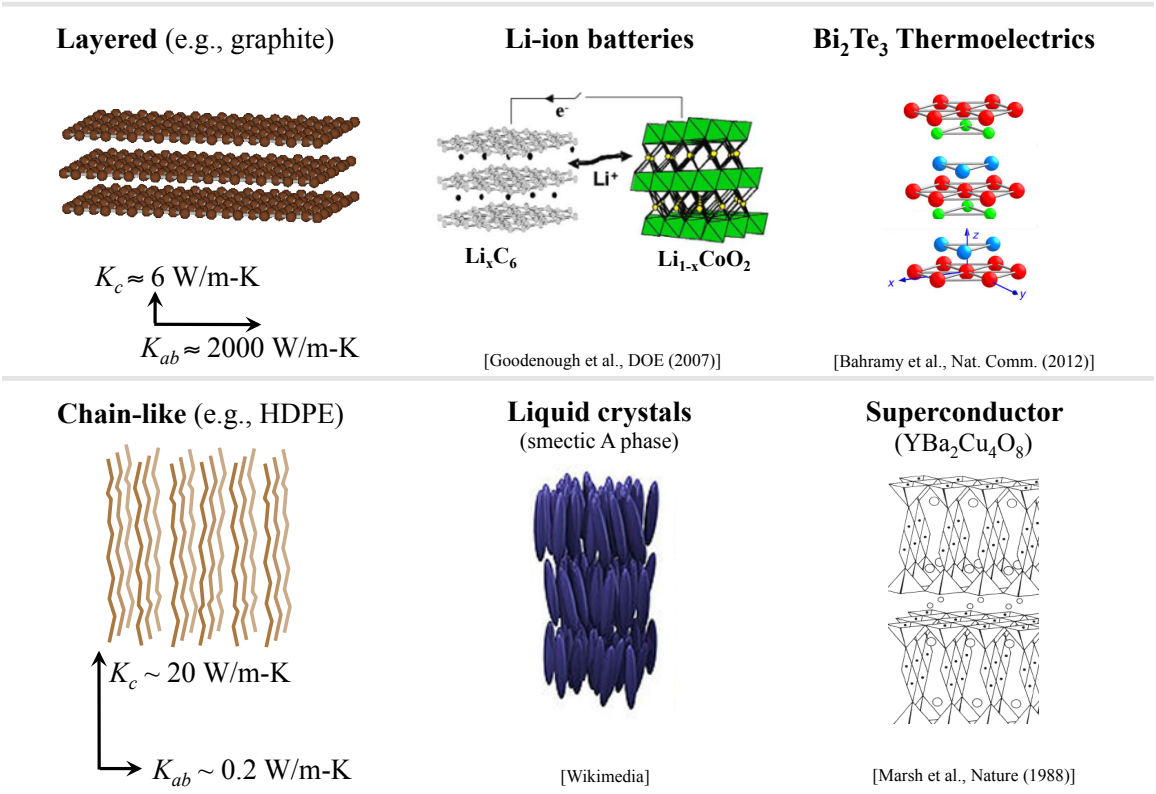

Figure 1-3. Important anisotropic materials.

As shown in Fig. 1-3, many important materials are highly anisotropic. For example, graphite is a typical layered material, as are the Li-ion battery material Li_xC_6 and $Li_{1-x}CoO_2$, and the popular thermoelectric material Bi_2Te_3. High density polyethylene, liquid crystal (smectic A phase), and the famous superconducting material $YBa_2Cu_4O_8$ are well-known chain-like materials.

Before introducing our general framework to model the heat transfer in anisotropic materials, it's desirable to revisit some of the fundamental principles:

A. Onsager's reciprocal relation [9]: the conductivity matrix is symmetric no matter how the axes are aligned, which is a manifestation of the more fundamental principle of time reversal symmetry.

B. Neumann's Principle [10]: the conductivity tensor must be *at least* as symmetric as the crystal. For example, silicon has cubic symmetry in crystal structure, and its sound velocities vary with direction. Yet the thermal conductivity of silicon is isotropic.

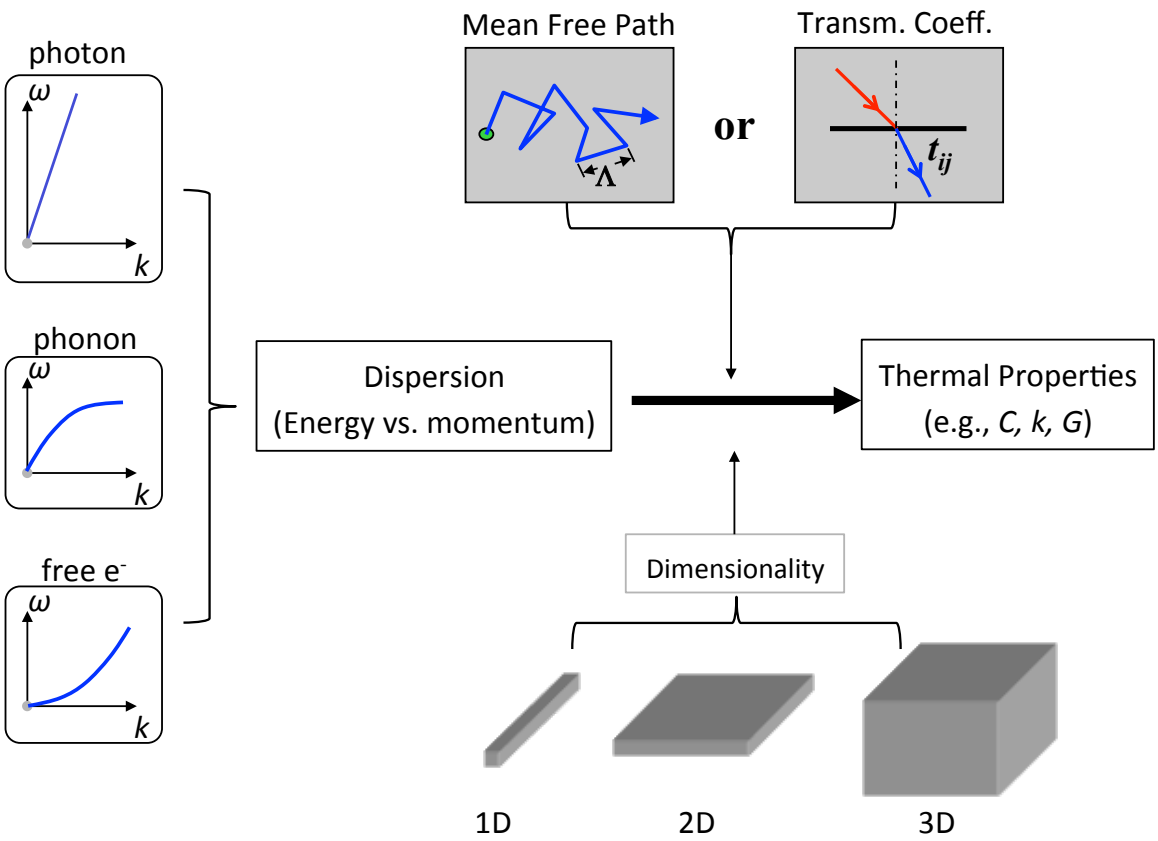

Figure 1-4. Flowchart for modeling thermal properties.

As indicated in Fig. 1-4, the dispersion, i.e., the energy-momentum relation, of a specific energy carrier (*e.g.* photon, phonon, electron) is the central information to model any thermal properties. From the dispersion relation, we can extract the group velocity of the energy carrier, the density of states (if the dimensionality is known), and thus the heat capacity (C). To model the thermal conductivity (k), we need a second piece of information, which is the scattering mechanisms that give the mean free path (MFP) of the carrier. Likewise, we need the transmission coefficient (t_{ij}) to model the thermal boundary conductance (G).

This thesis will discuss in detail how to model C and G of anisotropic materials in Chapter 3, and leave k for future research directions.

1.3 Nonlinear thermal devices

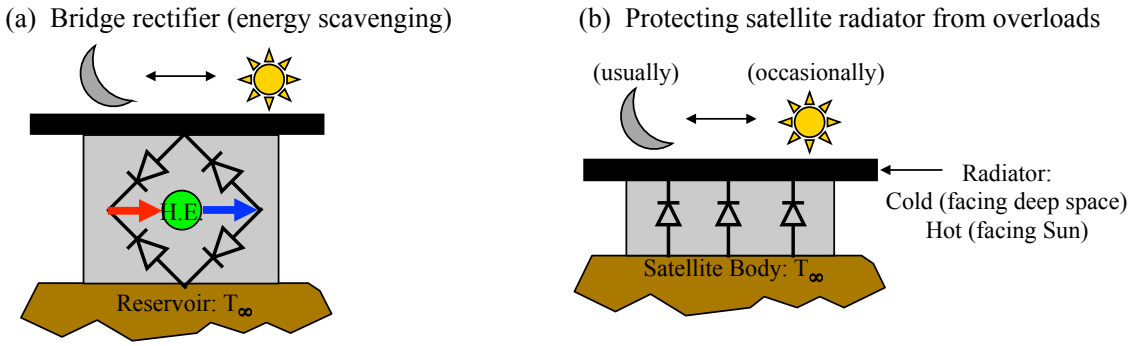

Figure 1-5. Proposed application of thermal diodes.

The great success of electrical engineering can partially be attributed to the capability of controlling electrical flux nonlinearly. By contrast, thermal engineering still relys on the linear thermal elements, namely thermal resistors (R) and capacitors (C). It is desirable to control heat flux in a nonlinear manner, both passively and actively.

The most fundamental *passive* nonlinear thermal element would be a thermal diode: a two-terminal device that transmits heat more easily in one direction than in the reverse direction would be the heat-transfer analogue to the familiar electrical diode. Highly-effective thermal rectifiers could find numerous applications in thermal engineering. For example, in solar-thermal power, a temperature doubler [analogous to a voltage doubler; see Fig. 1-5(a)] can exploit nighttime cold temperatures as well as daytime highs to increase the average temperature difference driving a heat engine, increasing both efficiency and power output [11-12]. A thermal diode's clamping functionality could be useful for thermal regulation of building envelopes [13], as well as thermal protection of delicate components in electrical hardware, spacecraft thermal shielding, and satellite radiators [Fig. 1-5(b)].

The most fundamental *active* nonlinear thermal element would be a thermal transistor: a three-terminal device that controls the thermal conductivity of a channel. Due to the active nature, a thermal transistor would have more degrees of control in thermal engineering than a passive thermal diode. For example, a feedback mechanism could be built up through the gate terminal of the thermal transistor so the amount of heat that is dissipated or acquired through the satellite radiators could be accurately controlled [imagine the thermal diodes in Fig. 1-5(b) are replaced with thermal transistors].

We should note that these nonlinear thermal devices might never be as efficient as their electrical counterparts, which is due to the fact that the *thermal* conductivity of solids spans less than five orders of magnitude, while the *electrical* conductivity spans more than twenty orders of magnitude.

This thesis will experimentally demonstrate a passive thermal diode in Chapter 4, and leave the active thermal transistor for future research directions.

1.4 Outline of the thesis

This thesis is broadly concerned with heat transfer in anisotropic and nonlinear systems, from both experimental and theoretical perspectives.

Chapter 2 measures the thermal properties of graphene encased by silicon dioxide layers. A heat spreader method is developed and verified, and finally applied to measure the thermal conductivity of graphene. A differential 3ω method is adapted to measure the thermal contact resistance between graphene and silicon dioxide.

Chapter 3 develops a general framework to model the thermal properties of anisotropic materials. The model is compared with experimental results of specific heat and thermal boundary conductance for typical layered and chain-like materials.

Chapter 4 experimentally demonstrates a photon thermal diode. The measurements underline the two key ingredients, the asymmetry and the nonlinearity, to any thermal rectification mechanism.

Finally Chapter 5 summarizes the contribution of this thesis and suggests some interesting directions for future research.

1.5 References

[1] P. R. Wallace, The band theory of graphite, *Phys. Rev.* **71**, 622–634 (1947).

[2] J. W. McClure, Diamagnetism of graphite, *Phys. Rev.* **104**, 666–671 (1956).

[3] J. C. Slonczewski, P. R. Weiss, Band structure of graphite, *Phys. Rev.* **109**, 272–279 (1958).

[4] K. S. Novoselov *et al.*, Electric field effect in atomically thin carbon films., *Science* **306**, 666–9 (2004).

[5] Bolotin *et al.*, Ultrahigh electron mobility in suspended graphene, *Sol. St. Commun.* **146**, 351-355 (2008).

[6] R. Murali, Y. Yang, K. Brenner, T. Beck, J. D. Meindl, Breakdown current density of graphene nanoribbons, *Appl. Phys. Lett.* **94**, 243114 (2009).

[7] A. A. Balandin *et al.*, Superior thermal conductivity of single-layer graphene., *Nano Lett.* **8**, 902–7 (2008).

[8] N. Mingo, D. A. Broido, Length Dependence of Carbon Nanotube Thermal Conductivity and the "Problem of Long Waves," *Nano Lett.* **5**, 1221–1225 (2005).

[9] L. Onsager, Reciprocal Relations in Irreversible Processes. I., *Phys. Rev.* **37**, 405–426 (1931).

[10] R. E. Newnham, *Properties of Materials: Anisotropy, Symmetry, Structure* (Oxford University Press, New York, 2005).

[11] Y. Yan, J. A. Malen, Periodic heating amplifies the efficiency of thermoelectric energy conversion, *Energy Environ. Sci.* **6**, 1267–1273 (2013).

[12] J. Miller, W. Jang, C. Dames, Thermal rectification by ballistic phonons in asymmetric nanostructures*2009 ASME Summer Heat Transf. Conf.* (2009).

[13] S. Varga, A. C. Oliveira, C. F. Afonso, Characterisation of thermal diode panels for use in the cooling season in buildings, *Energy Build.* **34**, 227–235 (2002).

Chapter 2: Thermal properties of encased graphene

2.1 Introduction

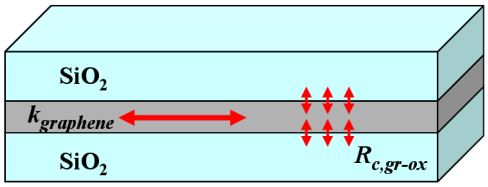

This portion of the thesis investigates the heat transfer properties of graphene encased by silicon dioxide layers. The first half of the chapter develops a heat spreader method to measure the thermal conductivity of graphene and ultrathin graphite (thickness from 1 to ~20 layers) encased within silicon dioxide. The thermal conductivity increases with the number of graphene layers, approaching the in-plane thermal conductivity of bulk graphite for the thickest samples, while showing suppression below 160 W/m-K at room temperature for single-layer graphene. These results show the strong effect of the encasing oxide in disrupting the thermal conductivity of adjacent graphene layers, an effect that penetrates a characteristic distance of approximately 2.5 nm (~7 layers) into the core layers at room temperature. The second half of the chapter adapts a differential 3ω method to measure the thermal contact resistance between graphene and silicon dioxide. The sample thicknesses are 1.2 nm (single-layer graphene), 1.5 nm, 2.8 nm, and 3.0 nm, as determined by atomic force microscopy. All samples exhibits approximately the same temperature trend from 42 K to 310 K, with no clear thickness dependence. The contact resistance at room temperature ranges from 5.6×10^{-9} to 1.2×10^{-8} m^2-K/W, which is significantly lower than previous measurements involving related carbon materials. These results underscore graphene's potential for applications in microelectronics and thermal management structures.

This chapter is based very closely on our previous publications [1, 2], but includes more details and justifications.

2.2 Thermal conductivity

Among graphene's many remarkable properties [3], its expected very high thermal conductivity k has been suggested as a key advantage for applications in microelectronics and thermal management. Using a Raman method for both heating and temperature sensing [4], the thermal conductivity of suspended single-layer graphene (SLG) has been measured in the range ~600 to ~5000 W/m-K near and above room temperature [4-6], far higher than the k of copper (~400 W/m-K). Although the variations in the reported optical absorbance remain to be clarified [4-6], these results suggest that suspended SLG has a k comparable to, if not exceeding, its very high-k carbonaceous cousins – including graphite (1950 W/m-K in-plane [7]), diamond (2310 W/m-K [7]), and suspended carbon nanotubes (up to ~3400 W/m-K for μm-length tubes, according to modeling [8] and experiments [9-13]).

However, in most practical devices, graphene layers will be encased within dielectrics such as silicon dioxide, and it is essential to understand how this boundary interaction impacts thermal transport. Although traditional analysis of the in-plane k of

thin films ignores the distinction between suspended and supported boundaries [14-15], recent measurements of SLG with one face supported on a substrate show that k is greatly reduced, to ~50 - 1020 W/m-K on copper (Raman method [6]), or ~600 W/m-K on SiO_2 (suspended platform method [16]). In contrast to suspended SLG, these values fall far below the in-plane k of bulk graphite [7], demonstrating the great importance of free vs. supported boundaries.

Here we present the first measurements of graphene and ultrathin graphite ($1 \leq N_{Layers} \leq$ ~20) in an encased configuration. The results show that the encasing SiO_2 further reduces k well below that of supported graphene. Furthermore, these experiments capture the thickness-dependent transition from SLG to bulk graphitic behavior, and imply that the surface-induced disruptions of k penetrate into the neighboring graphene layers by a characteristic distance of 2.5 nm (7 layers) at room temperature.

2.2.1 Physical picture and heat transfer models

A. Graphene as a heat spreader

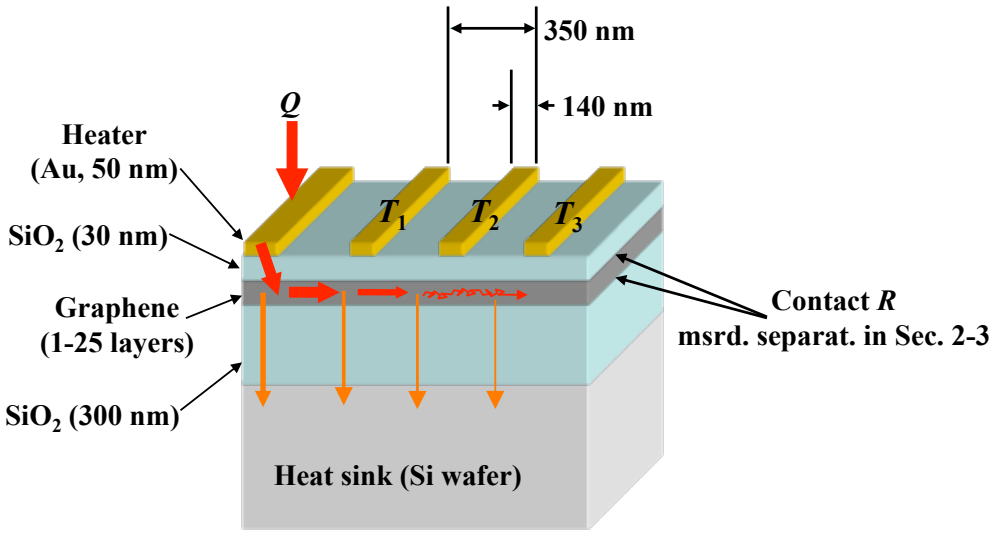

Figure 2-1. Schematic of the "heat spreader method" to measure k for graphene encased between top and bottom SiO_2 films. Heat flows (red arrows) through the encased graphene and into the Si heat sink.

Figure 2-1 shows a schematic of the heat spreader method developed in this work to measure the in-plane k of encase graphene. The graphene thin film is encased between top and bottom oxide layers, a configuration which is very relevant to microelectronics applications, where graphene layers might be used as the transistors, interconnects, and thermal management materials, all encased by SiO_2 dielectric layers. The silicon substrate acts as a heat sink. A heater and three temperature sensors are microfabricated on top of the upper oxide layer, which is used to electrically isolate these electrodes from the graphene. A metallic line heater dissipates Joule heat at a rate Q_H, which flows vertically through the stack into the Si heat sink, while simultaneously spreading laterally

through the high-k graphene layer. Compared to a control experiment with no graphene layer, the configuration in Fig. 2-1 results in higher temperatures at the sensors T_1 - T_3. Finally, k of the graphene layer is inferred by fitting 3 measured experimental quantities (temperature rise per unit heater power, for sensors T_1, T_2, and T_3) to a thermal model.

B. One, two, and three dimensional heat transfer models

We model the heat transfer in this encased graphene structure (Fig. 2-1) under the framework of the classic heat conduction, namely the heat diffusion equation. This assumption is adjusted in Section 2.2.4E. We start with a simple one dimensional (1D) model for physical insight, and end with a sophisticated three dimensional (3D) model to extract the thermal conductivity of graphene.

1D fin: simplistic but insightful

The simplest thermal model is to treat the graphene heat spreader as a "1D fin," where the effective "convection" coefficient h_{eff} represents the vertical conduction through the lower SiO_2 layer into the Si heat sink. The interfacial contact resistances are also important. Thus,

$$h_{eff} = \left(t_{ox} / k_{ox} + R''_{c,gr-ox} + R''_{c,ox-Si} \right)^{-1} \tag{2-1}$$

where k_{ox} and t_{ox} are the thermal conductivity and thickness of the lower oxide layer, and the two R''_c terms are the specific contact resistances (m^2-K/W) from graphene-to-oxide and from oxide-to-silicon, respectively. We note that $R''_{c,ox-Si}$ has been previously measured (~2x10^{-8} m^2-K/W at 300 K [17]), but $R''_{c,gr-ox}$ has not. This latter quantity is particularly important for graphene microelectronics applications, and will be measured separately in Section 2.3.

This simplified fin model gives good insight into the major measurement issues. As a first approximation, we neglect the R''_c terms, and using t_{ox} = 300 nm we estimate h_{eff} = 4x10^6 W/m^2K. Using textbook fin theory, we estimate the characteristic fin length (also known as the thermal healing length [50]), $m^{-1} = \sqrt{kA_c / h_{eff} P}$, where A_c and P are the cross sectional area and "wetted perimeter" of the graphene fin. For a flake of thickness t, and width w out of the page in Fig. 2-1, the ratio A_c/P is simply t. Thus, the characteristic fin length is

$$m^{-1} = \sqrt{kt / h_{eff}}\ , \tag{2-2}$$

which ranges from ~0.5 μm for single layer graphene (t = 0.34 nm) to ~1.5 μm for 10 layer graphene (t = 3.4 nm), assuming k~3000 W/m-K [4, 8, 18-20]. Thus, the extent of lateral heat spreading is expected to be roughly a few microns. However, as shown below, it turns out that the thermal conductivity of graphene is more than 1 order of magnitude smaller than the assumed 3000 W/m-K. This violates the criterion, $m^{-1} >> t_{ox}$ required to use the fin analogy. Therefore, in this work we use the fin model as a helpful qualitative guide to the measurement issues, but not for quantitative analysis.

2D models: SOV vs. FEM

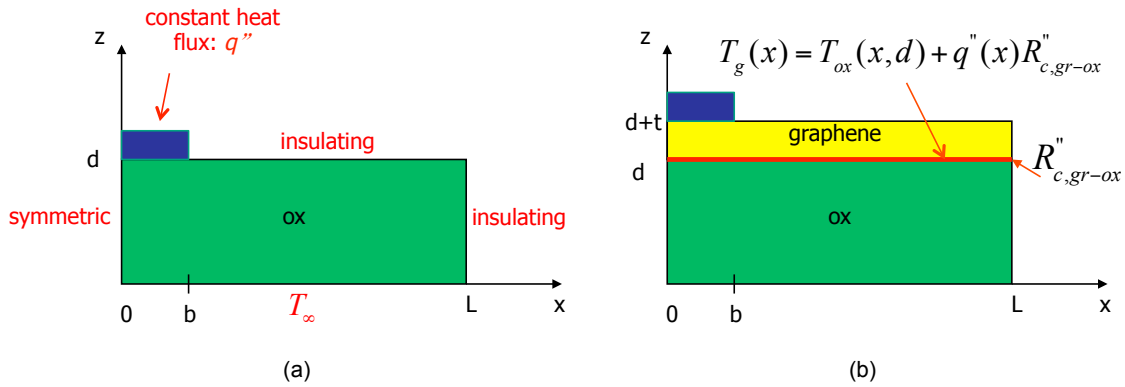

Figure 2-2. Boundary conditions for the 2D analytical model solved using separation of variables. (a) Step 1: solving the temperature field of the bottom oxide, $T_{ox}(x,z)$. (b) Step 2: solving the temperature field of graphene, $T_g(x)$. The thermal boundary resistance, $R_{c,gr-ox}$, also included.

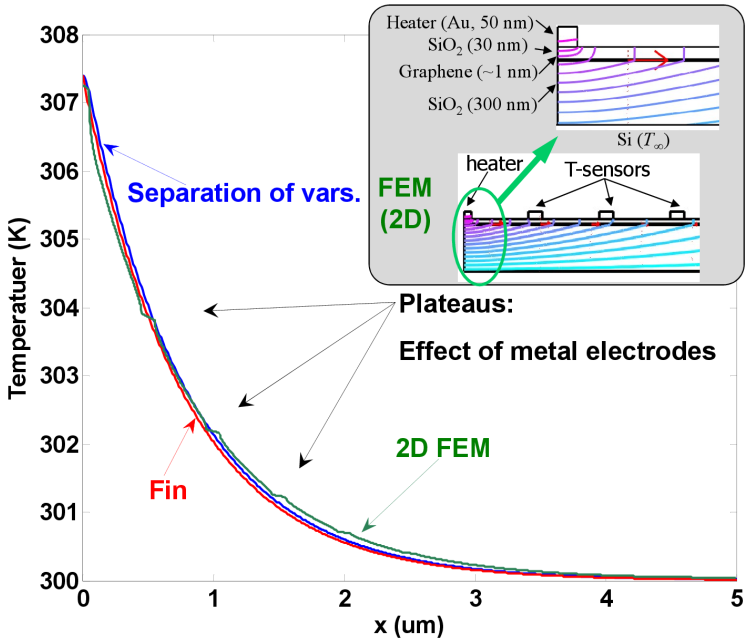

Figure 2-3. Typical *T* profiles along a graphene film calculated by three different models: 1D fin, 2D SOV, and 2D FEM, all of which assume perfect Si heat sink. Inset: detail of the 2D FEM calculations.

A slightly improved model is a 2D calculation implemented using separation of variables (SOV). We solve this problem in two steps. First, we solve the 2D Laplace equation $\frac{\partial^2 T}{\partial x^2} + \frac{\partial^2 T}{\partial z^2} = 0$ with boundary conditions indicated in Fig. 2-2(a), to obtain the 2D temperature field of the bottom oxide:

$$T_{ox}(x,z) = T_\infty + \frac{q'' b}{k_{ox} L} z + \frac{2q''}{k_{ox} L} \sum_{m=1}^{\infty} \frac{\sin(\beta_m b)}{\beta_m^2 \cosh(\beta_m d)} \sinh(\beta_m z) \cos(\beta_m x), \quad (2\text{-}3)$$

where q'' is the heat flux with unit W/m^2, b is the half width of the heater line, d and L are the thickness and length of the bottom oxide, respectively, and the eigenvalue $\beta_m = \frac{m\pi}{L}, m = 1,2,3,...$

Second, we add the graphene thin film and $R''_{c,gr-ox}$ [Fig. 2-2(b)]. An infinitesimal control volume on graphene results in an energy balance as $q'' - k_{ox} \left.\frac{\partial T_{ox}}{\partial z}\right|_{z=d} + k_g t \left.\frac{\partial^2 T_g}{\partial x^2}\right|_{z=d} = 0$, where $T_g(x) = T_{ox}(x,d) + R''_{c,gr-ox} k_{ox} \left.\frac{\partial T_{ox}}{\partial z}\right|_{z=d}$. Thus the resulting temperature of graphene is

$$T_g(x) = T_\infty + \frac{q'' b}{k_{ox} L} d + \frac{q'' b}{L} R''_{c,gr-ox} + \frac{2q''}{L} \sum_{m=1}^{\infty} \frac{\sin(\beta_m b)[\sinh(\beta_m d) + \beta_m R''_c k_{ox} \cosh(\beta_m d)]}{\beta_m^2 [k_g t \beta_m \sinh(\beta_m d) + k_g t R''_c k_{ox} \beta_m^2 \cosh(\beta_m d) + k_{ox} \cosh(\beta_m d)]} \cos(\beta_m x) \quad (2\text{-}4)$$

Note the top oxide and metal electrodes are neglected for simplicity in this SOV method.

To account for the effect of the top oxide and the metal electrodes, we have also implemented a 2D finite-element method (FEM). As shown in Fig. 2-3, the three methods agree within 1% with each other. Also note from the inset of Fig. 2-3 that within the lower oxide the temperature gradients in the cross-plane direction are significantly steeper than the gradients in the in-plane direction, supporting the use of the fin model. The FEM calculations account for the effect of the metal electrodes in causing local spatial averaging ("plateaus") of the temperature.

3D FEM: all details

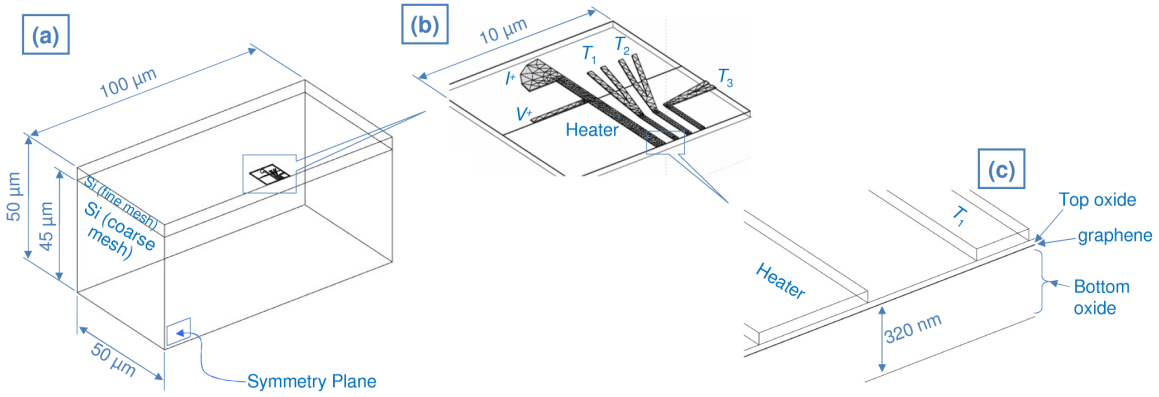

Figure 2-4. A typical 3D FEM model. For clarity, the mesh is only shown in (b), and only for the electrodes.

The simple 2D models above turn out to be too crude, because they assume the Si substrate has infinite *k* and also neglect the geometric variations out-of-the-page. Finally, we have to set up a 3D FEM model using a commercial software package (COMSOL). A typical simulation domain is shown in Fig. 2-4. A heat flux boundary condition is applied on the top surface of the heater's active length to represent Joule heating, while the rest of the top surfaces are treated as insulated. The symmetry plane that bisects the region of interest is also treated as insulated. The bottom face and three side faces of the silicon substrate domain are held at ambient temperature, to approximate the far-field conditions of the true Si wafer. This is justified because the typical size of the central heater region that dominates the total Joule heating is ~10 μm long. From well-known solutions for the 3D spreading resistance of small heat source into a semi-infinite 3D substrate [21], such a problem can always be accurately approximated with a finite substrate as long as the characteristic substrate dimensions are all much larger than the heater dimensions. We simulated a range of substrate sizes to confirm that the final model results were independent of the simulated substrate size. Analogous optimizations were performed to quantify the length of the oxide layers and metal leads (of heater and *T* sensors) that were required to be included in the simulation domain.

Additional computational optimization focused on meshing. Due to the extreme ratio of the graphene film thickness (~1 nm) to its typical in-plane dimensions (~10 μm), as well as for reasons of computational efficiency, this system is more easily optimized using a swept mesh strategy rather than the typical free mesh. Note also from Fig. 2-4(a) that the upper 5 μm of the Si substrate were meshed finely while the lower 45 μm were meshed coarsely. We confirmed the calculations in this work are fully converged by comparing results from different mesh sizes and meshing strategies (swept vs. free).

In summary, these simulations include known 3D geometries (graphene flake, heater, *T* sensors, oxide layers, and at least $(50\ \mu m)^3$ of the Si substrate), thermal conductivities (top and bottom oxide layers, Si substrate, and metal electrodes), and the thermal contact resistance between graphene and SiO_2, which is measured in Section 2-3 Each FEM-simulated sensor temperature takes into account the local *T* averaging caused by the finite sensor width. The results are only sensitive to the in-plane (rather than cross-plane) *k* of the encased flake.

2.2.2 Microfabrication

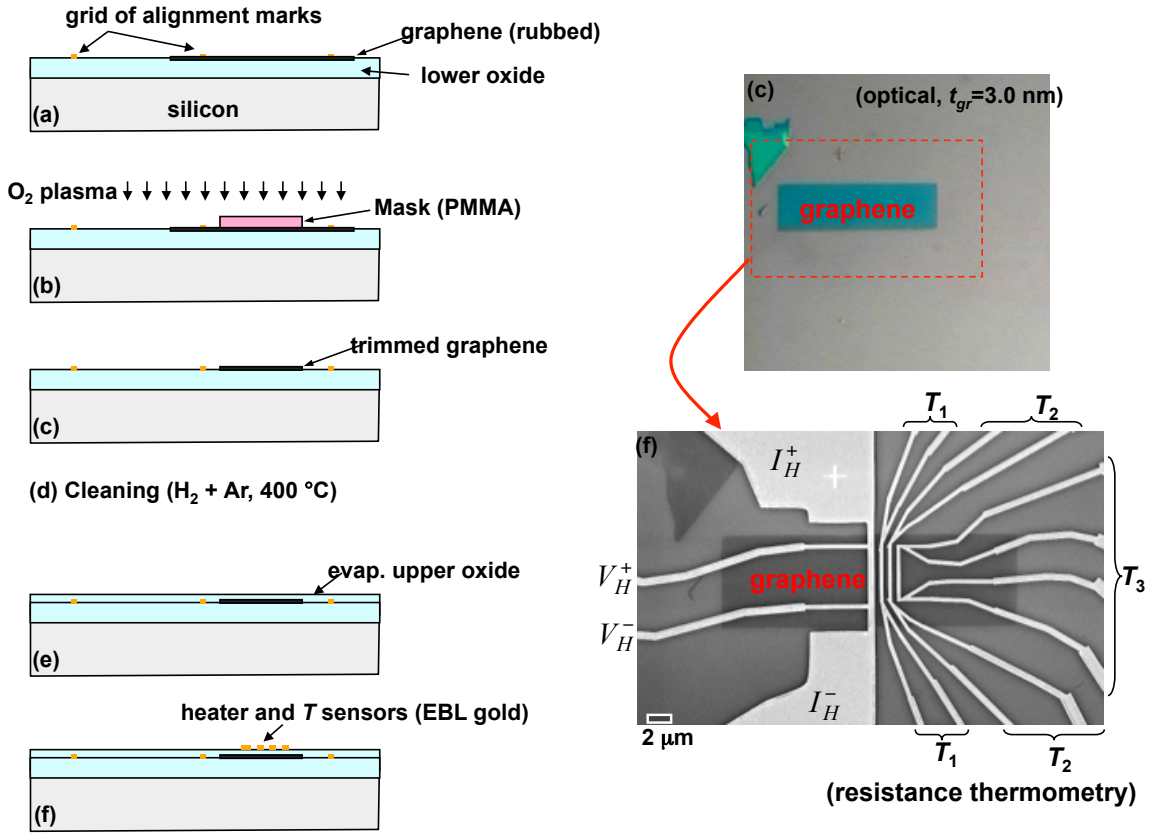

Figure 2-5. Microfabrication of a sample for measurement (by Dr. Wanyoung Jang). (a) Deposit and locate graphene flakes. (b-c) Trim into rectangle using an oxygen plasma. (d) Clean. (e) Evaporate upper oxide. (f) Pattern the heater and temperature sensors.

All the samples are prepared by Dr. Wanyoung Jang. As shown in Fig. 2-5: we start with an oxidized Si wafer with a grid of alignment marks. Then graphene flakes are deposited randomly, and candidate flakes are located with respect to the grid. To facilitate the theoretical analysis and simplify the 3D FEM model, we trim the messy as-deposited graphene flakes into regular rectangular shapes using an oxygen plasma. The next step is a hydrogen cleaning anneal [22], and then the upper oxide layer is deposited by electron beam evaporation. Finally, electron-beam lithography is used to pattern the metallic electrodes by a lift-off process. An important detail is that the current leads of the heater are made as wide as possible outside of the central heating region [Fig. 2-5(f), right], to ensure that the large majority of the joule heat is generated in the immediate vicinity of the graphene sample.

2.2.3 Experiment

A. Set up

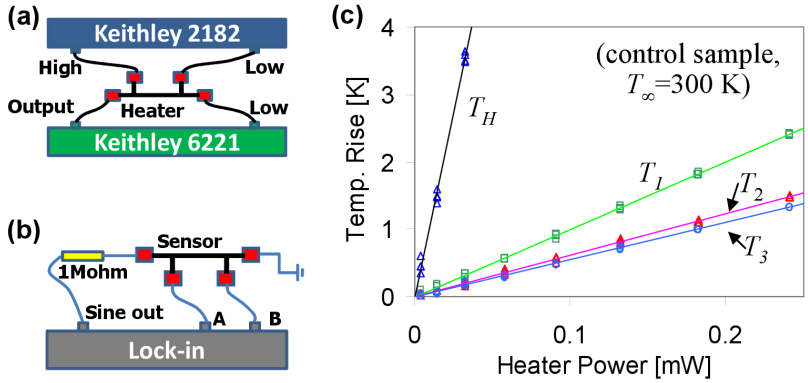

Figure 2-6. (a) Schematic electrical circuit to apply heating power and measure the temperature rise of the heater. (b) Schematic electrical circuit to measure the temperature rise of the 3 sensors. (c) Typical measurements for the "heat-spreader" method: T rise as a function of heater power.

With the sophisticated 3D FEM model and the microfabricated samples, we now set up the experiment to measure the temperature profile in order to fit the thermal conductivity of graphene. The heater and three temperature sensors are independent resistance thermometers measured using four-point probe methods. Figure 2-6(a-b) shows the circuits for the heater and the sensor, respectively, through which the Joule heating (Q_H in Fig. 2-1) is applied and the temperature responses (T_1, T_2, and T_3) are recorded. Figure 2-6(c) shows typical data for the temperature rise at each sensor as a function of DC heater power. The data in Fig. 2-6(c) include both positive and negative heater currents, confirming that we are free of artifacts of Seebeck/Peltier effects or electrical leakage through the upper oxide layer.

The experiments were conducted in a liquid nitrogen cryostat evacuated to a pressure of ~10^{-6} Torr, under which circumstances convection can be neglected, and we also confirmed that radiation is also negligible over our temperature range (from 37 K to 310 K).

B. Fitting scheme

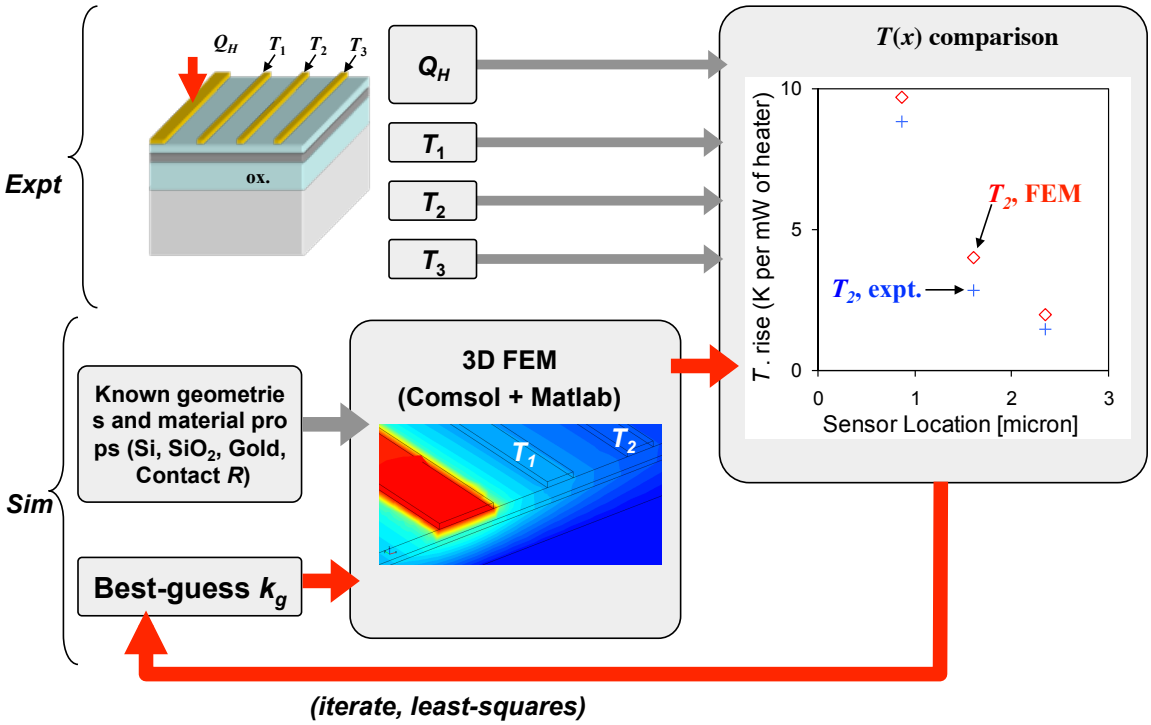

Figure 2-7. Flowchart to extract the thermal conductivity of graphene from a 3D FEM model based on the measured temperature profile (T_1, T_2, and T_3) responding to a Joule heating, and other geometries and thermal properties justified in Table 2-2.

As shown in Fig. 2-7, to extract the thermal conductivity of graphene from the experimentally-measured quantities, we treat the unknown thermal conductivity k of the graphene layer as an adjustable parameter, and solve the 3D FEM model iteratively to find the value of k that results in the best agreement between simulated and measured quantities (sensor temperatures normalized by heater power). Note that all the other input parameters to the 3D FEM model, including geometries and thermal properties, are listed and justified in Table 2-2 of the sensitivity analysis (see Section 2.2.4-F). This non-linear least-squares fitting process is automated by using MATLAB to interface directly with our COMSOL software. Using a single desktop computer, the fitting process typically requires about 0.5 - 1 hour to converge.

C. Improving the experiment

Figure 2-8 shows the result of a control experiment which measures the temperature response on the top surface of the oxide for 9 distances ranging from 1 to 1000 μm away from the heater line. Note that this control experiment has *no* graphene layer, and thus the 3D FEM has *no* fitting parameters. As shown schematically in Fig. 2-9(a), our initial design of the heater line had very long I+ and I- leads, which dissipate more than 20 times of the heating power as compared to the central potion of the heater, leading to temperature response far away from the central heater region. As indicated by curve 1 & 2 in Fig. 2-8, we have to include these long leads in our 3D FEM model in

order for a better comparison with experimental results. However, this will be punished by the computational time.

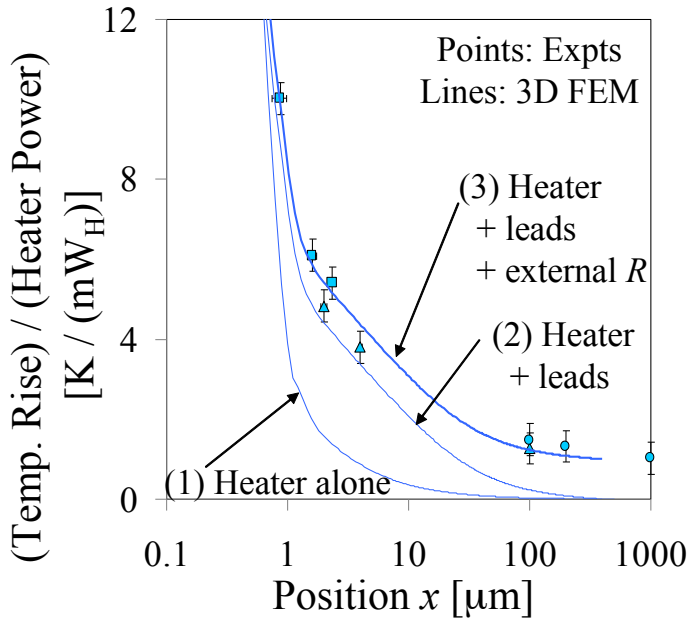

Figure 2-8. Effect made in order to shake hands between measurements and FEM simulations for a control experiment excluding graphene layer from the basic stack. The results suggest two improvements as indicated in Fig. 2-9.

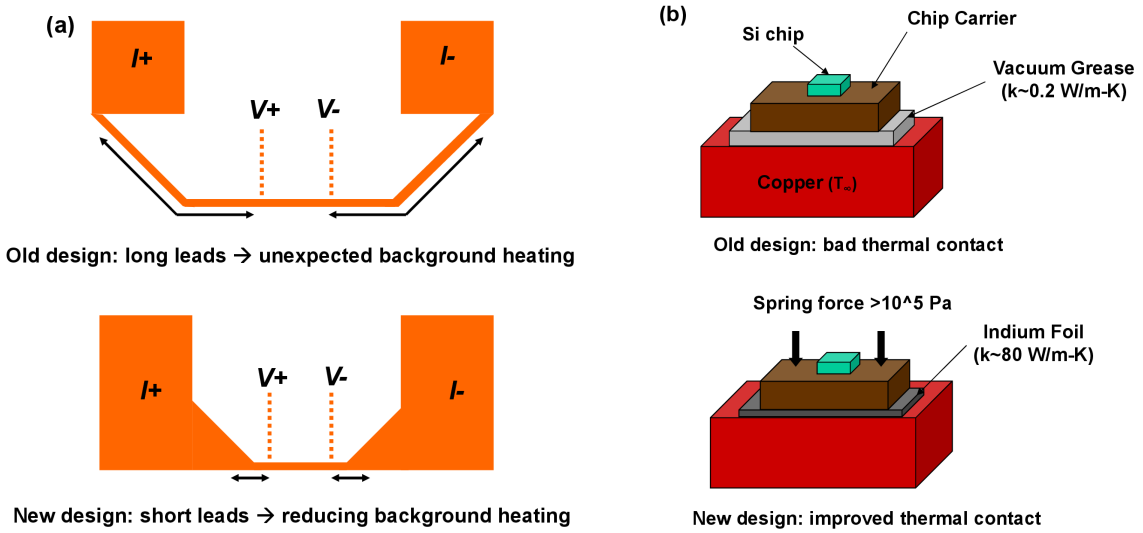

Figure 2-9. Improving the experiment. (a) Shorten heater leads to reduce unnecessary background heating. (b) Reduce thermal resistance to copper heat sink.

In addition, our old design relied on a layer of vacuum grease (k~0.2 W/m-K) for thermal contact between the chip carrier and copper sample stage. We estimate that the thermal resistance of this layer is ~20-40 K/W. Coupled with the large 20x background heating, we estimate that these two effects are enough to cause a significant uniform "background" temperature rise of ~1 K/mW$_{Heater}$, which affects all T sensors uniformly (see curve 3 of Fig. 2-8).

In order to improve our experiment:

• We redesigned the heater current leads to be much shorter and wider [see the schematic in Fig. 2-9(a) and the microfab. in Fig. 2-5(f)], reducing the background heating by a factor of at least 10.

• We replaced the grease with indium foil (k~80 W/m-K) and built a simple spring fixture to apply several atmospheres of clamping pressure [see the schematic in Fig. 2-9(b)] [23-24], which should reduce the background T by another factor of 10.

2.2.4 Results and discussion

A. Validation of method

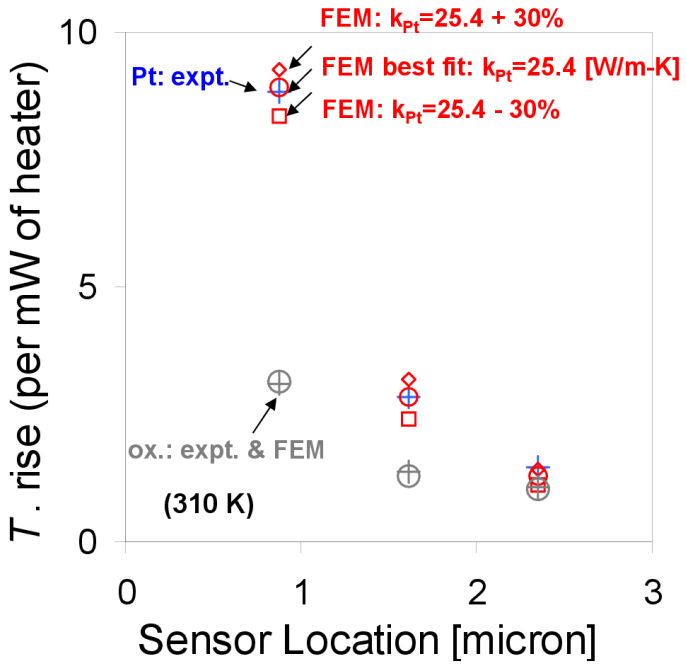

Figure 2-10. Comparison between experimentally-measured sensor temperatures (crosses) and best-fit FEM simulation results (circles) for the simplest "Si + oxide" control experiment (gray), as well as the "Si + Pt + oxide" control experiment (blue, red). We also checked the sensitivity of the Pt fit, which is better than ± 30% (red squares and diamonds).

To validate this new heat spreader method we used the two experiments shown in Fig. 2-10. First, a control experiment was performed without the graphene layer. As shown by the lower curve, this measured baseline T profile is described very well by an FEM fit that treats k of SiO_2 as the only free parameter. (In all other experiments the oxide thermal conductivities are considered to be known and fixed). The fit value for k_{SiO2} at 310 K is 1.43 W/m-K, agreeing to better than 1% with our separate measurement of this SiO_2 using a standard 3ω method [25].

In the second validation experiment (upper curve of Fig. 2-10), we prepared a sample with a 38-nm thick film of evaporated Pt in the stack rather than graphene. The Pt film is an effective heat spreader, leading to significantly higher Ts than the oxide control experiment for the same heating power. Using k of Pt as the only free parameter, the best-fit FEM temperature profile (T_1, T_2, T_3) is in very good agreement with the experimental measurements, and was obtained using a best-fit value of k_{Pt} = 25.4 W/m-K. To confirm this value of k_{Pt} we used the Wiedemann-Franz law to estimate k_{Pt} = 26.6 W/m-K from the resistivity of a four-probe Pt line prepared during the same evaporation run, thus validating this heat spreader + FEM method to within 5%. We also checked the sensitivity of this method by varying the best-fit property away from its optimized value. For example, Fig. 2-10 also show the results of FEM simulations using a value of k_{Pt} that is 30% smaller (red squares) or 30% larger (red diamonds) than the best-fit value. These results show that the sensitivity of this fit is clearly better than ±30%.

B. The effect of thermal contact resistance $R_{c,gr\text{-}ox}$

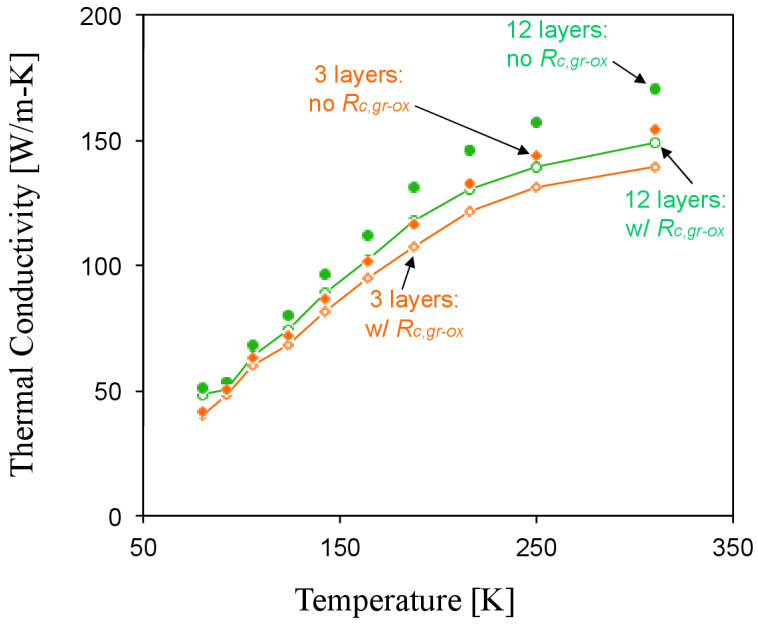

Figure 2-11. Effect of the graphene-oxide thermal contact resistance on the FEM-extracted thermal conductivity of graphene. Accouting for the thermal contact resistance decreases the extracted thermal conductivity of graphene by ~10% at room temperature, and as the temperature goes down, the correction becomes less and less important.

To study the effect of thermal contact resistance between the graphene and the oxide layer, in Section 2.3 we developed a differential 3ω experiment [26] to directly measure the contact resistance between graphene and silicon dioxide over the same temperature range. At room temperature, the measured thermal contact resistance is around 1.0×10^{-8} m^2-K/W, which is equivalent to the thermal resistance of an oxide layer a few tens of nanometers thick [27]. The temperature dependence of the thermal contact resistance is weak around room temperature, transitioning to a power law close to T^{-1} at low temperature. We revised our FEM parameter extraction to account for this thermal contact resistance, thus leading to improved values for the thermal conductivity of graphene. We can see from Fig. 2-11 that accounting for the thermal contact resistance leads to reductions in the extracted graphene thermal conductivity by ~10% at room temperature, and the effect becomes weaker as decreasing temperature. This trend can be qualitatively understood by the simple "fin" model: according to Eqs. (2-1) and (2-2), the thermal contact resistance results in a decrease of the effective "convection" coefficient, which for constant fin parameter *m* also corresponds to a decrease in the graphene thermal conductivity. As the temperature decreases, the conduction thermal resistance of the oxide layer increases more quickly than does the contact thermal resistance, making the contact-resistance term relatively less important to the extracted *k* of graphene at low temperatures.

C. Temperature dependence of k

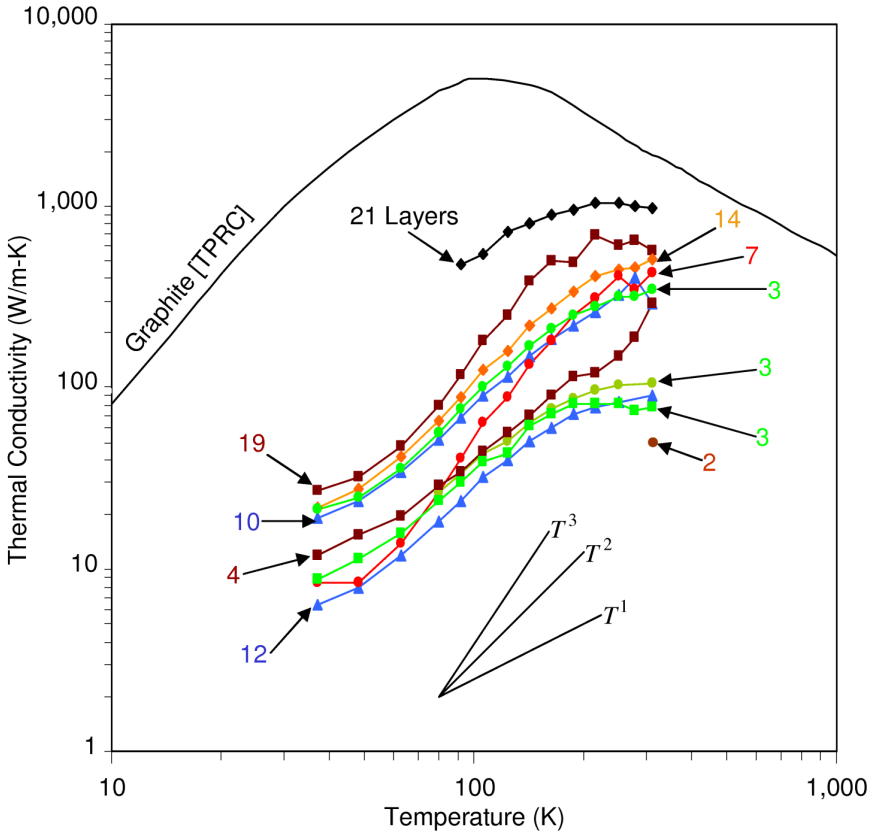

Figure 2-12. Temperature dependence of *k* for encased graphene and ultrathin graphite. TPRC: Ref. [7].

In Fig. 2-12, we plot k as a function of temperature for all of the encased samples measured in this work. For clarity, we omit the error bars here and save them to Fig. 2-13. Figure 2-12 shows that for a given thickness, the suppression of k as compared to bulk graphite is even stronger at lower T. Over the range from 60 K < T < 150 K, seven of the samples follow a power law temperature trend between $T^{1.5}$ and T^{2}. The specific heat of bulk graphite [28] also follows an approximately $T^{1.5}$ power law in this temperature range, suggesting that these samples are in a boundary-scattering regime where k simply tracks the specific heat capacity. At higher T the data in Fig. 2-12 transition to a much weaker power law. We expect that all of these samples have a peak in $k(T)$ near or just above room temperature, indicating the onset of significant Umklapp phonon scattering, although because of the limited T range measured in Fig. 2-12 the peak is only clearly evident for the 19 layer flake. Recent measurements of supported and suspended SLG are also consistent with the existence of a peak in $k(T)$ around room temperature [6, 16].

D. Thickness dependence of k

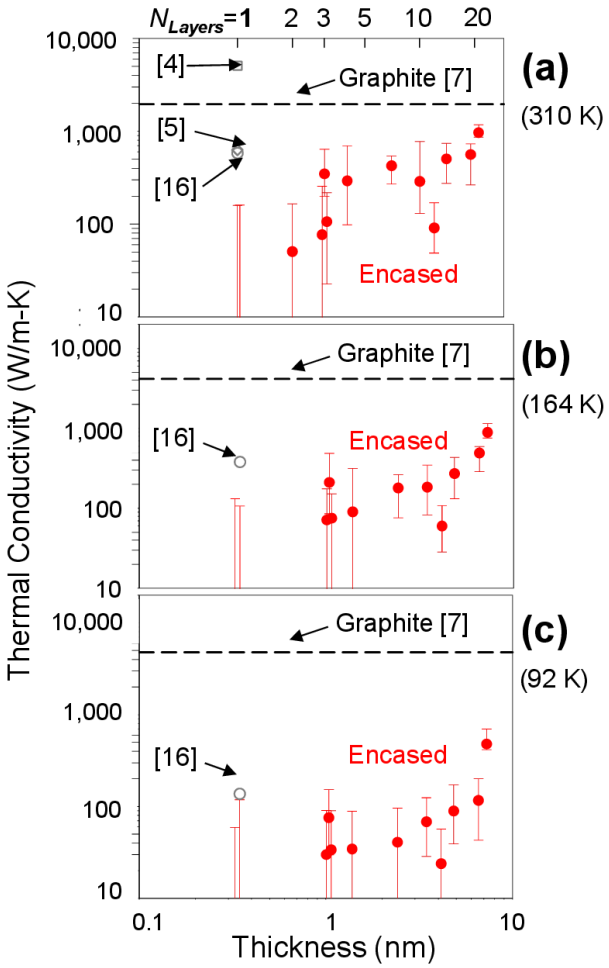

Figure 2-13. k vs. thickness at (a) 310 K, (b) 164 K, and (c) 92 K. Because multiple samples were measured with N_{Layers}=3, their thickness coordinates have been shifted slightly for clarity. The 2 layer flake was only measured at 310 K. Error bars

indicate 95% confidence intervals, and *k* of the encased SLG flake is so low that only the upper bound is significant. For comparison, literature values are also shown for bulk graphite (dashed lines [7]), suspended SLG (open square [4], open diamond [5]), and SiO_2-supported SLG (open circles [16]).

In Fig. 2-13, we plot *k* of encased graphene and ultrathin graphite as a function of thickness at three different temperatures. The 95% confidence intervals (CI) are evaluated using a Monte Carlo method described in Section 2.5 and our estimates of the random and systematic uncertainties (Table 2-2). This analysis reveals that our experiments are most sensitive for thick flakes of high *k*. Conversely, we find that *k* of encased SLG is so low that this heat spreader method can meaningfully give only the upper bound of *k*. For example, as shown in Fig. 2-13(a), at 310 K our measurements show with 97.5% confidence that *k* of encased SLG is below 160 W/m-K. This is well below the room-temperature values of 580 W/m-K reported for SiO_2-supported SLG [16], and ~1000 to ~5000 W/m-K reported for suspended SLG [4-6].

The dominant feature of Fig. 2-13 is the trend that *k* of encased graphene increases with the number of layers, approaching bulk graphite for the thickest sample at room temperature [Fig. 2-13(a)]. We note that this trend is opposite of that reported for suspended graphene [4], which for SLG shows *k* well *above* that of bulk graphite, and with *k decreasing* with the number of layers to approach the bulk graphite value.

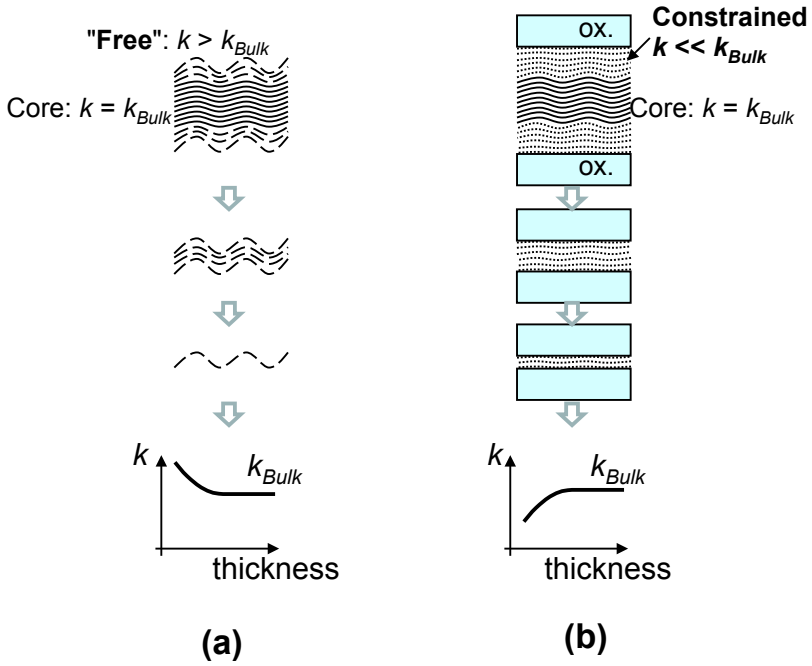

Figure 2-14. (a) Suspended scenario: more DOF and less scattering per layer near the "free" boundaries as compared to the "core", thermal conductivity will increase when decreasing the number of graphene layers. (b) Encased scenario: fewer DOF and more scattering per layer near the "constrained" boundaries as compared to the "core", thermal conductivity will decrease when decreasing the # of graphene layers.

To interpret these opposite trends we offer a simple physical picture: as indicated in Fig. 2-14, for the suspended case, which has a "free" boundary, there are more degrees of freedom (DOF) and less phonon scattering per layer for layers near the boundaries as compared to layers in the "core" [30]. As a result the thermal conductivity of layers near the boundaries is bigger than that of the "core" layers, so, upon decreasing the total number of layers, the boundaries become relatively more important than the core, and the effective average thermal conductivity of a suspended graphene sheet will increase. On the other hand, for the *encased* case, which has "constrained" boundaries, there are fewer DOF and more phonon scattering per layer for layers near boundaries as compared to the "core." Thus, the thermal conductivity of the boundary layers is now smaller than that of the "core" layers, so, upon decreasing the number of "core" layers, the effective thermal conductivity of an *encased* graphene sheet will now decrease.

For the *encased* scenario, a key physical question is to identify the characteristic length δ by which these oxide-induced surface disruptions of the outermost graphene layers extend into the core of the flake due to the weak Van der Waals coupling between adjacent graphene layers.

To address this question we introduce the following phenomenological model. We assume that the in-plane k of an ultrathin graphite flake varies continuously across the flake thickness according to an unknown function $\hat{k}(z,t)$, where $\hat{k}$ is the local thermal conductivity, and z is measured from the midplane of the flake which has a total thickness t. This assumption of a local thermal conductivity function $\hat{k}(z,t)$ is supported in part by the fact that the in-plane thermal conductivity of 3D graphite can be largely understood through analysis of a 2D phonon gas [31]. Because the interlayer Van der Waals coupling is much weaker than the in-plane bonding, the most important effect of the adjacent layers is in scattering the in-plane 2D phonons rather than major alterations of the phonon dispersion [18, 31-32].

Note that our experiments yield only the effective conductivity of the entire flake, equivalent to averaging: $k(t) = \frac{1}{t}\int_{-t/2}^{t/2} \hat{k}(z,t)\,dz$. Referring to Fig. 2-13, at any given temperature we expect $k(t)$ to have three features: (i) For very thick flakes k should recover to the bulk graphite value, that is, $k(t \to \infty) = k_{Bulk}$; (ii) For sufficiently thin flakes it appears that k tends to an approximately constant value k_0, that is, $k(t \to 0) = k_0$; (iii) There is some characteristic thickness at which the $k(t)$ function transitions between the k_0 regime and the k_{Bulk} regime.

Consistent with these criteria, here we suggest a semi-empirical form for the local thermal conductivity function:

$$\hat{k}(z,t) = k_0 + (k_{Bulk} - k_0)\left[1 - \cosh\left(\frac{z}{\delta}\right)\Big/\cosh\left(\frac{t}{2\delta}\right)\right], \qquad (2\text{-}5)$$

where δ characterizes the distance that the oxide-induced disruptions of the outermost surface layers penetrate into the core of the flake. Note that the symmetry of Eq. (2-5) assumes that the upper and lower surfaces of the flake experience similar constraining

effects by their respective adjacent oxides, which is not obvious considering that one interface arises from mechanical exfoliation and the other from evaporation, but nevertheless might be a good approximation if Ref. 16 is correct that the dominant effect of the oxide is in quenching the out-of-plane ZA modes. For flakes much thicker than δ, Eq. (2-5) is simply a function that interpolates between the constrained $\hat{k} = k_0$ at the flake surfaces and $\hat{k} = k_{Bulk}$ deep within the core of the flake, over the exponential decay length δ. Averaging Eq. (2-5) for $-\frac{t}{2} \le z \le \frac{t}{2}$ to compare with experiments gives

$$k(t) = k_0 + \left(k_{Bulk} - k_0\right)\left[1 - \tfrac{2\delta}{t}\tanh\left(\tfrac{t}{2\delta}\right)\right]. \qquad (2\text{-}6)$$

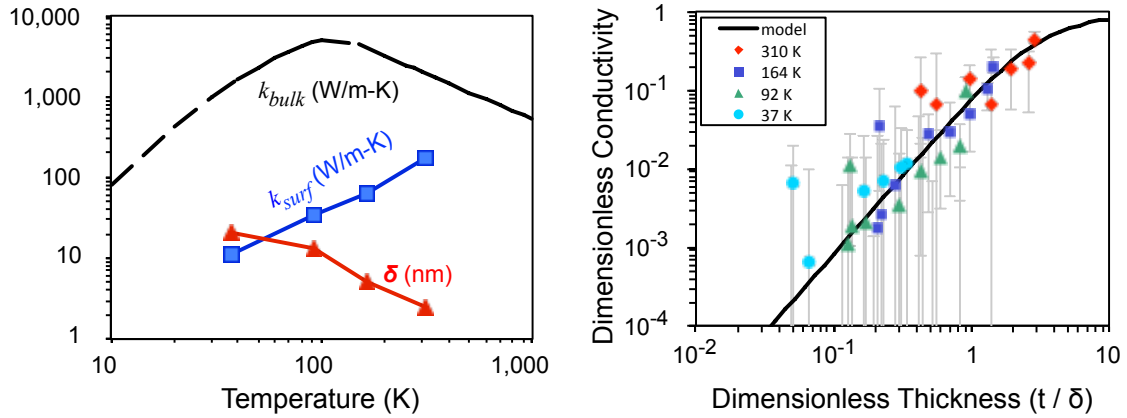

Figure 2-15. (a) Best-fit values of k_0 and δ as functions of temperature. $k_{Bulk}(T)$ is graphite [7]. (b) Dimensionless comparison of Eq. (2-6) with the thickness-dependent measurements from four different Ts, using the dimensionless conductivity $\left(k - k_0\right)/\left(k_{Bulk} - k_0\right)$.

To apply this model to our data, k_0 and δ are treated as T-dependent fitting parameters, while $k_{Bulk}(T)$ is taken from Ref. 7. We use a χ^2 minimization to fit this model to the thickness-dependent k from Fig. 2-13, using k_{Bulk} from TPRC [7]. The temperature dependence of these fitting parameters, k_0 and δ, is given in Fig. 2-15(a), which shows that the oxide-induced surface distortions penetrate much deeper into the core at low temperature. Finally, in Fig. 2-15(b) we collapse the measurements from these four Ts and all thicknesses on to a single dimensionless plot of $\left(k - k_0\right)/\left(k_{Bulk} - k_0\right)$ vs. t/δ, which suggests that Eq. (2-6) is a reasonable description of this entire data set.

E. Estimation of phonon mean free paths

Because the FEM method is based on the continuum diffusion equation which cannot handle ballistic effects, it is only appropriate for flakes with phonon mean free paths smaller than the center-to-center spacing of our T sensors.

To confirm that our samples are in the diffusive rather than ballistic regime, we used kinetic theory to estimate the phonon mean free paths. The two-dimensional form of kinetic theory is $k = \frac{1}{2} C v \Lambda$, where C is the volumetric heat capacity, v is the phonon velocity, the factor of $\frac{1}{2}$ is for a two-dimensional system, and Λ is the phonon mean free path. This simplified "dominant phonon" or "gray" formulation approximates all phonons as traveling at the same velocity, and neglects the contribution of optical modes. Because the temperatures of interest in this study are well below graphite's Debye temperature (~2000 K in-plane), the dominant phonon approach is a much better approximation for graphite/graphene than for most other materials. Therefore we estimate the mean free path as $\Lambda \approx 2k / Cv$, where C is taken from Ref. 28 and v=14,800 m/s is an average of the LA and TA sound velocities using $v^{-2} = \frac{1}{2}\left(v_{s,LA}^{-2} + v_{s,TA}^{-2}\right)$ [33]. Table 2-1 summarizes this calculation using our k measured for representative thick (19 layers) and thin (3 layers, using the average of our three samples of this thickness) samples.

	Heat Capacity, C	Mean Free Path, Λ	
T [K]	[J/m^3-K]	Thick (19 layers)	Thin (3 layers, avg. of 3 samples)
310	15×10^5	51 nm	16 nm
164	6.5×10^5	103 nm	25 nm
92	2.8×10^5	56 nm	23 nm
37	0.55×10^5	67 nm	37 nm
Averages:		69 nm	25 nm

Table 2-1 Estimation of phonon mean free paths in encased graphene.

As shown in Table 2-1, the phonon mean free paths in the graphene samples measured in this work are typically in the range of 20 nm - 100 nm, considerably smaller than the electrode spacings and thus justifying the use of the diffusion equation.

F. Sensitivity analysis using partial derivatives

If the uncertainties of every input parameter are small and assumed to have a Gaussian distribution about their mean value, the classical partial derivative method for uncertainty analysis can be written

$$\frac{u_k}{k} = \sqrt{\sum_i \left(S_i \times \frac{u_{x_i}}{x_i} \right)^2} , \tag{2-7}$$

where u_k is the total uncertainty in graphene's thermal conductivity k, u_{x_i} is the uncertainty in the i-th input parameter x_i, and the dimensionless sensitivities S_i are defined as

$$S_i = \frac{x_i}{k} \frac{\partial k}{\partial x_i} = \frac{\partial \left(\ln k \right)}{\partial \left(\ln x_i \right)} . \tag{2-8}$$

An example of this analysis is summarized in Table 2-2 for the sample that is nominally 12 layers thick. In this sample only the first two sensors were working. The

uncertainties in each of the input quantities are given at the 95% confidence level and are our estimates considering both random and systematic uncertainties at 310 K. The uncertainties were updated as appropriate at other temperatures (not shown). The partial derivatives were evaluated numerically via COMSOL+MATLAB using small perturbations of each parameter around its typical value. To highlight the relative importance of each of the inputs, Table 2-2 also lists each variable's contribution, defined as $c_i = |S_i| \times \left(u_{x_i} / x_i\right)$.

Input parameters		Typical value, x_i	Units	Relative uncertainty, u_i / x_i	Sensit-ivity, S_i	Contribution $c_i = \|S_i\| \times (u_i / x_i)$	Comment on uncertainty estimate
thickness of top and bottom oxide layers	t_{TopOx}	0.025	[μm]	12.0%	-0.10	1.2%	Crystal monitor & stylus profilometer
	t_{BotOx}	0.32		1.6%	-3.84	6.0%	Ellipsometer & SEM
width of heater	w_{Htr}	0.50		2.0%	-0.20	0.4%	Placement accuracy of e-beam lithography patterning; measurements using SEM
center-to-center distances between metal lines	$d_{HtrToS1}$	0.87		0.3%	6.41	2.2%	
	$d_{HtrToS2}$	1.61		0.2%	-0.80	0.2%	
width of *T* sensors	$w_{Sens.}$	0.24		2.1%	-0.44	0.9%	
thermal conductivities of oxide layers, Si substrate, and gold electrodes	k_{TopOx}	0.95	[W/m-K]	5.0%	-0.11	0.6%	Comparison between 3ω measurements, FEM fitting of control samples, & lit. values [S4, S5]
	k_{BotOx}	1.43		5.0%	3.54	17.7%	
	k_{Sub}	93		20%	0.78	15.6%	
	$k_{Electrode}$	141		9.9%	0.06	0.6%	Measured resistivity + Wiedemann-Franz Law
TBR between gr. and ox	$R_{c,Gr\text{-}Ox}$	9.5 x 10^{-9}	[m^2-K/W]	50%	-0.12	6.0%	Measured by 3ω [S6]
Sensor response: *T* rise per unit heating power power	dT_{S1}	8.35	10^3 [K/W]	5.0%	3.06	15.3%	Consequence of measurements and fitting with Bloch-Gruneisen formula [S6-S8]
	dT_{S2}	2.70		5.0%	0.36	1.8%	

Table 2-2 Example of a detailed sensitivity analysis for the nominal 12-layer sample at 310 K.

Table 2-2 reveals the following:

• The thermal conductivity of graphene is very sensitive ($|S_i| > 3$) to the thickness and thermal conductivity of the bottom oxide, the temperature rise of sensor 1, and the distance between electrodes.

• The thermal conductivity of graphene is weakly sensitive ($|S_i| \leq 0.2$) to the top oxide properties, the heater width, the metal thermal conductivity, and the thermal contact resistance between graphene and SiO_2.

• The input parameters with the greatest relative uncertainty (u_i / x_i) are the thermal conductivity of the substrate and the thermal contact resistance between graphene and SiO_2.

The combined effect of the above is that the three most important contributions (largest c_i) to the total uncertainty in graphene's thermal conductivity are the thermal conductivity of the bottom oxide, the thermal conductivity of the silicon substrate, and the temperature rise of sensor 1. We measured the thermal conductivity of the silicon substrate and the bottom oxide using a standard 3-omega method. We determined the uncertainty of these parameters by considering our 3-omega results, literature values [17, 34], and the FEM fitting results for a control experiment without any graphene. The uncertainty in the temperature response of each sensor depends critically on that sensor's temperature coefficient of resistance, which we measure for every sensor and fit using a Bloch- Grüneisen formula [29, 35] (details see Section 2.3.1E).

The thermal contact resistance between graphene and SiO_2 (details see Section 2.3) was also included in our analysis. The thermal contact resistances between Si and SiO_2 and between gold and SiO_2 were not included in the analysis, but by considering the thickness of an equivalent oxide layer [17], the above partial derivative analysis suggests that these corrections should change the final value of graphene's k by at most a few percent, which can be safely neglected compared to the other uncertainties. Likewise, the uncertainty in the electrode thickness (e.g. 55 nm ± 4 nm) was also ignored because it was shown to have a negligible influence on the final extracted value of graphene's k; this is also evident from the fact that the sensitivity to the metal thermal conductivity is very low (Table 2-2).

The layer thicknesses t were determined using a combination of AFM measurements and interference colors under an optical microscope [36-38]. From our previous experience with optical interference colors as cross-referenced with Raman microscopy and electrical transport measurements [36], we are confident in identifying single- and bi-layer graphene flakes and assume negligible uncertainty in this designation. For flakes 3 layers and thicker, the typical standard deviation in AFM thickness measurements is 0.15 nm, and the uncertainty can be considered to be at most ±1 layer. For simplicity in plotting and designating samples we rounded the AFM measured thickness to the nearest integer number of layers. We have confirmed numerically that our heat-spreading method is only sensitive to the product $k \cdot t$, because all graphene flakes are so thin that there are negligible temperature gradients through the flake's thickness. Thus any uncertainty in t leads translates directly to an equal uncertainty in k. Therefore, for a 3 layer flake, an uncertainty of ±1 layer would contribute an additional 33% uncertainty in k, and for a 10±1 layer flake the additional uncertainty in k is only 10%. These uncertainties are not incorporated in the error bars of Fig. 2-12 where they would be only a minor correction.

2.3 Thermal contact resistance

To ensure effective heat transfer away from active devices and into heat sink regions, future graphene-based microelectronics, interconnects, and thermal management structures will require good thermal contact between graphene and other materials, especially dielectrics.

While direct measurements are rare [1, 51] for the thermal contact resistance involving graphene, the thermal contact resistance of several related carbon materials has been measured by various groups. For example, using a transient thermoreflectance technique, Schmidt *et al*. [39] measured the thermal contact resistance between a highly ordered pyrolytic graphite (HOPG) substrate and an Al thin film to be 2.0×10^{-8} m^2-K/W at 300 K. Yu *et al.* [40] measured the thermal contact resistance between a 152-nm-diameter carbon nanofiber and a Pt substrate; based on the reported contact width (10 nm), and our estimates of the contact length from the published scanning electron microscope (SEM) images, the equivalent thermal contact resistance of the nanofiber is $4.4 - 6.7\times10^{-8}$ m^2-K/W at room temperature. For single-walled carbon nanotubes on SiO_2 substrates, by fitting the measured electrical breakdown voltages to a thermal model, Pop *et al*. [41] extracted a contact resistance equivalent to $1.0 - 2.1\times10^{-8}$ m^2-K/W from 500 ^{0}C - 700 ^{0}C.

Here we report measurements of the thermal contact resistance between single- and few-layer graphene and silicon dioxide, using a differential 3ω method [26] over a temperature range from 42 K to 310 K.

2.3.1 Experimental method

A. A differential 3ω method

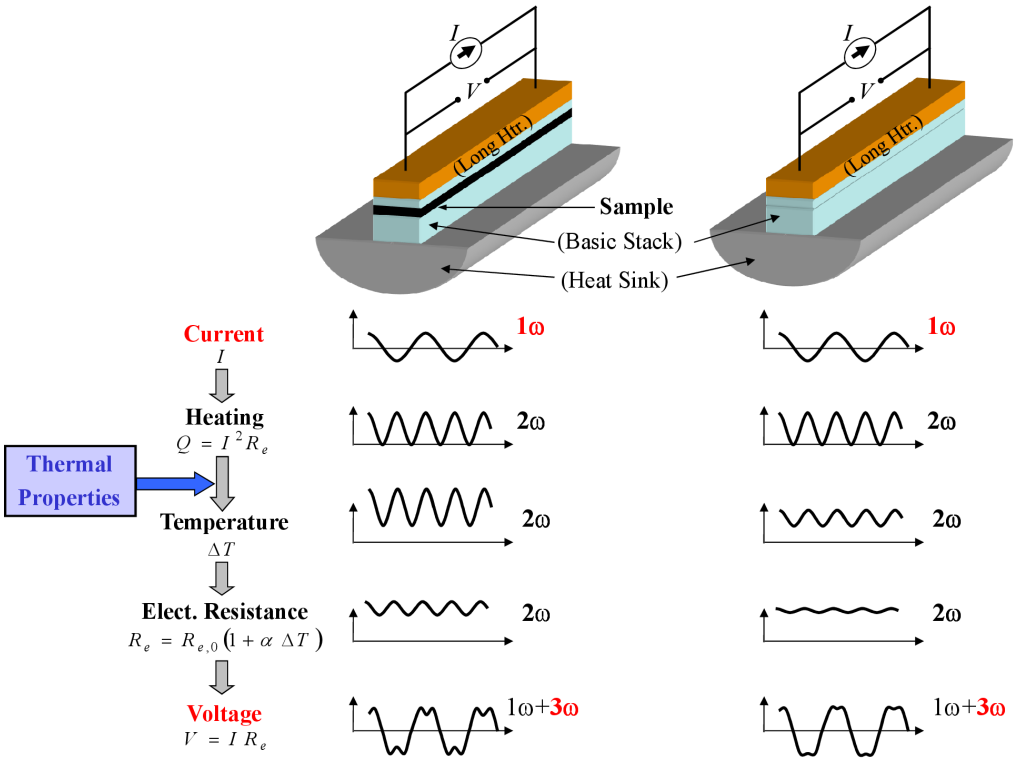

Figure 2-16. Schematic of the differential 3ω method. Two samples have the same structure except one has the thin film of interest while the other not. The thermal

property of interest (*k* of the thin film or R_c) can be extracted by subtracting the thermal impendences of the two samples measured by a classical 3ω method, respectively.

We first briefly introduce the classical 3ω method, a standard technique to measure thermal properties of both bulk and micro/nano structrues [25, 42]. As shown in Fig. 2-16, the measurement is driven by an AC current with angular frequency ω through a heater line microfabricated on the surface of the sample. The resulting Joule heating oscillates at a frequency of 2ω, which correspondingly produce a temperature field oscillating at the same frequency. As a response to this temperature oscillation, an AC component with a frequency of 2ω is superposed to the original DC component of the electrical resistance of the heater line. Finally, combining these two components of the electrical resistance with the driving AC current, we obtain two superposed voltage components, $V_{1\omega}$ and $V_{3\omega}$, both of which contain important information of thermal properties of the sample. In particular, the 3ω component is widely used, and known as the 3ω method.

We now describe the differential 3ω method, which extends the classical 3ω method for thin film measurement, especially for samples containing multiple thin films. As indicated in Fig. 2-16, two samples are prepared, which have exactly the same structure except that the primary sample includes the thin film of interest while the control sample does not. Subtracting the thermal impedance of the control sample (Z_B) from that of the primary sample (Z_A) gives net thermal impedance of the thin film and the thermal contact resistances.

Note that the thermal impedance of the atomic graphene layer is negligible for our sandwich structure (Fig. 2-1), so the thermal contact resistance dominates, i.e., $Z_A - Z_B = \left(R_{g\leftrightarrow top\ ox} + R_{g\leftrightarrow bot.\ ox}\right) - R_{top\ ox\leftrightarrow bot.\ ox}$. We assume the thermal contact resistances from graphene to top and bottom oxides are identical ($R_{g\leftrightarrow top\ ox} = R_{g\leftrightarrow bot.\ ox} = R_{g\leftrightarrow ox}$), and neglect the contact resistance between the top and bottom oxide layers in the control pattern ($R_{top\,ox\leftrightarrow bot.ox} << 2R_{g\leftrightarrow ox.}$). Thus, we calculate $R_{g\leftrightarrow ox} = \frac{1}{2}(Z_A - Z_B)$.

B. Microfabrication

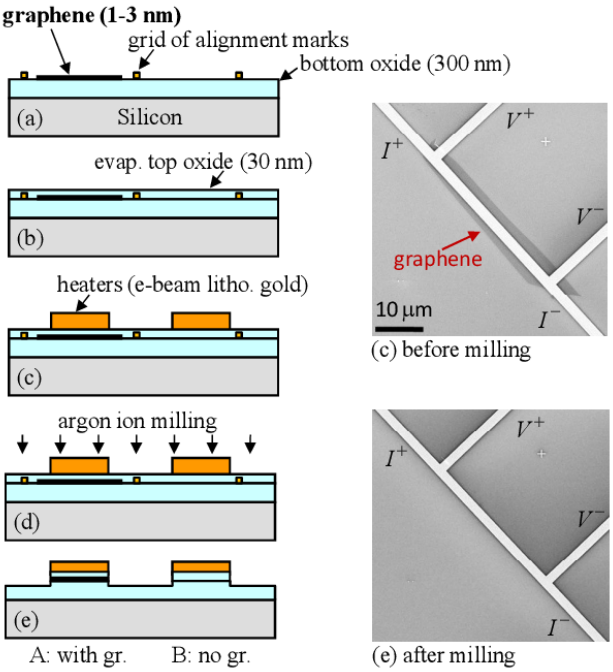

Figure 2-17. Sample microfabrication (by Dr. Wanyoung Jang). (a) Deposit and locate graphene flakes. (b) Cleaning anneal, then evaporate top oxide. (c) Pattern the heaters. (d-e) Ion mill the top surface using an Ar beam, to trim the flake and simplify the thermal analysis.

The samples are prepared by Dr. Wanyoung Jang. As shown in Fig. 2-17: first, graphene flakes are deposited randomly on an oxidized Si wafer using an exfoliation method [36, 43]. Although it would be desirable for the bottom oxide to be thinner in order to minimize the background thermal resistance, we are restricted to use a 300 nm thick layer because of the optical interference method used to identify the thin flakes [43]. Candidate flakes are then located with respect to a grid of alignment marks. Next we anneal the samples with Ar (1.7 L/min) and H_2 (1.9 L/min) at 400 °C for 1 hour [22], followed by electron-beam evaporation of approximately 30 nm of silicon dioxide. Then electron-beam lithography is used to pattern evaporated Cr/Au electrodes (thickness 5 nm / 175-345 nm) by a lift-off process. Finally, we use an argon ion beam (inductively coupled plasma at 450 W, with 50 W of RF power) to mill the top surface of the sample to an etch depth slightly greater than the original thickness of the top oxide. In this way the graphene flake is trimmed to match the width of the metal heater line, which ensures one dimensional (1D) heat flow through the graphene flake, as justified in the following section. To facilitate the differential 3ω measurements, on every sample we fabricate two heaters in close proximity with identical heater patterns and etch depths: the primary pattern ("A") which includes the graphene flake between the oxide layers, and a control pattern ("B") with top and bottom oxide layers but no graphene [Fig. 2-17(e)].

C. Justification of the 1D heat transfer assumption

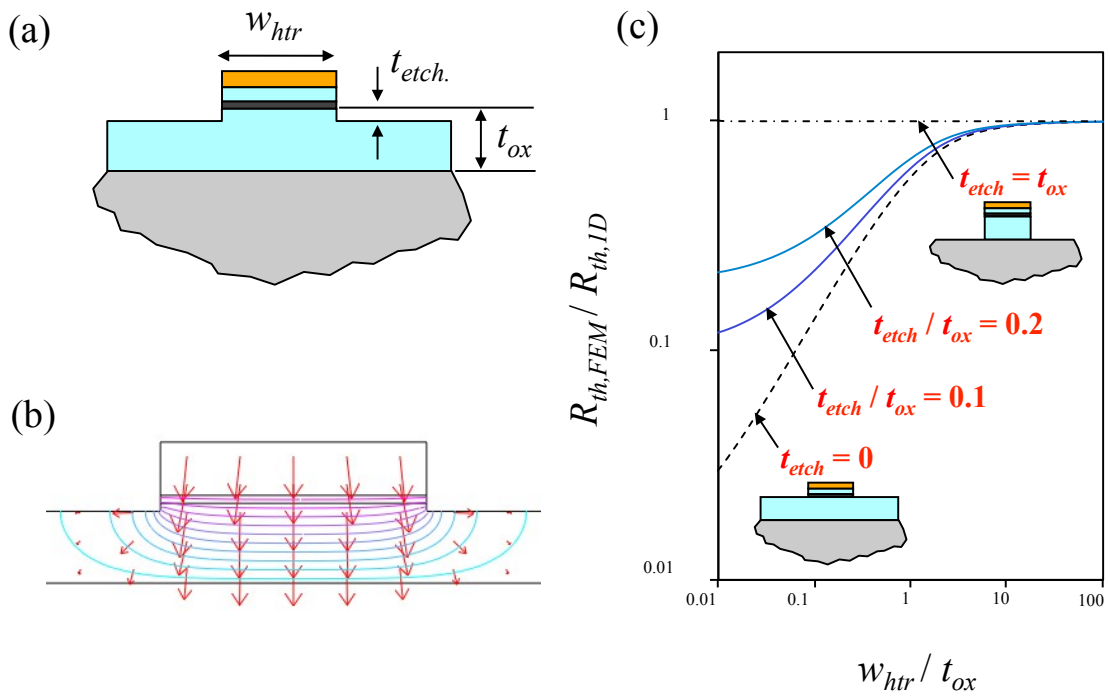

Figure 2-18. One dimensional heat transfer justification. (a) Three key length scales of the problem. (b) Visualization of the isotherms and flux lines by a 2D FEM simulation. (c) Convergence of the real thermal resistance to the ideal 1D resistance, $R_{th,FEM}$/ $R_{th,1D}$, as a function of the dimensionless group w_{htr}/t_{ox}. Typical expected values of these parameters in the real experiments: w_{htr} = 3 μm, t_{etch} = 60 nm, t_{ox} = 300 nm.

We now justify the assumption of the 1D heat transfer through the sandwich structure (top SiO_2 + graphene + bottom SiO_2). As indicated in Fig. 2-18(a), there are three important lengths in this problem: the heater width (w_{htr}), the oxide thickness (t_{ox}), and the etching depth (t_{etch}). Ideally, we want $w_{htr} >> t_{ox}$ or $t_{etch} = t_{ox}$ to ensure 1D heat transfer through the sandwich structure. In practice, however, we are constrained by the graphene flake size and concerned about the time and cost of the ion milling. In order to compromise between the ideality and reality, we performed analysis utilizing a two dimensional finite element method (2D FEM) through a commercial software package (COMSOL). To mimic the real experiment, we use a flux boundary condition to represent the heater. We then apply a temperature boundary condition on the lower surface of the bottom oxide, and set the other boundaries to be adiabatic. Figure 2-18(b) shows the isotherms and adiabats for a representative structure, which confirms the 1D heat transfer qualitatively. Note that we exaggerated the thickness of graphene for clarity. For a quantitative justification, in Fig. 2-18(c) we normalize the real thermal resistance ($R_{th,FEM}$) by the ideal 1D resistance, $R_{th,1D} = t_{ox}/(k_{ox} \cdot w_{htr})$, and plot it as a function of a dimensionless group w_{htr}/t_{ox}. We showed four different scenarios by increasing the etching depth from zero to all the way through the bottom oxide. The first feature is, as expected, that $R_{th,FEM}$ gradually converges to $R_{th,1D}$ as w_{htr}/t_{ox} increases for all the scenarios. The second feature is that as the etching depth increases, the convergence becomes faster. Based on this analysis, and also considering the reality, we design our

experiment parameters to be: w_{htr} = 3 μm, t_{etch} = 0.2·t_{ox}, which introduces a 4.5% error by assuming 1D heat transfer through the sandwich structure. Note that this is a conservative analysis since it ensures the heat transfer through not only graphene but also the oxide to be one dimensional.

D. A current-sweep scheme

The experiments are conducted at temperatures from 42 K - 310 K in a liquid helium cryostat evacuated to ~10^{-6} Torr. Although differential 3ω methods most commonly use a single value of the electrical current and evaluate the difference between two frequency sweeps [26], we have found somewhat improved uncertainty by fixing the frequency (at 1000 Hz) and evaluating the difference between two current sweeps. In this scheme we check the linearity of the curve of heater temperature rise vs. power, to verify that the current and voltage are free of offset errors and non-thermal harmonics. We confirmed that the final results are independent of the frequency chosen for the current sweep. For example, contact resistance measurements taken at 10, 500, 1000, and 10000 Hz agree to within ±3.8% at 310 K and ±2.2% at 80 K [95% confidence interval (CI)].

E. A Bloch- Grüneisen formula

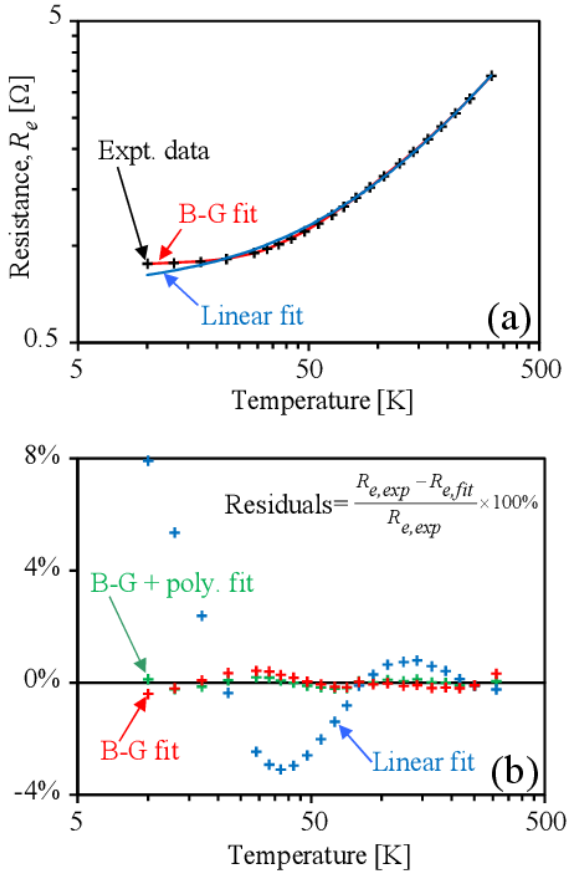

Figure 2-19. Fitting the electrical resistance of a typical heater. (a) Comparison between the experimental data (points) and the fits using a linear (blue line) or

Bloch-Grüneisen (B-G) formula (red line). On these logarithmic axes the linear fit appears curved. (b) Residuals for the linear fit (blue), B-G fit (red), and B-G + empirical polynomial fit [green; see Eq. (2-10)].

The largest contribution to the overall uncertainty in $R_{g\text{-}ox}$ is the uncertainty in the temperature response of the electrical resistance of the heater, dR_e/dT. As shown in Fig. 2-19(a), a simple linear fit $R_e = a + bT$ is clearly inadequate to describe the calibration curve $R_e(T)$ over the large temperature ranges of interest. Therefore, for every heater pattern we fit the measured $R_e(T)$ with a Bloch-Grüneisen formula [35]

$$R_{e,BG}(T) = r_0 + 4\Delta\left(\frac{T}{\theta}\right)^5 \int_0^{\frac{\theta}{T}} \frac{z^5 e^z}{(e^z - 1)^2} dz \,, \tag{2-9}$$

where r_0 is the residual resistance indicating the impurity and boundary scatterings of electrons, θ is the Debye temperature, and Δ is a scaling factor indicating the strength of electron-phonon coupling. As shown in Fig. 2-19, $R_{e,BG}(T)$ is a much better description of the experimental $R_e(T)$. As expected the residuals of this improved fit reveal small but clear deviations from the simple Bloch-Grüneisen theory [Fig. 2-19(b)] [35]. We capture these deviations empirically using a low-order polynomial in ln(T):

$$R_e(T) \approx R_{e,BG}(T) + \sum_{n=1}^{N} c_n \left[\ln(T)\right]^n \,, \tag{2-10}$$

where the results become approximately independent of N for $3 \le N \le 5$. Finally, we differentiate Eq. (2-10) analytically to obtain the required dR_e/dT. [Our final results are taken as the average of the values obtained from the 3rd, 4th, and 5th order versions of Eq. (2-10).]

2.3.2 Results and discussion

A. Thickness and temperature dependence of $R_{g\text{-}ox}$

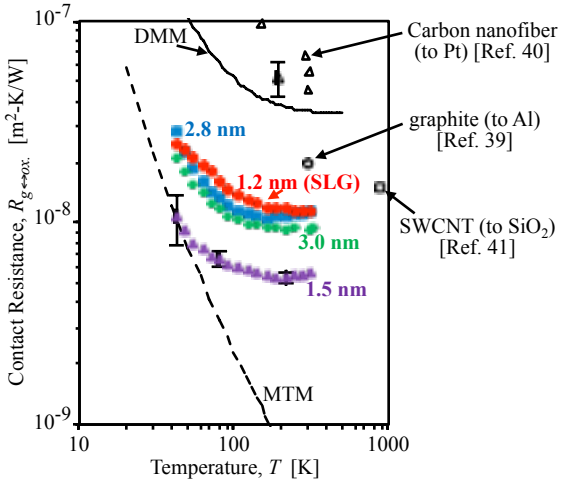

Figure 2-20. Experimental measurements of the thermal contact resistance between silicon dioxide and graphene, for four samples of different thicknesses (filled points, in color). Also included for comparison are the contact resistances of several related carbon materials from the literature (open points), and theoretical curves for a diffuse mismatch model (DMM) and a maximum transmission model (MTM) (lines).

The measured thermal contact resistances between graphene and SiO_2 are shown in Fig. 2-20 for four samples with different thicknesses (1.2 nm, 1.5 nm, 2.8 nm, and 3.0 nm) as determined by atomic force microscopy (AFM). Based on these AFM measurements [37-38] and our experience with the interference colors under an optical microscope [36], we believe that the 1.2 nm and 1.5 nm samples are single layer (SLG) and bilayer graphene (BLG), respectively. As shown in Fig. 3, the typical uncertainty in the contact resistance ranges from approximately ±7% at 310 K to ±28% at 42 K (95% CI). At room temperature the contact resistance is found to range from 5.6×10^{-9} to 1.2×10^{-8} m^2-K/W, which is relatively low compared to typical values reported for various other material pairings [44], and in particular is lower than previous measurements of the contact resistance of carbon materials to various substrates [39-41].

Although the measurements in Fig. 2-20 do not exhibit any clear dependence on the sample thickness, all four samples follow roughly the same temperature trend. Around room temperature, the contact resistance is relatively independent of temperature, although two of the samples show a slight minimum in $R_{g\text{-}ox}(T)$ around 200 K. Below about 100 K, all four samples show a marked increase in contact resistance, transitioning to a power law that can be approximated as $R_{g\leftrightarrow ox} \propto T^{-1}$.

B. Comparing to theoretical models

Modeling the thermal contact between graphene and silicon dioxide is challenging due to the amorphous nature of the SiO_2 and the highly anisotropic properties of the graphene. Here we briefly consider two simple models as shown in Fig. 2-20 (a more sophisticated model will be developed in Chapter 3). First, a lower bound on the thermal contact resistance is the "maximum transmission model" (MTM) [33], a generalization of the "phonon radiation limit" [45]. The phonon internal energies were determined from

experimental values of the heat capacity [28]. The characteristic velocities were taken as 4487 m/s and 2157 m/s for oxide (isotropic) and graphene (c-axis [28]), respectively, determined from a weighted average of the transverse and acoustic sound speeds. The second model considered in Fig. 2-19 is the elastic diffuse mismatch model (DMM) described by Duda *et al*. for thermal contact between isotropic and anisotropic materials [46, 47]. As shown by the dashed (MTM) and solid (DMM) lines in Fig. 2-20, both models capture certain features in the measurements, but with significant weaknesses. The MTM indeed serves as a lower bound and appears promising below about 60 K, but it greatly underpredicts the true contact resistance at higher temperatures. The DMM qualitatively captures most of the temperature trend, but the DMM values are too large by a factor of approximately 6 at all temperatures, which may indicate that inelastic phonon scattering (neglected in this implementation [46]) is a significant channel for heat flow.

2.4 Summary

This portion of the thesis focused on measuring thermal properties of encased graphene. First, we have developed and validated a heat spreader method to measure k of graphene and ultrathin graphite encased within SiO_2. These results highlight the importance of layer thickness and interfacial coupling for in-plane heat transfer. In particular, to maximize k by ultrathin graphite encased in SiO_2 at room temperature, layer thicknesses of at least 10 nm should be targeted to ensure $k > 1000$ W/m-K. Second, we have measured the thermal contact resistance between graphene and silicon dioxide from 42 K to 310 K, and found resistance values significantly lower than previous measurements involving related carbon systems [39-41]. These measurements should prove helpful for interpreting recent experiments involving heat transfer and energy dissipation in graphene [4, 48-49], and are an encouraging development for possible future applications of graphene in microelectronics, interconnects, and thermal management structures.

2.5 Appendix: a Monte Carlo scheme for uncertainty analysis

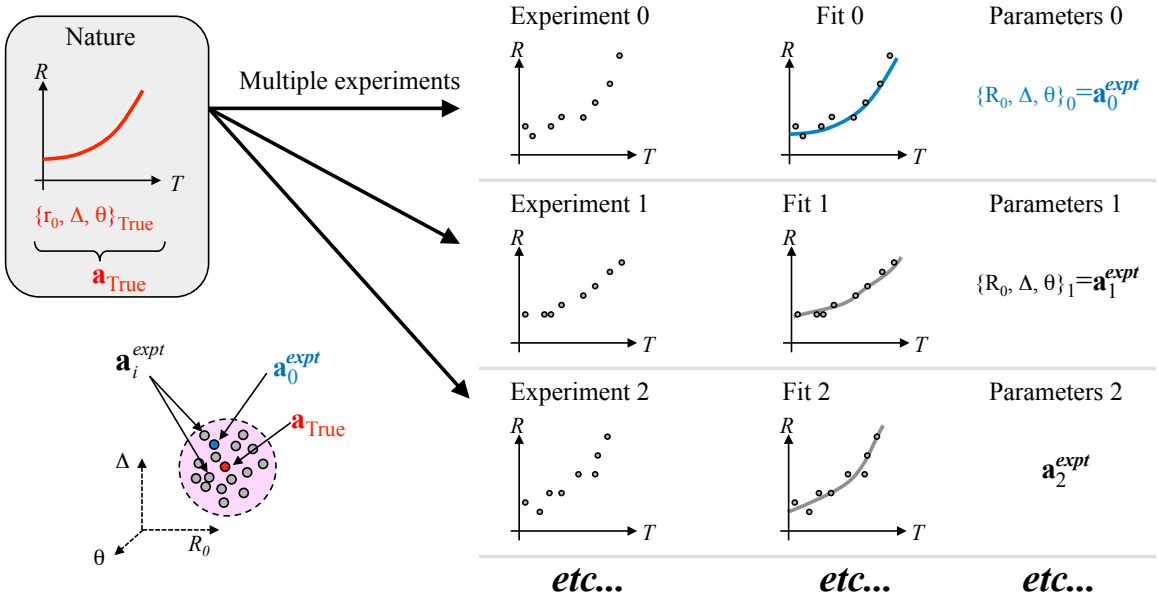

Figure 2-21. A straightforward approach to estimate confident intervals in the temperature-resistance calibration.

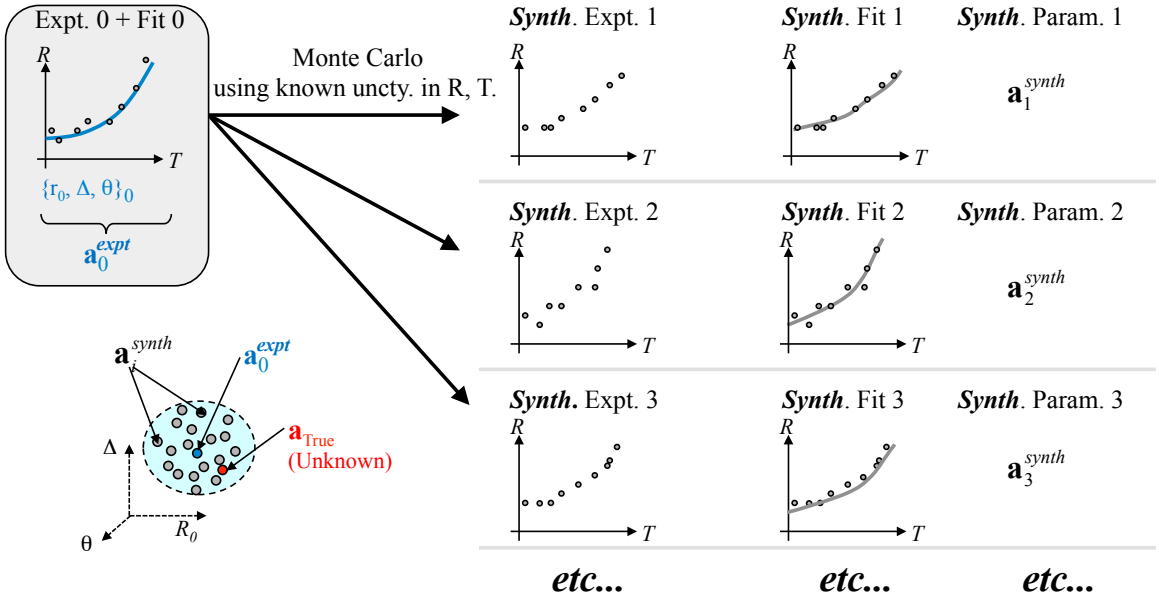

Figure 2-22. A Monte Carlo approach to estimate confident intervals in the temperature-resistance calibration.

"Offered the choice between mastery of a 5-foot shelf of analytical statistics books and middling ability at performing statistical Monte Carlo simulations, we would surely choose ... the latter." - W. H. Press *et al.*, Numerical Recipes 3rd edn.

We choose a Monte Carlo scheme [29] to analyze uncertainties for both the thermal conductivity of graphene (k_{gr}) and the calibration of temperature-resistance relation [$R(T)$] of microfabricated thermometers. In the k_{gr} analysis, as shown in Table 2-2 certain input parameters such as the substrate thermal conductivity and the contact resistance between graphene and SiO_2 have rather large uncertainties, violating one of the basic assumptions of the partial derivative uncertainty analysis described in Section 2.2.4.F. In the $R(T)$ calibration, the dataset are nonlinear and complicated. In both scenarios, Monte Carlo simulations are good options to analyze uncertainty propagations.

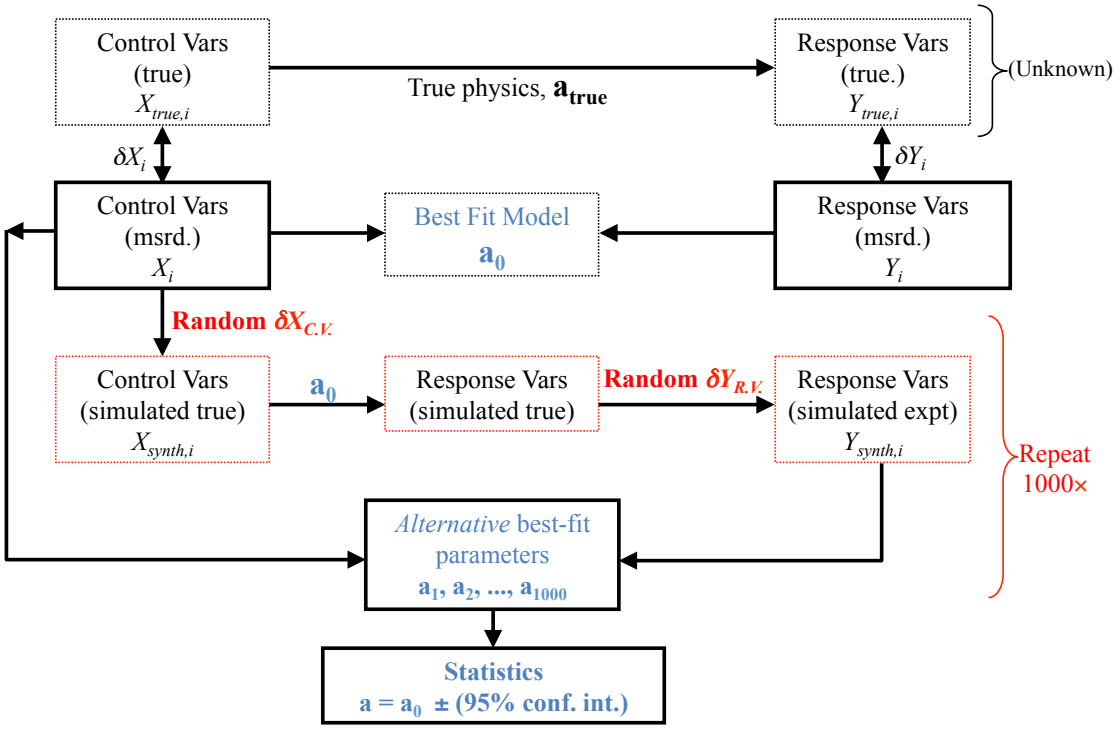

Figure 2-23. Flowchart of a Monte Carlo scheme to analyze uncertainty.

We use the $R(T)$ calibration as an example to demonstrate this Monte Carlo scheme. As illustrated in Fig. 2-21, here T is the control variable (X_i) set in the cryostat, R_e is the response variable (Y_i) measured using a four-probe method [Fig. 2-6(a)]. Our goal is find the true physics, *i.e.*, the three parameters, r_0, θ, and Δ, of the Bloch-Grüneisen formula [Eq. (2-9)]. For simplicity, we group these three parameters to define a vector parameter, $\mathbf{a} = \{r_0, \theta, \Delta\}$. A straightforward approach is to calibrate multiple trials to estimate $\mathbf{a}_{true} \approx avg.(\mathbf{a}_i^{expt.})$ and the confident interval from the scatter of $\mathbf{a}_i^{expt.}$. However, in most cases we only have one measurement, thus only $\mathbf{a}_0^{expt.}$. As shown in Fig. 2-22 and the flowchart of Fig. 2-23, the Monte Carlo scheme allows us to generate numerous synthetic control-response variable datasets ($T_{synth,i}$, $R_{synth,i}$) from the measured (T_0, R_0) dataset based on the Bloch-Grüneisen formula and the known statistical distributions of experimental uncertainties in T_i and R_i. Fitting each synthetic dataset with the model yields a slightly different outcome for the fitting parameter $\mathbf{a}_i^{synth.}$, the statistics of which finally allow us to calculate the uncertainty in $\mathbf{a}$. Note that this scheme

implicitly assumes the error propagation (the "error cloud" in Fig. 2-21 and 2-22) in the neighborhood of $\mathbf{a}_0^{expt.}$ is similar to in the neighborhood of $\mathbf{a}_{\mathbf{true}}$.

Likewise, in the k_{gr} analysis, the control variables (X_i) are all the geometries and the thermal properties input to the FEM model (Fig. 2-7), except k_{gr}; the response variables (Y_i) are the temperatures measured by the three resistive thermometers; the best fit model is the 3D FEM model; and the fitting parameter ($\boldsymbol{a}$) is k_{gr} at a specific cryostat temperature.

In both scenarios, we confirmed that the MC results are converged by comparing results from multiple MC trials. In the k_{gr} analysis, to validate our implementation of the MC method we evaluated a test case using small uncertainties for all input parameters, and confirmed that it was in close agreement with the partial derivative method.

2.6 References

[1] Z. Chen, W. Jang, W. Bao, C. N. Lau, C. Dames, Thermal contact resistance between graphene and silicon dioxide, *Appl. Phys. Lett.* **95**, 161910–161913 (2009).

[2] W. Jang, Z. Chen, W. Bao, C. N. Lau, C. Dames, Thickness-Dependent Thermal Conductivity of Encased Graphene and Ultrathin Graphite, *Nano Lett.* **10**, 3909–3913 (2010).

[3] A. K. Geim, Graphene: status and prospects., *Science* **324**, 1530–4 (2009).

[4] A. A. Balandin *et al.*, Superior thermal conductivity of single-layer graphene., *Nano Lett.* **8**, 902–7 (2008).

[5] C. Faugeras *et al.*, Thermal conductivity of graphene in corbino membrane geometry., *ACS Nano* **4**, 1889–92 (2010).

[6] W. Cai *et al.*, Thermal transport in suspended and supported monolayer graphene grown by chemical vapor deposition., *Nano Lett.* **10**, 1645–51 (2010).

[7] Y. S. Touloukian, *Thermophysical Properties of Matter* (IFI/Plenum, New York).

[8] N. Mingo, D. A. Broido, Length Dependence of Carbon Nanotube Thermal Conductivity and the "Problem of Long Waves," *Nano Lett.* **5**, 1221–1225 (2005).

[9] P. Kim, L. Shi, A. Majumdar, P. McEuen, Thermal Transport Measurements of Individual Multiwalled Nanotubes, *Phys. Rev. Lett.* **87**, 215502 (2001).

[10] T. Y. Choi, D. Poulikakos, J. Tharian, U. Sennhauser, Measurement of thermal conductivity of individual multiwalled carbon nanotubes by the 3-ω method, *Appl. Phys. Lett.* **87**, 013108 (2005).

[11] H.-Y. Chiu *et al.*, Ballistic Phonon Thermal Transport in Multiwalled Carbon Nanotubes, *Phys. Rev. Lett.* **95**, 226101 (2005).

[12] E. Pop, D. Mann, Q. Wang, K. Goodson, H. Dai, Thermal conductance of an individual single-wall carbon nanotube above room temperature., *Nano Lett.* **6**, 96–100 (2006).

[13] M. T. Pettes, L. Shi, Thermal and Structural Characterizations of Individual Single-, Double-, and Multi-Walled Carbon Nanotubes, *Adv. Funct. Mater.* **19**, 3918–3925 (2009).

[14] A. Majumdar, Microscale Heat Conduction in Dielectric Thin Films, *J. Heat Transfer* **115**, 7 (1993).

[15] M. Asheghi, Y. K. Leung, S. S. Wong, K. E. Goodson, Phonon-boundary scattering in thin silicon layers, *Appl. Phys. Lett.* **71**, 1798 (1997).

[16] J. H. Seol *et al.*, Two-dimensional phonon transport in supported graphene., *Science* **328**, 213–6 (2010).

[17] S.-M. Lee, D. G. Cahill, Heat transport in thin dielectric films, *J. Appl. Phys.* **81**, 2590 (1997).

[18] S. Berber, Y.-K. Kwon, D. Tománek, Unusually High Thermal Conductivity of Carbon Nanotubes, *Phys. Rev. Lett.* **84**, 4613–4616 (2000).

[19] N. Mingo, D. Broido, Carbon Nanotube Ballistic Thermal Conductance and Its Limits, *Phys. Rev. Lett.* **95**, 096105 (2005).

[20] K. Saito, J. Nakamura, A. Natori, Ballistic thermal conductance of a graphene sheet, *Phys. Rev. B* **76**, 115409 (2007).

[21] F. P. Incropera, D. P. DeWitt, T. L. Bergman, A. S. Lavine, *Fundamentals of Heat and Mass Transfer* (ed. 6th).

[22] M. Ishigami, J. H. Chen, W. G. Cullen, M. S. Fuhrer, E. D. Williams, Atomic structure of graphene on SiO2., *Nano Lett.* **7**, 1643–8 (2007).

[23] F. Pobell, *Matter and methods at low temperatures* (Springer, 2007).

[24] R. C. Richardson, E. N. Smith, *Experimental techniques in condensed matter physics at low temperatures* (Westview Press, 1998).

[25] D. G. Cahill, Thermal conductivity measurement from 30 to 750 K: the 3ω method, *Rev. Sci. Instrum.* **61**, 802 (1990).

[26] T. Borca-Tasciuc, a. R. Kumar, G. Chen, Data reduction in 3ω method for thin-film thermal conductivity determination, *Rev. Sci. Instrum.* **72**, 2139 (2001).

[27] D. G. Cahill *et al.*, Nanoscale thermal transport, *J. Appl. Phys.* **93**, 793 (2003).

[28] R. Nicklow, N. Wakabayashi, H. Smith, Lattice Dynamics of Pyrolytic Graphite, *Phys. Rev. B* **5**, 4951–4962 (1972).

[29] W. H. Press, S. A. Teukolsky, W. T. Vetterling, B. P. Flannery, *Numerical Recipes* (Cambridge University Press, New York, ed. 3rd, 2007), p. 807.

[30] P. G. KLEMENS, Theory of the a-Plane Thermal Conductivity of Graphite, *J. Wide Bandgap Mater.* **7**, 332–339 (2000).

[31] P. G. Klemens, D. F. Pedraza, Thermal conductivity of graphite in the basal plane, *Carbon N. Y.* **32**, 735–741 (1994).

[32] G. Slack, Anisotropic Thermal Conductivity of Pyrolytic Graphite, *Phys. Rev.* **127**, 694–701 (1962).

[33] C. Dames, Theoretical phonon thermal conductivity of Si/Ge superlattice nanowires, *J. Appl. Phys.* **95**, 682 (2004).

[34] A. D. McConnell, K. E. Goodson, THERMAL CONDUCTION IN SILICON MICRO- AND NANOSTRUCTURES, *Annu. Rev. Heat Transf.* **14** (2005).

[35] J. M. Ziman, *Electrons and Phonons* (Oxford University Press, New York, 1960).

[36] F. Miao *et al.*, Phase-coherent transport in graphene quantum billiards., *Science* **317**, 1530–3 (2007).

[37] X. Li, X. Wang, L. Zhang, S. Lee, H. Dai, Chemically derived, ultrasmooth graphene nanoribbon semiconductors., *Science* **319**, 1229–32 (2008).

[38] Y.-M. Lin, P. Avouris, Strong suppression of electrical noise in bilayer graphene nanodevices., *Nano Lett.* **8**, 2119–25 (2008).

[39] A. J. Schmidt, X. Chen, G. Chen, Pulse accumulation, radial heat conduction, and anisotropic thermal conductivity in pump-probe transient thermoreflectance., *Rev. Sci. Instrum.* **79**, 114902 (2008).

[40] C. Yu *et al.*, Thermal Contact Resistance and Thermal Conductivity of a Carbon Nanofiber, *J. Heat Transfer* **128**, 234 (2006).

[41] E. Pop, D. A. Mann, K. E. Goodson, H. Dai, Electrical and thermal transport in metallic single-wall carbon nanotubes on insulating substrates, *J. Appl. Phys.* **101**, 093710 (2007).

[42] C. Dames, G. Chen, 1ω, 2ω, and 3ω Methods for Measurements of Thermal Properties, *Rev. Sci. Instrum.* **76**, 124902 (2005).

[43] A. K. Geim, K. S. Novoselov, The rise of graphene., *Nat. Mater.* **6**, 183–91 (2007).

[44] H.-K. Lyeo, D. Cahill, Thermal conductance of interfaces between highly dissimilar materials, *Phys. Rev. B* **73**, 144301 (2006).

[45] N. Snyder, Heat transport through helium II: Kapitza conductance, *Cryogenics (Guildf).* **10**, 89–95 (1970).

[46] J. C. Duda, J. L. Smoyer, P. M. Norris, P. E. Hopkins, Extension of the diffuse mismatch model for thermal boundary conductance between isotropic and anisotropic materials, *Appl. Phys. Lett.* **95**, 031912 (2009).

[47] R. Prasher, Thermal boundary resistance and thermal conductivity of multiwalled carbon nanotubes, *Phys. Rev. B* **77**, 075424 (2008).

[48] M. Freitag *et al.*, Energy dissipation in graphene field-effect transistors., *Nano Lett.* **9**, 1883–8 (2009).

[49] R. Murali, Y. Yang, K. Brenner, T. Beck, J. D. Meindl, Breakdown current density of graphene nanoribbons, *Appl. Phys. Lett.* **94**, 243114 (2009).

[50] M. Asheghi, M. N. Touzelbaev, K. E. Goodson, Y. K. Leung, and S. S. Wong, Temperature- dependent thermal conductivity of single-crystal silicon layers in SOI substrates, *ASME J. Heat Transfer*, **120**:30–36, 1998.

[51] Y. K. Koh, M.-H. Bae, D. G. Cahill, E. Pop, Heat conduction across monolayer and few-layer graphenes., Nano Lett. **10**, 4363–8 (2010).

Chapter 3: An anisotropic Debye model for the thermal boundary conductance

[Reproduced with permission from Physical Review B 87, 125426 (2013)]

3.1 Introduction

Understanding and engineering the thermal boundary conductance (TBC, also discussed as a thermal boundary resistance or thermal contact resistance) across atomically-intimate interfaces is becoming increasingly important as the characteristic lengths of modern devices continue shrinking to micro- and nano- scales [1]. Nearly all models for the TBC, such as the widely-used diffuse mismatch model (DMM) and acoustic mismatch model (AMM) [2], require that the materials have isotropic properties, and are most commonly based on an isotropic Debye dispersion relation. However, many important materials are highly anisotropic, including layered materials such as graphite, boron nitride, and Bi_2Te_3, and chain-like materials such as high density polyethylene (HDPE). In such highly anisotropic materials, the conventional isotropic Debye model is no longer a good approximation. For example, in graphite at intermediate temperatures the predictions of the isotropic Debye model deviate from the experimental data for the specific heat capacity by more than a factor of two [3-4], and, as will be shown below, compared to the measured TBC between graphite and metals [5], DMM calculations using an isotropic Debye model are typically in error by more than a factor of 10.

For the special case of interfaces involving graphite, recently two anisotropic TBC models were reported. Prasher [6] used the DMM to model the TBC between graphite and platinum below 100 K using the aniostropic graphite dispersion from Komatsu [7]. Also using the DMM, Duda *et al.* [8] modeled the TBC between graphite and aluminum by approximating graphite's density of states (DOS) as two-dimensional (2D). In both cases the modeled TBC was found to be lower for interfaces oriented parallel to graphite's *ab*-planes (also called basal planes), which was attributed to the fact that the sound velocity is much lower in the *c*-axis direction than along the *ab*-planes. Because these models [6, 8] were developed specifically for graphite, they are difficult to generalize to other anisotropic materials.

In this chapter we develop a general framework for the TBC using an anisotropic Debye phonon dispersion, whereby the first Brillouin zone and the iso-energy surfaces are both generalized from spherical to ellipsoidal. We restrict the analysis to materials where only one of the three principle directions is anisotropic; that is, materials with tetragonal, trigonal, or hexagonal symmetries. This restriction is appropriate for a large number of layered and chain-like materials, including graphite, boron nitride, Bi_2Te_3, HDPE, and tellurium. This chapter is organized as follows. In Section 3.2 we present the two basic assumptions of the framework and derive an expression for the TBC, include simple analytical expressions for several limiting cases. The specific heat capacity is also discussed. Then in Section 3.3 we compare the model to experimental results from the literature for the specific heat of a typical layered (graphite) and chain-like (HDPE)

material, and for the TBC between graphite and various metals. Finally we summarize this chapter in Section 3.4, and leave some detailed derivations in Section 3.5.

3.2 Description of model

3.2.1 Basic assumptions and justifications

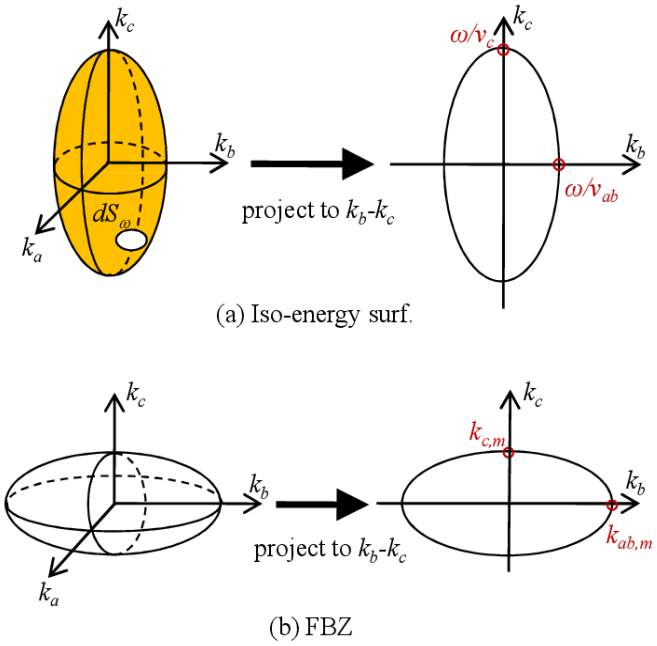

Figure 3-1. (a) Iso-energy surface (here for $v_{ab} > v_c$; the opposite case is straightforward). The ellipsoidal surface has an equatorial radius ω/v_{ab} and polar radius ω/v_c. Its k_b-k_c projection is an ellipse. (b) FBZ (here for $k_{ab,m} > k_{c,m}$; the opposite case is straightforward) with equatorial radius $k_{ab,m}$ and polar radius $k_{c,m}$. Its k_b-k_c projection is also an ellipse.

The first key assumption of this model is that a material's anisotropic phonon dispersion can be well approximated by the anisotropic Debye dispersion, $\omega^2 = v_a^2 k_a^2 + v_b^2 k_b^2 + v_c^2 k_c^2$, where v_a, v_b and v_c are the sound velocities along the *a*-, *b*- and *c*-axis directions respectively, and (k_a, k_b, k_c) is the wavevector. This dispersion has ellipsoidal iso-energy surfaces in *k*-space [Fig. 3-1(a)]. Because in this work we focus on materials with $v_a = v_b = v_{ab}$, this simplifies to

$$\omega^2 = v_{ab}^2 k_{ab}^2 + v_c^2 k_c^2, \tag{3-1}$$

where $k_{ab}^2 = k_a^2 + k_b^2$.

The other key assumption is that an anisotropic material's first Brillouin zone (FBZ) can be adequately approximated by an ellipsoid [Fig. 3-1(b)], an obvious

generalization of the spherical FBZ used in the classic isotropic Debye model. Here the FBZ ellipsoid is defined as the surface satisfying $\frac{k_a^2}{k_{a,m}^2}+\frac{k_b^2}{k_{b,m}^2}+\frac{k_c^2}{k_{c,m}^2}=1$, where $k_{a,m}$, $k_{b,m}$, and $k_{c,m}$ are wavevector cutoffs. Because we focus on materials with restricted symmetries such that $k_{a,m}=k_{b,m}=k_{ab,m}$, this can be written

$$\frac{k_{ab}^2}{k_{ab,m}^2}+\frac{k_c^2}{k_{c,m}^2}=1. \tag{3-2}$$

To ensure the correct total number of acoustic modes, these wavevector cutoffs are constrained by the number density of primitive unit cells, η_{puc}, through

$$\eta_{puc}=\tfrac{1}{6\pi^2}k_{ab,m}^2 k_{c,m}. \tag{3-3}$$

The number of optical modes is given by $\eta_{opt.}=3(m-1)\eta_{puc}$, where m is the number of atoms in the crystal basis. For simplicity we approximate them as Einstein modes, making their contributions to heat transfer vanish.

We now comment briefly on the validity of this anisotropic Debye approximation. The form of Eq. (3-1) is motivated by an exact result from continuum elasticity [9-11], in which the dispersion relation for the pure transverse acoustic (pure-TA) branch of materials with hexagonal symmetry can be written as

$$\rho\omega^2=C_{66}k_{ab}^2+C_{44}k_c^2, \tag{3-4}$$

where ρ is the mass density and C_{ij} is stiffness constant. Although the dispersion relations for both the quasi-longitudinal acoustic (quasi-LA) and the quasi-transverse acoustic (quasi-TA) branches have more complicated angular dependencies [11], under certain conditions they also are well approximated by the form of Eq. (3-4) using different C_{ij} (details in Section 3.3.1). Graphite is a typical example satisfying these conditions. However, this anisotropic Debye approximation cannot capture the variation of the phase velocity with the magnitude of the wavevector in real materials, which arises purely from atomistic effects [12]. For example, the present model cannot capture the curvature of the well known flexural (ZA, also called $TA_\perp$ [13] or oTA [14]) branch in graphite, which has been given by Lifshitz as [12,15]

$$\rho\omega^2=C_{44}k_{ab}^2+C_{33}k_c^2+\frac{B}{d}k_{ab}^4, \tag{3-5}$$

where B is related to the bond-bending stiffness of an isolated graphene layer and d is the interlayer distance. The last term in Eq. (3-5) is a subcontinuum effect, which can be formally neglected if $k_{ab}^2 << C_{44}d/B$. Similar considerations apply to chain-like materials and the bond-bending stiffness of individual atomic chains [12].

Comparing the anisotropic Debye model of Eq. (3-1) to the real dispersion of a typical layered material, graphite [16], we estimate that for all three acoustic branches (LA, TA, ZA) the present model is in error by typically tens of percent for variations in ω with the magnitude of $\mathbf{k}$ in any fixed direction. This shortcoming is offset, however, by the merit of the model in capturing the large variations of ω with the direction of $\mathbf{k}$, which is the emphasis of the present work. These directional variations can be substantial: for example $\mathbf{v}_g$ in graphite changes by a factor of approximately 5 to 10 as estimated by comparing the sound velocity in the *ab*-plane to that along the *c*-axis. Section 3.3 will show this anisotropic Debye approximation compares favorably with experimental values of the specific heat and a more detailed lattice dynamics calculation of phonon irradiation, typically to within ±10% over the temperature range 200 to 2,000K.

3.2.2 Characteristic frequencies and temperatures

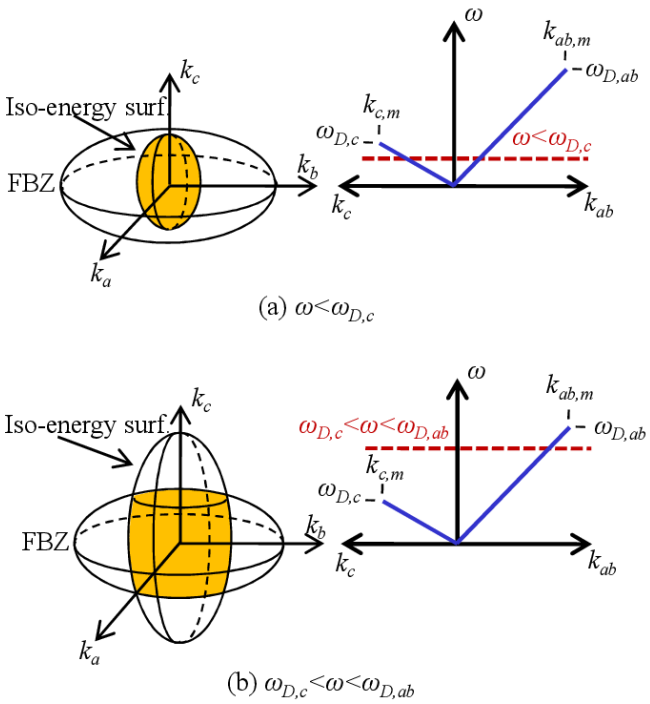

Figure 3-2. Two frequency regimes (here for $v_{ab} > v_c$, and $k_{ab,m} > k_{c,m}$; the other combinations are straightforward). (a) When $\omega < \min\left(\omega_{D,c}, \omega_{D,ab}\right)$, all of the states on the iso-energy surface are allowed. (b) When $\min\left(\omega_{D,c}, \omega_{D,ab}\right) < \omega < \max\left(\omega_{D,c}, \omega_{D,ab}\right)$, only the states inside the FBZ are allowed. In both cases the orange shading indicates the allowed states.

Based on the ellipsoidal dispersion relation and FBZ, we define the characteristic Debye frequencies of the *ab*-plane and *c*-axis directions,

$$\begin{aligned} \omega_{D,ab} &= v_{ab} k_{ab,m} \\ \omega_{D,c} &= v_c k_{c,m} \end{aligned}, \tag{3-6}$$

with corresponding Debye temperatures

$$\begin{aligned} \theta_{D,ab} &= \hbar\omega_{D,ab} / k_B \\ \theta_{D,c} &= \hbar\omega_{D,c} / k_B \end{aligned}, \tag{3-7}$$

where $\hbar$ is the reduced Planck's constant and k_B is the Boltzmann constant. It will also prove convenient to define the anisotropy ratio

$$r = \frac{\omega_{D,ab}}{\omega_{D,c}} = \frac{\theta_{D,ab}}{\theta_{D,c}}. \tag{3-8}$$

We refer to materials with $r > 1$ as "layered," and $r < 1$ as "chain-like." Thus graphite ($r >> 1$) is strongly layered, while HDPE is strongly chain-like ($r << 1$).

The definitions of Eqs. (3-6)-(3-8) facilitate the upcoming analysis by distinguishing between two different frequency regimes, as shown in Fig. 3-2. First, for those modes with $\omega < \min\left(\omega_{D,c}, \omega_{D,ab}\right)$, the iso-energy surface has not reached the FBZ boundary, so all of those states are allowed as indicated by orange shading in Fig. 3-2(a). Second, for those modes with $\min\left(\omega_{D,c}, \omega_{D,ab}\right) < \omega < \max\left(\omega_{D,c}, \omega_{D,ab}\right)$, part of the iso-energy surface lies outside of the FBZ, so only the part inside the FBZ is allowed [orange shading in Fig. 3-2(b)].

3.2.3 Specific heat

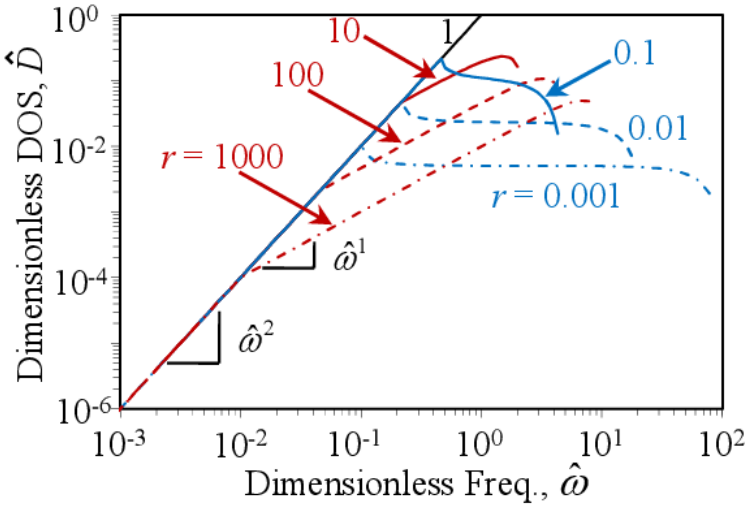

Figure 3-3. Dimensionless DOS, $\hat{D} = D\left(\omega_{D,ab}^2 \omega_{D,c}\right)^{\frac{1}{3}} \Big/ \left(3\eta_{puc}\right)$, as a function of dimensionless frequency $\hat{\omega} = \omega \Big/ \left(\omega_{D,ab}^2 \omega_{D,c}\right)^{\frac{1}{3}}$. While layered materials (r >> 1) show a transition from a quadratic to a linear power law with increasing ω, chain-like materials (r << 1) show a transition from a quadratic power law to a constant value. These transitions indicate different dimensionality crossovers.

The phonon specific heat is given by

$$C = \sum_{pol} \int \hbar\omega \frac{\partial f_{BE}}{\partial T} D(\omega) d\omega \,, \tag{3-9}$$

where the sum runs over all polarizations, f_{BE} is the Bose-Einstein distribution function, and $D(\omega)$ is the DOS which for an arbitrary dispersion relation is given by [17]

$$D(\omega) = \frac{1}{8\pi^3} \iint \frac{dS_\omega}{\|\mathbf{v}_g\|}, \tag{3-10}$$

where dS_ω is an elemental area on an iso-energy surface in k-space [Fig. 3-1(a)]. For the anisotropic Debye model defined by Eqs. (3-1) and (3-2), the analytical expression of DOS is conveniently evaluated in two regimes depending on the anisotropy ratio r (details in Appendix A).

In Fig. 3-3, we plot the dimensionless density of states $\hat{D} = D\left(\omega_{D,ab}^2 \omega_{D,c}\right)^{\frac{1}{3}} \Big/ \left(3\eta_{puc}\right)$ as a function of the dimensionless frequency $\hat{\omega} = \omega \Big/ \left(\omega_{D,ab}^2 \omega_{D,c}\right)^{\frac{1}{3}}$ for a single polarization. The key feature is the range of power laws describing $\hat{D}$ versus $\hat{\omega}$. The isotropic "control" case (r = 1) follows the well-known quadratic power law over the entire frequency range. Layered materials (r >> 1) show a

transition from a quadratic to a linear power law with increasing ω, which can be interpreted by the scenario depicted in Fig. 3-2(b). This transition indicates a dimensionality crossover from 3D to 2D as the *c*-axis modes become fully saturated at large ω. Chain-like materials ($r << 1$), on the other hand, show a transition from a quadratic power law to a constant value with increasing ω, indicating a dimensionality crossover from 3D to 1D.

Substituting Eqs. (3-31) and (3-32) into Eq. (3-9), we obtain two integral expressions for the specific heat in terms of $x = \hbar\omega/k_B T$. For $r > 1$,

$$C = \sum_{pol} \frac{k_B^4}{2\pi^2 v_{ab}^2 v_c \hbar^3} \left[\int_0^{x_{D,c}} \frac{T^3 x^4 e^x}{\left(e^x - 1\right)^2} dx + \int_{x_{D,c}}^{x_{D,ab}} \frac{T^2 x^3 e^x}{\left(e^x - 1\right)^2} \sqrt{\theta_{D,c}^2 \frac{\theta_{D,ab}^2 - (Tx)^2}{\theta_{D,ab}^2 - \theta_{D,c}^2}} dx \right], \tag{3-11a}$$

while for $r < 1$,

$$C = \sum_{pol} \frac{k_B^4}{2\pi^2 v_{ab}^2 v_c \hbar^3} \left\{ \int_0^{x_{D,ab}} \frac{T^3 x^4 e^x}{\left(e^x - 1\right)^2} dx + \int_{x_{D,ab}}^{x_{D,c}} \left[\frac{T^3 x^4 e^x}{\left(e^x - 1\right)^2} - \frac{T^2 x^3 e^x}{\left(e^x - 1\right)^2} \sqrt{\theta_{D,c}^2 \frac{(Tx)^2 - \theta_{D,ab}^2}{\theta_{D,c}^2 - \theta_{D,ab}^2}} \right] dx \right\}. \tag{3-11b}$$

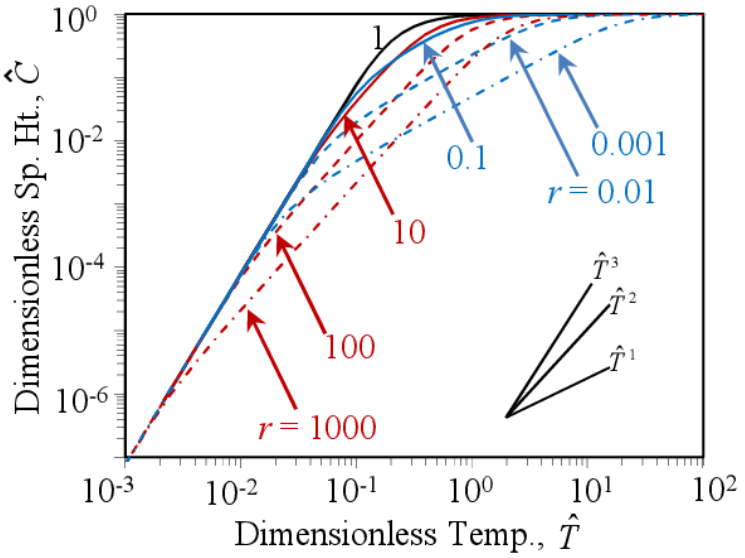

Figure 3-4. Dimensionless specific heat, $\hat{C} = C/\left(3\eta_{puc} k_B\right)$, as a function of dimensionless temperature, $\hat{T} = T/\left(\theta_{D,ab}^2 \theta_{D,c}\right)^{\frac{1}{3}}$, obtained by numerical integration of Eqs. (3-11a) and (3-11b). All materials recover the Debye T^3 law at low T, and Dulong and Petit limit at high T. But at intermediate temperatures the layered

materials ($r >> 1$) show a T^2 dependence, while the chain-like materials ($r << 1$) show a T^1 dependence.

Low T $T \ll \min(\theta_{D,c}, \theta_{D,ab})$	$C_{LowT} = \frac{2\pi^2 k_B^4}{15\hbar^3} \sum_{pol} \frac{T^3}{v_{ab}^2 v_c}$	
Intermediate T $\min(\theta_{D,c}, \theta_{D,ab}) \ll T \ll \max(\theta_{D,c}, \theta_{D,ab})$	Layered ($r >> 1$) $C_{Layer-Mid.T} = \frac{3\zeta_3 k_B^3 k_{c,m}}{\pi^2 \hbar^2} \sum_{pol} \frac{T^2}{v_{ab}^2}$	Chain-like ($r << 1$) $C_{Chain-Mid.T} = \frac{k_{ab,m}^2 k_B^2}{12 v_c \hbar} \sum_{pol} \frac{T}{v_c}$
High T $T \gg \max(\theta_{D,c}, \theta_{D,ab})$	$C_{HighT} = 3\eta_{puc} k_B$	

Table 3-1. Analytical expressions for the specific heat in several limiting cases. The model recovers the Debye T^3 law in the low temperature limit, and the Dulong and Petit law in the high temperature limit. For strongly anisotropic materials at intermediate temperatures, the model predicts a T^2 dependence and T^1 dependence for layered ($r >> 1$) and chain-like ($r << 1$) materials, respectively. $\zeta_3 = 1.202...$ is Apery's constant.

In both Eqs. (3-11a) and (3-11b), the first integral is the exact result for a traditional isotropic Debye solid, while the second integral captures the effects of anisotropy. Figure 3-4 shows the dimensionless specific heat $\hat{C} = C \Big/ \left(3\eta_{puc} k_B\right)$ versus the dimensionless temperature $\hat{T} = T \Big/ \left(\theta_{D,ab}^2 \theta_{D,c}\right)^{\frac{1}{3}}$, calculated by numerical integration of Eqs. (3-11a) and (3-11b). Layered materials ($r >> 1$) exhibit a transition from $T^3 \rightarrow T^2 \rightarrow T^0$ behavior with increasing T, while chain-like materials with $r << 1$ exhibit a transition from $T^3 \rightarrow T^1 \rightarrow T^0$. We will come back to these transitions in Section 3.3.2 when comparing this model to the experimental specific heat of graphite and prior models.

To gain further physical insight, in Table 3-1 we simplify Eqs. (3-11a) and (3-11b) in several limiting cases. First, in the low temperature limit [$T = \min(\theta_{D,c}, \theta_{D,ab})$], only low energy phonons are activated, in which case the FBZ boundaries are far away from the iso-energy surfaces [Fig. 3-1(a)]. Therefore the analytical expression recovers the classic Debye T^3 law and depends on the two sound velocities, but not the two wavevector cutoffs because the phonon wavelengths are insensitive to the granularity of the lattice in this limit. On the other hand, in the high temperature limit [$T \gg \max(\theta_{D,c}, \theta_{D,ab})$], all of the phonons are full activated and obey equipartition of energy, and thus the analytical expression recovers the Dulong and Petit result, and depends on the two wavevector cutoffs (related to the total number of phonon modes) but not the sound velocities.

At intermediate temperatures [$\min(\theta_{D,c}, \theta_{D,ab}) = T = \max(\theta_{D,c}, \theta_{D,ab})$], Table 3-1 shows that strongly anisotropic materials exhibit a mixture of the high-T and low-T behaviors just described. At intermediate T, the populated iso-energy surfaces reach the FBZ boundary along the crystal direction of low sound velocity, while remaining far from the FBZ boundary along the direction of fast sound velocity [Fig. 3-1(b)].

Therefore the slow-velocity direction is saturated in its high-T regime while the fast-velocity direction is still in its low-T regime. Thus the limiting analytical expression for a layered material at intermediate temperature follows a T^2 power law, and depends on v_{ab} and $k_{c,m}$ but not v_c or $k_{ab,m}$. Conversely, a chain-like material follows a T^1 law, and depends on v_c and $k_{ab,m}$ but not v_{ab} or $k_{c,m}$. These intermediate T behaviors are further justified in Appendix B through an alternative derivation using simplified 2D and 1D phonon gas models.

3.2.4 Phonon irradiation

We calculate the irradiation and TBC using the close analogy between phonon transport and photon radiation. We restrict the analysis to interfaces oriented normal to the material's c-axis, the configuration of highest symmetry, because this simplifies the analysis and it is also a common configuration in applications and experiments [5]. For materials with isotropic properties, the "incident radiation" [Eq. (6) of Ref. 18] is a convenient quantity for evaluating the TBC. However, to accommodate materials with anisotropic properties, the phonon "irradiation" is a better choice. A general expression for the irradiation along the c-axis is

$$H_c = \sum_{pol} \iiint_{\mathbf{k}\cdot\hat{\mathbf{c}}<0} I\ \hat{\mathbf{s}}\cdot\hat{\mathbf{c}}\ d^3\mathbf{k}, \tag{3-12}$$

where $\hat{\mathbf{c}} = (0,0,1)$ is the unit vector along the c-axis, $\hat{\mathbf{s}}$ is a unit vector parallel to the group velocity, $\mathbf{k}\cdot\hat{\mathbf{c}} < 0$ denotes integration over the incident half-space, and the intensity $I = \frac{1}{8\pi^3}\hbar\omega\left\|\mathbf{v}_g\right\| f_{BE}$ at wavevector $\mathbf{k}$ travels in the $\hat{\mathbf{s}}$ direction.

It is helpful to convert Eq. (3-12) to an integral over frequency,

$$H_c = \sum_{pol}\int_{\omega} \hbar\omega\ h_c f_{BE} d\omega, \tag{3-13}$$

where we introduce a new quantity, h_c, which can be understood as the density of states [Eq. (3-10)] weighted by the c-axis projected velocity:

$$h_c(\omega) = \frac{1}{8\pi^3}\iint_{\hat{\mathbf{s}}\cdot\hat{\mathbf{c}}<0} \frac{\left(\mathbf{v}_g\cdot\hat{\mathbf{c}}\right)}{\left\|\mathbf{v}_g\right\|} dS_\omega. \tag{3-14}$$

Thus, h_c represents the product of the phonon velocity component along the direction of heat transfer (here, $\hat{\mathbf{c}}$) and the number of phonon modes per unit frequency between ω and $\omega + d\omega$, integrated over the incident half-FBZ. We refer to h_c as the vDOS (v indicating velocity-weighted), and its role in the irradiation [Eq. (3-13)] is analogous to the role of the DOS in the specific heat [Eq. (3-9)]. Analytical expressions for the vDOS are given in Appendix A.

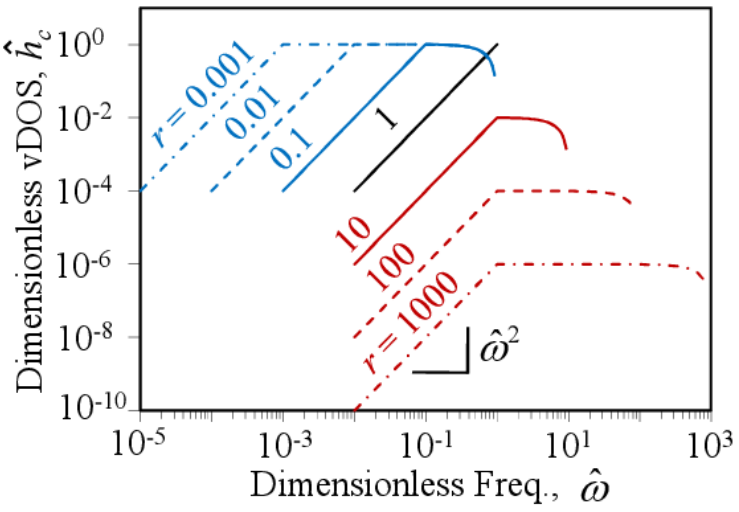

Figure 3-5. Dimensionless vDOS defined in Eq. (3-14), $\hat{h}_c = h_c \omega_{D,c} \big/ \left(3\eta_{puc} v_c / 4\right)$, as a function of dimensionless frequency, $\hat{\omega} = \omega / \omega_{D,c}$. Both layered ($r >> 1$) and chain-like ($r << 1$) materials transition from a quadratic power law at low frequency to a constant value at high frequency.

Figure 3-5 shows the dimensionless vDOS, $\hat{h}_c = h_c \omega_{D,c} \big/ \left(3\eta_{puc} v_c / 4\right)$, versus the dimensionless frequency, $\hat{\omega} = \omega / \omega_{D,c}$, for a single polarization. Both layered and chain-like materials show a transition from a $\hat{\omega}^2$ dependence at low frequency to a constant value at high frequency. The low frequency behavior is straightforward from Eqs. (3-33) and (3-34) of Appendix A, and the high frequency behavior can be understood from the definition of h_c [Eq. (3-14)]: an averaged product of DOS [Eq. (3-10)] and the *c*-axis component of the group velocity. For layered materials, the high frequency DOS is 2D and thus proportional to ω (Fig. 3-3), and as shown in Appendix B the frequency-dependent *c*-axis component of the group velocity scales as $v_{g,c,2D} \propto \omega^{-1}$. However, for chain-like materials, the high frequency DOS is 1D and thus constant while $v_{g,c,1D} \propto \omega^0$ (Appendix B).

Substituting Eqs. (3-33) and (3-34) into Eq. (3-13), we obtain expressions for the irradiation. For $r > 1$,

$$H_c = \sum_{pol} \frac{k_B^4}{8\pi^2 v_{ab}^2 \hbar^3} \left\{ \int_0^{x_{D,c}} \frac{T^4 x^3}{e^x - 1} dx + \int_{x_{D,c}}^{x_{D,ab}} \left[\frac{\theta_{D,ab}^2 \theta_{D,c}^2}{\theta_{D,ab}^2 - \theta_{D,c}^2} \frac{T^2 x}{e^x - 1} - \frac{\theta_{D,c}^2}{\theta_{D,ab}^2 - \theta_{D,c}^2} \frac{T^4 x^3}{e^x - 1} \right] dx \right\}, \qquad (3\text{-}15a)$$

while for $r < 1$,

$$H_c = \sum_{pol} \frac{k_B^4}{8\pi^2 v_{ab}^2 \hbar^3} \left\{ \int_0^{x_{D,ab}} \frac{T^4 x^3}{e^x - 1} dx + \int_{x_{D,ab}}^{x_{D,c}} \left[\frac{\theta_{D,c}^2 \theta_{D,ab}^2}{\theta_{D,c}^2 - \theta_{D,ab}^2} \frac{T^2 x}{e^x - 1} - \frac{\theta_{D,ab}^2}{\theta_{D,c}^2 - \theta_{D,ab}^2} \frac{T^4 x^3}{e^x - 1} \right] dx \right\}. \qquad (3\text{-}15b)$$

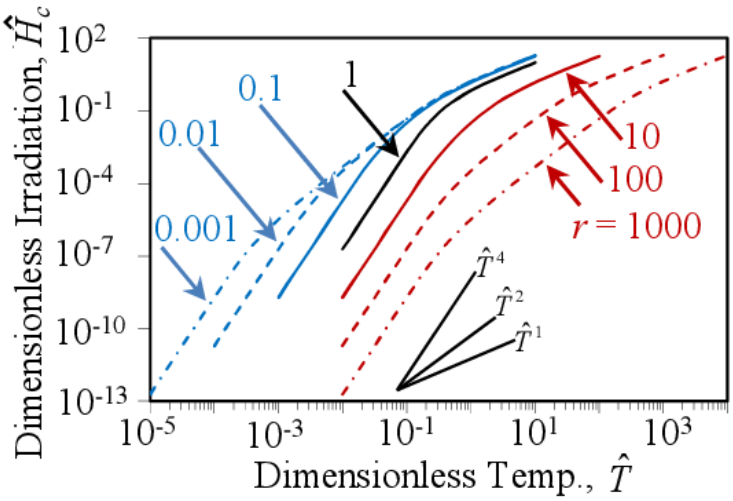

Figure 3-6. Dimensionless *c*-axis irradiation, $\hat{H}_c = H_c \big/ \left(3\eta_{puc} k_B v_c \theta_{D,c} / 4\right)$, as a function of dimensionless temperature, $\hat{T} = T/\theta_{D,c}$, obtained by numerical integration of Eqs. (3-15a) and (3-15b). Both layered ($r >> 1$) and chain-like ($r << 1$) materials show $T^4 \rightarrow T^2 \rightarrow T^1$ power law transitions.

The first integral of Eqs. (3-15a) and (3-15b) is the exact result for a traditional isotropic Debye solid, while the second integral captures the effects of anisotropy. In Fig. 3-6 we plot the dimensionless irradiation $\hat{H}_c = H_c \big/ \left(3\eta_{puc} k_B v_c \theta_{D,c} / 4\right)$ versus the dimensionless temperature $\hat{T} = T/\theta_{D,c}$. Both layered ($r >> 1$) and chain-like ($r << 1$) materials show a $T^4 \rightarrow T^2 \rightarrow T^1$ transition with increasing T.

Low T $T \ll \min(\theta_{D,c}, \theta_{D,ab})$	$H_{c-LowT} = \sigma_{phonon} T^4 = \left[\dfrac{\pi^2 k_B^4}{120\hbar^3} \sum_{pol} \dfrac{1}{v_{ab}^2}\right] T^4$	
Intermediate T $\min(\theta_{D,c}, \theta_{D,ab}) \ll T \ll \max(\theta_{D,c}, \theta_{D,ab})$	Layered ($r >> 1$) $H_{c-Layer-Mid.T} = \dfrac{k_{c,m}^2 k_B^2 T^2}{48\hbar} \sum_{pol} \dfrac{v_c^2}{v_{ab}^2}$	Chain-like ($r << 1$) $H_{c-Chain-Mid.T} = \dfrac{k_{ab,m}^2 k_B^2 T^2}{16\hbar}$
High T $T \gg \max(\theta_{D,c}, \theta_{D,ab})$	$H_{c-HighT} = \frac{1}{2} \eta_{puc} k_B T \sum_{pol} \dfrac{v_c k_{c,m}}{v_{ab} k_{ab,m} + v_c k_{c,m}} v_c$	

Table 3-2. Analytical expressions for the *c*-axis irradiation H_c in several limiting cases. In the low temperature limit the model reduces to the blackbody emissive power law. For intermediate temperatures and strongly anisotropic materials, the model predicts a T^2 dependence for both layered and chain-like materials. These expressions also highlight the phonon focusing effect of the *ab*-plane velocity v_{ab}: except for chain-like materials at intermediate *T*, in all other cases H_c is actually increased by reducing v_{ab}.

For further physical insight, Table 3-2 presents simplifications of Eqs. (3-15a) and (3-15b) for several limiting cases. In the low temperature limit, regardless of *r* Eqs. (3-15a) and (3-15b) reduce to the well-known blackbody emissive power law with a phonon Stephen-Boltzmann constant $\sigma_{phonon} = \pi^2 k_B^4 \left(\sum_{pol} v_{ab}^{-2} \right) \Big/ \left(120 \hbar^3 \right)$ [19]. In the limit of strongly anisotropic materials at intermediate temperatures, Table 3-2 shows that both layered and chain-like materials follow a T^2 power law, which arises from the power law $\hat{h}_c \propto \hat{\omega}$ (Fig. 3-5). These intermediate temperature behaviors are further justified in Appendix B using simplified 2D and 1D phonon gas models.

Table 3-2 reveals the unexpected result that the *c*-axis irradiation H_c is generally *increased* by *reducing* the *ab*-plane sound velocity v_{ab} (the only exception being chain-like materials at intermediate *T*, for which H_c has no velocity dependence at all). This v_{ab} dependence of H_c can be understood as a consequence of phonon focusing [20-22]. As can be seen from Fig. 3-1(a), reducing v_{ab} elongates the iso-energy surfaces ("slowness surfaces" in Ref. 20) along the *ab*-plane, thus increasing the component of the group velocity along the *c*-axis direction and correspondingly increasing H_c. This suggests a surprising guideline for materials engineering to increase TBC: the heat transfer along the *c*-axis direction can be *increased* by *reducing* a phonon velocity, as long as it is a velocity component perpendicular to the *c*-axis. The analogous effect on the thermal conductivity of highly anisotropic materials has also been reported [23-25]. For example, a hybrid model [22] (lattice dynamics + molecular dynamics) confirmed that the thermal conductivity in the *c*-axis direction of a graphite-like material is also increased by reducing the *ab*-plane phonon velocity, caused in part by the same phonon focusing effects of interest here. In Section 3.3, we will examine this anticipated H_c dependence of the TBC further for two particular models of transmission coefficient.

3.2.5 Thermal boundary conductance

From traditional radiative heat transfer [26], the net heat flux across an interface between materials A and B can be expressed as

$$q = \tau \left[H_A(T_1) t_{AB}(T_1) - H_B(T_2) t_{BA}(T_2) \right], \tag{3-16}$$

where t_{AB} is an average (with respect to direction, position, energy, and polarization) transmission coefficient from A to B, T_1 and T_2 are the local equilibrium temperatures on either side of the interface, and the pre-factor

$$\tau = \frac{1}{1 - \frac{1}{2}\left[t_{AB}(T_1) + t_{BA}(T_2) \right]} \tag{3-17}$$

arises because we work in terms of equilibrium rather than emitted temperatures (Appendix C) [18, 27].

When the system is at equilibrium at temperature T, the 2nd Law of Thermodynamics requires $q = 0$ and thus [2, 18, 28] from Eq. (3-16)

$$H_A(T)t_{AB}(T) = H_B(T)t_{BA}(T). \tag{3-18}$$

Substituting Eq. (3-18) into Eq. (3-16), and expanding q as a Taylor series in $\Delta T = T_1 - T_2$, we obtain an expression for the thermal boundary conductance defined as $G = \lim_{\Delta T \to 0}\left(q/\Delta T\right)$:

$$G = \tau\left[\frac{\partial H_i}{\partial T}t_{ij} + \frac{\partial t_{ij}}{\partial T}H_i\right], \tag{3-19}$$

where $i, j = A, B$ or equivalently B, A.

We note in passing that the TBC obtained from the limit $\Delta T \to 0$ must be always symmetric upon exchanging the labels A and B. Thus, there cannot be any rectification in this low-bias regime, regardless of the model of the transmission coefficient. Although some analyses may neglect the second term of Eq. (3-19), such an approximation can have the side effect of incorrectly implying thermal rectification [29].

3.3 Comparison with experiments

3.3.1 Specifying input parameters

A. Wavevector cutoffs: $k_{ab,m}$ and $k_{c,m}$

Given η_{puc} for a real material, Eq. (3-3) sets the first constraint for the two wavevector cutoffs, and as the second constraint we choose to fix the anisotropy ratio:

$$\frac{k_{ab,m}}{k_{c,m}} = \frac{k_{ab,m,exp.}}{k_{c,m,exp.}}, \tag{3-20}$$

where $k_{ab,m,exp.}$ and $k_{c,m,exp.}$ are wavevector cutoffs consistent with the experimentally-determined crystallographic structure. For example, one simple way to fix the $k_{m,exp.}$ values is from the reported extents of the FBZ in the [100], [010], and/or [001] directions.

B. Sound velocities

We have used two different approaches to obtain the six sound velocities (3 polarizations each of v_{ab} and v_c). The first and easiest approach is to use experimentally-measured values along suitable high symmetry directions in the *ab*-plane and along the *c*-axis. For materials for which the full phonon dispersion relation is available a second approach is a "secant" method, in which case the sound velocity for a specified branch and direction is set to be equal to the slope of the secant that connects the Γ point and the end point of that branch at the FBZ boundary.

Although we could easily calculate the specific heat by summing over each branch (LA, TA_1, TA_2), for simplicity and physical insight it is also helpful to lump these six velocities into two effective ones, $v_{ab,eff.}$ and $v_{c,eff.}$, requiring two more equations. For the first constraint we insist on the correct low T behavior of the specific heat from Table 3-1, leading to

$$\frac{3}{v_{ab,eff.}^2 v_{c,eff.}} = \sum_{pol} \frac{1}{v_{ab}^2 v_c}. \tag{3-21}$$

Similarly, for the second constraint we require the correct intermediate T behavior from Table 3-1. For layered materials this gives

$$\frac{3}{v_{ab,eff.}^2} = \sum_{pol} \frac{1}{v_{ab}^2}, \tag{3-22a}$$

while for chain-like materials we find

$$\frac{3}{v_{c,eff.}} = \sum_{pol} \frac{1}{v_c}, \tag{3-22b}$$

Note that Eq. (3-21) is exact for all materials, but Eqs. (3-22a) and (3-22b) are exact only for highly anisotropic materials.

C. Decomposition of iso-energy surfaces for materials with hexagonal symmetry

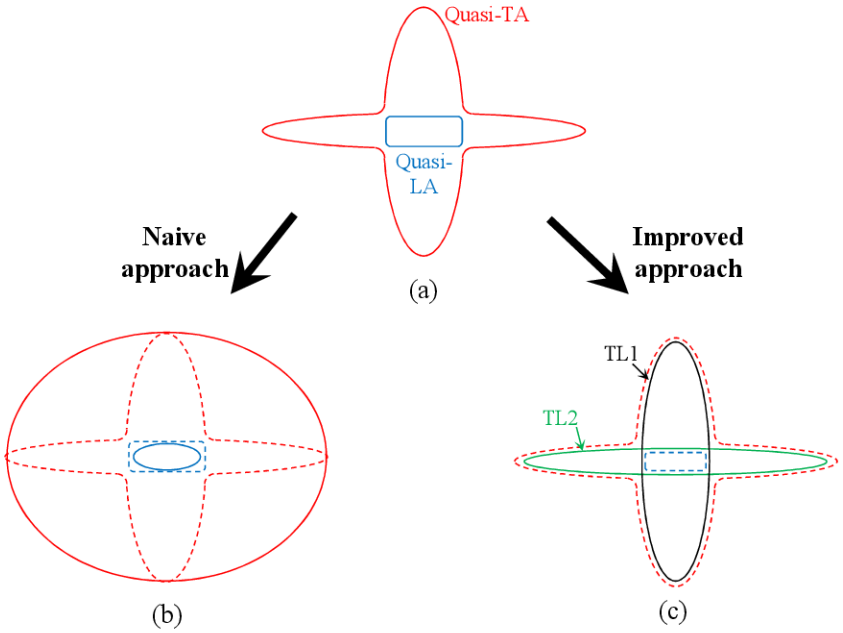

Figure 3-7. Debye ellipsoid approximations for the iso-energy surfaces of materials with hexagonal symmetry. The schematics represent projections in the A-Γ-M plane (an A-Γ-K plane looks very similar). (a) Schematic iso-energy surfaces for a graphite-like material with a lobed quasi-TA branch and an almost cylindrical

quasi-LA branch. The third branch (pure TA) is not shown because it is already well-approximated by an ellipsoid (Eq. 3-4). (b) A naive approach approximates the quasi-TA with a circumscribed ellipsoid, and the quasi-LA with an inscribed ellipsoid. (c) An improved approach, used in this work, decomposes the quasi-TA and quasi-LA branches and then recomposes them as the two ellipsoids TL1 (black) and TL2 (green); see Eq. (3-25). The original and recomposed iso-energy surfaces in (c) have been offset slightly for clarity.

As discussed in Section 3.2.1, the exact dispersion relations of the quasi-TA and quasi-LA branches are more complicated than Eq. (3-1), whether evaluated by lattice dynamics [22] or continuum elasticity [Eqs. (3.11) and (3.12) in the appendix of Ref. 11]. For a strongly layered material like graphite, the typical shapes of the exact iso-energy surfaces are depicted in Fig. 3-7(a). In the A-Γ-M plane, the quasi-LA surface is nearly rectangular while the quasi-TA surface has four prominent lobes (an A-Γ-K slice looks very similar).

The task here is to determine the best approximation of these iso-energy surfaces with Debye ellipsoids such as Fig. 3-1(a), given the principal sound velocities. The obvious but naive approach is to approximate each branch with its own ellipsoid. As indicated in Fig. 3-7(b), this is equivalent to approximating the lobed quasi-TA branch with a circumscribed ellipsoid. Similarly, the quasi-LA would be replaced with an equivalent inscribed ellipsoid. As suggested by the graphical comparison of Fig. 3-7(b), these approximations appear quite crude and will introduce large errors in the phonon transport calculations. For example, for graphite at room-temperature, H_C calculated in this way is eight times too small as compared to that calculated using an all-direction lattice dynamics method as described in Appendix D.

A much improved approach is motivated by the exact dispersion relations of the quasi-TA and quasi-LA branches. From Eqs. (3.11) and (3.12) of the appendix of Auld [11], when $\left(\frac{C_{13}}{C_{44}}+1\right)^2 = \left(\frac{C_{11}}{C_{44}}-1\right)\left(\frac{C_{33}}{C_{44}}-1\right)$ it can be shown that

$$\omega^2_{quasi-TA} = \begin{cases} \frac{C_{11}}{\rho}k_{ab}^2 + \frac{C_{44}}{\rho}k_c^2 \ , & \left|\frac{k_{ab}}{k_c}\right| \le \sqrt{\frac{C_{33}-C_{44}}{C_{11}-C_{44}}} \\ \frac{C_{44}}{\rho}k_{ab}^2 + \frac{C_{33}}{\rho}k_c^2 \ , & \left|\frac{k_{ab}}{k_c}\right| \ge \sqrt{\frac{C_{33}-C_{44}}{C_{11}-C_{44}}} \end{cases}, \tag{3-23}$$

and

$$\omega^2_{quasi-LA} = \begin{cases} \frac{C_{11}}{\rho}k_{ab}^2 + \frac{C_{44}}{\rho}k_c^2 \ , & \left|\frac{k_{ab}}{k_c}\right| \ge \sqrt{\frac{C_{33}-C_{44}}{C_{11}-C_{44}}} \\ \frac{C_{44}}{\rho}k_{ab}^2 + \frac{C_{33}}{\rho}k_c^2 \ , & \left|\frac{k_{ab}}{k_c}\right| \le \sqrt{\frac{C_{33}-C_{44}}{C_{11}-C_{44}}} \end{cases}, \tag{3-24}$$

Graphite satisfies this very well $\left[\left(\frac{C_{13}}{C_{44}}+1\right)^2 \Big/ \left(\frac{C_{11}}{C_{44}}-1\right)\left(\frac{C_{33}}{C_{44}}-1\right) < 0.01\right]$. Noticing the complementary relation between Eqs. (3-23) and (3-24), we rewrite them as two new branches

$$\omega_{TL1}^2 = \frac{C_{11}}{\rho} k_{ab}^2 + \frac{C_{44}}{\rho} k_c^2$$
$$\omega_{TL2}^2 = \frac{C_{44}}{\rho} k_{ab}^2 + \frac{C_{33}}{\rho} k_c^2, \quad (3\text{-}25)$$

with the graphical interpretation given in Fig. 3-7(c): decompose the lobed quasi-TA branch and the curved quadrilateral quasi-LA branch, and recompose them as two ellipsoids. Now all three branches of materials with hexagonal symmetry have dispersions in the form Eq. (3-1), and thus ellipsoidal iso-energy surfaces. To help validate this ellipsoidal Debye approximation, in Appendix D we compare its H_c with that from a full lattice-dynamics calculation of a graphite-like material. As shown in Fig. 3-12 the two calculations agree very well, to within ±10% over a wide temperature range from 200 K to 10,000 K.

D. Contributions from optical phonons

For materials with a polyatomic basis we use an Einstein model to account for the contributions of optical phonons, with Einstein frequencies taken from the average of the experimentally-reported optical phonon frequencies at the Γ point and the edge of FBZ. Note that this treatment may be oversimplified for materials with complicated optical branches and/or optical phonons with large group velocities.

3.3.2 Specific heat of graphite

The specific heat of graphite has been well understood for decades both theoretically and experimentally [3-4, 7, 9, 12-13, 30], making this a useful check of the accuracy of the anisotropic Debye approximation used in the present work. Graphite is highly anisotropic (*r* ranging from 10 - 16 depending on the polarization) and also has relevance for its close cousins graphene and carbon nanotubes.

Parameter	Unit	*ab*-plane	*c*-axis
v_{TA}	m/s	10200	1000
v_{TL1}	m/s	16200	1000
v_{TL2}	m/s	6400	2500
k_{max}	10^{10}m^{-1}	1.73	1.1
$f_{E,LO/TO}$	THz	42	
$f_{E,ZO}$	THz	23	

Table 3-3. Input parameters for graphite, which are extracted from the phonon dispersion in Ref. 16 using the iso-energy-decomposition process described in Section 3.3.1.

Following the recipes outlined above, the input parameters are extracted from the published phonon dispersion [16] and summarized in Table 3-3. We assign the secant

velocity to all branches. In addition, to facilitate the analysis we unfold the dispersion relation along the *c*-axis direction [6]: in real space we cut the 4-atom-basis primitive unit cell in half along the *c*-axis to form a unit cell with a 2-atom-basis, and correspondingly in reciprocal space the wavevector cutoff $k_{c,m}$ is doubled. Only the *c*-axis direction was unfolded because the real dispersion relation [13, 16] in that direction is continuous at the FBZ boundary (e.g. TA→TO' and LA→LO' in Fig. 2 of Ref. 16), whereas along the ab plane the real dispersion relation shows some gaps at the FBZ boundary and has optical modes that are relatively slower compared to their acoustic counterparts.

The modeled specific heat of graphite is shown by the solid red line in Figure 3-8(a), and shows a transition from T^2 to T^0 behavior with increasing T as expected from Table 3-1 as well as from standard models such as Lifshitz [12]. The model accounts for contributions from both optical and acoustic phonons, and we confirmed that the contribution from electrons is negligible at the temperatures considered here. The optical contributions are shown by the dashed red line and use $f_{E,\,LO/TO}$ = 42 THz and $f_{E,\,ZO}$ = 23 THz. The acoustic contribution was calculated using both approaches described above: summing over all three polarizations and using the two effective velocities calculated from Eqs. (3-21) and (3-22a). The two calculations are nearly indistinguishable so only the former is shown in Fig. 3-8(a).

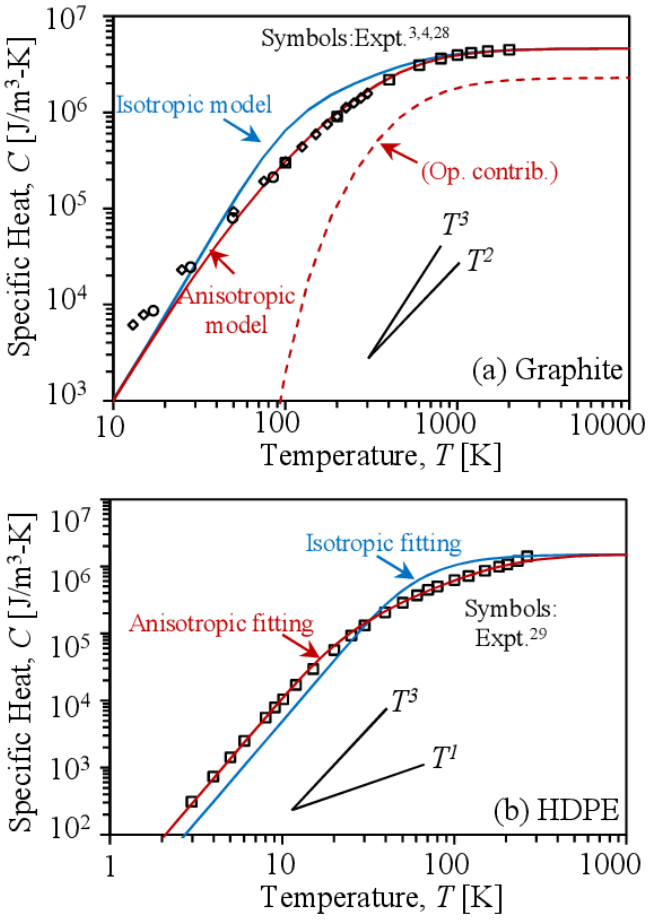

Figure 3-8. Comparison with experimental data for specific heat of (a) graphite and (b) HDPE, showing that the anisotropic Debye model successfully reproduces the specific heat of these strongly anisotropic materials. The model parameters for graphite are fully determined from the published dispersion relation without any fitting, while the HDPE model has two adjustable parameters because no published dispersion information was available.

The experimental specific heat of graphite [3-4, 31] is shown by the points in Fig. 3-8(a). With no free parameters the model agrees with the experimental data to within ±10% throughout the temperature range 50 – 2,000 K. However, below 20 K the model transitions to a T^3 power law, which is too steep as compared to the experimental data. This discrepancy is due to the oversimplification of linearizing the phonon dispersion of the ZA branch. The literature dispersion [13, 16] shows a monotonic decrease of the group velocity from 8500 m/s at the edge of the FBZ to approximately 1000 m/s at the Γ point. Therefore the secant method used here (6400 m/s) overestimates the velocity of small-wavevector ZA phonons which are the major contribution to the DOS at low temperatures, thereby underestimating their specific heat. A more detailed model dispersion such as Eq. (3-5) for the ZA branch [7, 12-13, 15-16] would help resolve this discrepancy, and also suggests an ideal T^1 regime between T^2 and T^0 for the ZA contribution to the specific heat [12]. However, such an approach is not pursued further

here because it requires another material-dependent parameter which is less widely available, loses some of the simplicity and physical insight of the present model, and is not necessary for good accuracy at typical temperatures (~50 K and above).

For comparison Fig. 3-8(a) also includes a traditional 3D isotropic Debye model (blue line). The isotropic sound velocity for each polarization is obtained using $v_{iso} = (v_{ab}^2 v_c)^{\frac{1}{3}}$, as required by the low temperature limit in Table 3-1. Similarly, the isotropic cutoff wavevector k_D is calculated by conserving the number of acoustic modes, $k_D = (k_{ab,m}^2 k_{c,m})^{\frac{1}{3}}$. Thus, as shown in Fig. 3-8(a) this isotropic model captures exactly the same high temperature Dulong and Petit limit and the low temperature Debye T^3 law as the anisotropic model , but at intermediate temperatures the isotropic model misses the T^2 regime and overpredicts the heat capacity by more than a factor of two.

3.3.3 Specific heat of high density polyethylene

High density polyethylene (HDPE) is chosen as a representative chain-like material because of its high anisotropy ($r \approx 0.09$) and the interest in its strongly direction-dependent and drawing-dependent thermal conductivity [32-33].

The number density of HDPE primitive unit cells (η_{puc} = 3.64×10^{28} m^{-3}) is estimated from the reported mass density [32] by approximating the primitive unit cell as containing a single [CH_2] basis. However, the acoustic parameters needed to calculate the specific heat of HDPE are not well documented in the literature. Therefore the strategy here is to fit our model to the experimental data. We treat the two Debye temperatures $\theta_{D,ab}$ and $\theta_{D,c}$ as adjustable parameters, and use a non-linear least-squares algorithm [34] to minimize the root-mean-square (RMS) error of $[(C_{expt.} - C_{model})/ C_{expt.}]$.

Figure 3-8(b) shows the experimental data and best fit model for the specific heat of HDPE of crystallinity 0.77 [32]. The experiment and model both show the expected transition from T^3 to T^1 behavior with increasing T, as expected from Table 3-1. We note that a more detailed dispersion relation accounting for subcontinuum chain bending modes [12] suggests the T^1 regime of those modes may ideally be separated into $T^{5/2}$ and $T^{1/2}$ regimes, although those do not appear separately evident in the experimental data of Fig. 3-8(b). Returning to the present model, the T^0 Dulong and Petit regime is not expected until above 1000 K, which exceeds the melting temperature of HDPE (~400 K) and thus is not accessible in the experiments. Also, because the vibrational temperature of the C-H bond can be estimated as above 1800 K [35], the heat capacity of the optical phonons is negligible over the entire experimental temperature range, and thus the calculation in Fig. 3-8(b) only accounts for the acoustic phonons. The fitting results show that the characteristic temperatures are $\theta_{D,ab} = 100$ K for the inter-chain modes and $\theta_{D,c} = 1099$ K for the intra-chain modes, corresponding to a high anisotropy r = 0.09. For comparison, Fig. 3-8(b) also shows the best fit using a traditional 3D isotropic Debye

model with one adjustable Debye temperature θ_D (289 K). The RMS residual of the anisotropic model (7%) is much better than that of the isotropic model (48%).

3.3.4 Models for TBC and transmission coefficient

To calculate the TBC using Eq. (3-19), we need the irradiation and the transmission coefficients. The former has been discussed in detail in Section 3.2.4, and for the latter we now consider two common models: a maximum transmission model (MTM) [18] and a diffuse mismatch model (DMM) [2].

The MTM (or radiation limit) supplies for the TBC an extreme upper bound compatible with the 2nd Law of Thermodynamics [18]. It assumes a 100% phonon transmission leaving the material with the lesser H_c, and the opposite transmission coefficient can be obtained directly from Eq. (3-18), leading to a TBC

$$G_{MTM} = \frac{2H_j}{H_j - H_i}\frac{\partial H_i}{\partial T},\ if\ H_i < H_j. \tag{3-26}$$

where $i, j = A, B$ or equivalently B, A.

The DMM is often used as an estimate for atomically disordered interfaces. The key assumption is that phonons lose their memory after bombarding the interface, leading to a transmission coefficient of the form[2]

$$t_{ij,DMM}(T) = \frac{H_j(T)}{H_i(T) + H_j(T)}. \tag{3-27}$$

where $i, j = A, B$ or equivalently B, A.

Substituting Eq. (3-27) into Eq. (3-19), we obtain

$$G_{DMM} = 2\frac{\frac{\partial H_A}{\partial T}H_B^2 + \frac{\partial H_B}{\partial T}H_A^2}{\left(H_A + H_B\right)^2}. \tag{3-28}$$

As noted previously, Eqs. (3-26) and (3-28) underline the symmetry of the heat transfer across the interface, i.e., there cannot be any thermal rectification upon exchanging the labels A and B.

We can now evaluate the suggestion from Section 3.2 that there may be a monotonic relationship between the irradiation and TBC. Without loss of generality, we fix H_A and increase H_B. For the DMM this does indeed always act to increase the TBC [Eqs. (3-19) and (3-27)]. However, for the MTM increasing H_B increases the TBC only while H_B is smaller than H_A; but for $H_B > H_A$ we see that increasing H_B reduces the

TBC [Eq. (3-26)]. Thus the anticipated monotonic relationship between irradiation and TBC is always true for the DMM, although only sometimes true for the MTM.

3.3.5 TBC between graphite and metals

Material	n_{puc} (10^{28}m^{-3})	v_{LA} (m/s)	v_{TA} (m/s)
Al	6.02	6240	3040
Au	5.90	3390	1290
Cr	8.33	6980	4100
Ti	2.83	6105	2923

Table 3-4. Input parameters for metals. The number density of primitive unit cells n_{puc} is obtained from Ref. 17 and the velocities from Ref. 2, with the exception of the slightly anisotropic titanium for which the effective isotropic velocities are obtained from $v_{iso} = (v_{ab}^2 v_c)^{\frac{1}{3}}$, where v_{ab} and v_c are calculated from the stiffness constants [11].

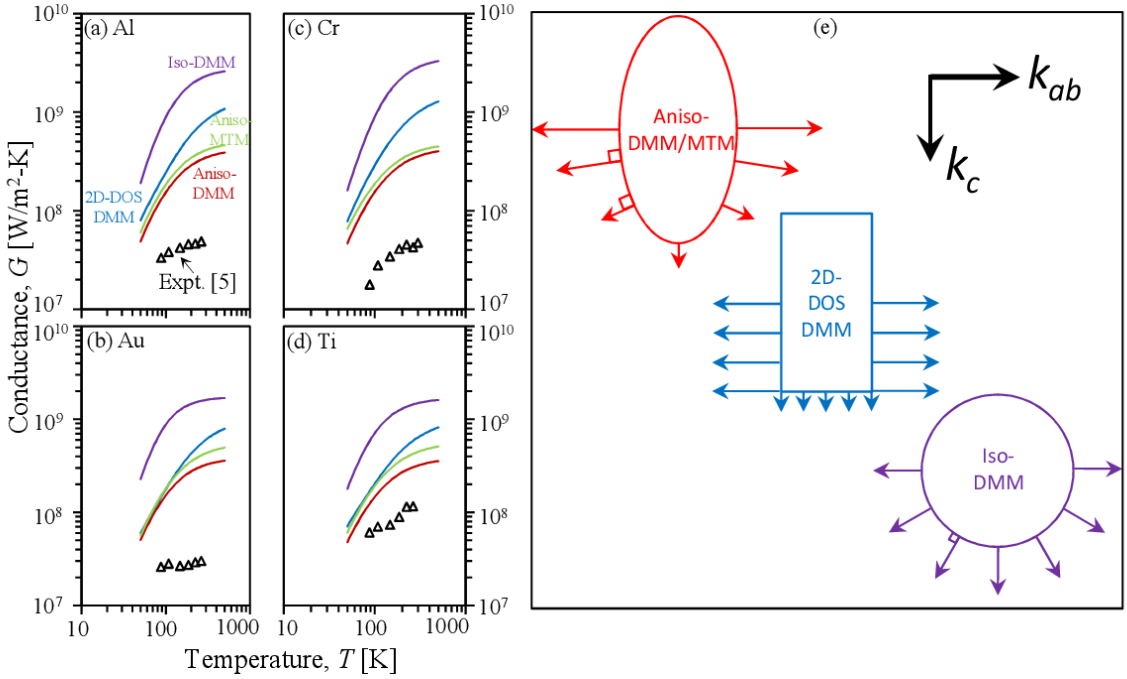

Figure 3-9. Comparison with experimental data[5] for TBC between graphite and (a) Al, (b) Au, (c) Cr, and (d) Ti. In each case, four different models are considered: the traditional isotropic DMM [2], the 2D-DOS DMM [8], and the anisotropic DMM and MTM from the present work. All models include the same pre-factor [Eq. (3-17)] and assume inelastic transmission across interfaces. The corresponding RMS errors are summarized in Table 3-5. Key qualitative differences among the models are indicated by the iso-energy surfaces and group velocity vectors sketched in (e):

as compared to the aniso-DMM, the 2D-DOS-DMM neglects the continuous transition from v_{ab} to v_c, while the iso-DMM is equivalent to decreasing v_{ab} and increasing v_c. In both cases, the additional approximations to v_{ab} and v_c tend to overestimate the *c*-axis heat transfer (Table 3-2).

We now compare the TBC model to recent measurements by Schmidt *et al.* [5] for boundaries between highly ordered pyrolytic graphite (HOPG) and various metals. In all experiments the interfaces are aligned normal to the graphite's *c*-axis, consistent with the model assumption. Using the input parameters for metals (Table 3-4) and those for graphite (Table 3-3), the flux bombarding on the interfaces (H_c) from graphite side is at most 16% of the flux from the metal sides throughout the experimental temperature range. This makes the overall TBC calculation dominated by graphite (particularly by the TL2 branch), as both Eqs. (3-26) and (3-28) simplify to $G \approx 2\left(\partial H_{c,gr} / \partial T\right)$ for $H_{c,gr} << H_{c,metal}$.

Figure 3-9 compares the experimental results [5] to four different models, including the traditional isotropic DMM [2], the 2D-DOS DMM [8], and the anisotropic DMM and MTM from this work. To facilitate meaningful comparisons, we underline two details held constant for all models. First, we include the pre-factor τ [Eq. (3-17)] which we believe represents the real physics for the equilibrium temperature drop [5, 18, 27], although it was not incorporated in the original 2D-DOS DMM [8]. This pre-factor increases the modeled TBC by a factor of 2-3 [Eq. (3-19)]. Second, we assume inelastic transmission [27] across the interfaces. Although restricting the transmission to be purely elastic would reduce the modeled TBCs closer to the experimental results, it also introduces an ambiguity in matching the phonon branches of the metals to the hybrid branches of graphite (Section 3.3.1).

The RMS errors of the four models as compared to the experimental data are summarized in Table 3-5. None of the models had any parameters adjusted to improve their fits. The comparison shows that the experiments (points in Fig. 3-9) are best explained by the anisotropic DMM of the present work (red line), with an average error of 491%. The 2D-DOS DMM[8] (blue line) is the next-best model, with an average error of 1010%, while the traditional isotropic DMM (purple line) [2] is the worst, with an average error of 3464%. Although the average error of 491% for the anisotropic DMM certainly leaves something to be desired, disagreements of this magnitude and larger are common in TBC modeling even of isotropic materials, and are most likely due to the failure of the DMM's fundamental assumptions about the interface transmissivity [1].

Comparing the models in more detail, we note that the isotropic DMM predictions greatly exceed those of the anisotropic DMM, and the experimental data. This is because the averaging rule used to obtain an effective isotropic velocity, $v_{iso} = (v_{ab}^2 v_c)^{\frac{1}{3}}$, is equivalent to increasing the incident velocity v_c and decreasing the in-plane velocity v_{ab}. As shown in Table 3-2, both of these changes tend to increase the irradiation in the *c*-axis direction, and as noted in Section 3.3.4 this will always correspond to an increase in the DMM TBC. The 2D-DOS DMM predictions exceed those of the anisotropic DMM for a similar reason, because the 2D-DOS DMM neglects the curvature of the iso-energy

surface at the edge of the FBZ, which also has the effect of overestimating the group velocity component along the *c*-axis direction and thus increasing the TBC.

The other major feature of Fig. 3-9 is the implications of the anisotropic MTM (green line), which based on the 2nd Law of Thermodynamics is expected to serve as an extreme upper bound for the TBC. The comparison with experiments shows that this anisotropic MTM indeed acts as an upper bound for these materials. However, Fig. 3-9 also shows that the isotropic DMM greatly exceeds the anisotropic MTM limit, indicating that approximating a strongly anisotropic material as isotropic can lead to TBC predictions that violate the 2nd Law of Thermodynamics.

3.4 Summary and conclusions

We have developed a general framework to calculate the TBC for anisotropic materials based on an anisotropic Debye dispersion relation and ellipsoidal first Brillouin zone, which also yields compact analytical expressions in various limiting cases. When compared to the experimental TBC between graphite and various metals from the literature [5], the new anisotropic DMM has errors at least a factor of six smaller than those of the traditional isotropic DMM and errors typically two times smaller than those of a recent 2D-DOS DMM [8]. The anisotropic model also predicts an interesting and unexpected guideline for materials engineering to increase the TBC: due to phonon focusing the TBC actually can be increased by reducing a phonon velocity, as long as it is a velocity component parallel to the plane of the interface. Recently an analogous effect on the thermal conductivity has also been reported [22-25].

3.5 Appendices

3.5.1 Evaluating the DOS and vDOS integrals

The general form of the DOS [Eq. (3-10)] is a surface integral [36] which can be evaluated by projecting the 3D iso-energy surface to a 2D plane. Here we project it to the k_a-k_b plane:

$$\iint \frac{dS_\omega}{\|\mathbf{v}_g\|} = \iint \sqrt{1+\left(\frac{\partial k_c}{\partial k_a}\right)^2+\left(\frac{\partial k_c}{\partial k_b}\right)^2}\,\frac{dk_a dk_b}{\|\mathbf{v}_g\|}, \tag{3-29}$$

where k_c can be expressed in terms of k_a and k_b: $k_c = \sqrt{\omega^2 - v_{ab}^2(k_a^2+k_b^2)}\,\big/ v_c$.

Equation (3-29) can be evaluated by implementing the polar-coordinate substitution:

$$\begin{aligned} k_a &= \rho\cos\varphi \\ k_b &= \rho\sin\varphi \end{aligned}, \tag{3-30}$$

where the domain of the polar angle is $0 \le \varphi \le 2\pi$. The main complication is in determining the domain of the polar radius ρ.

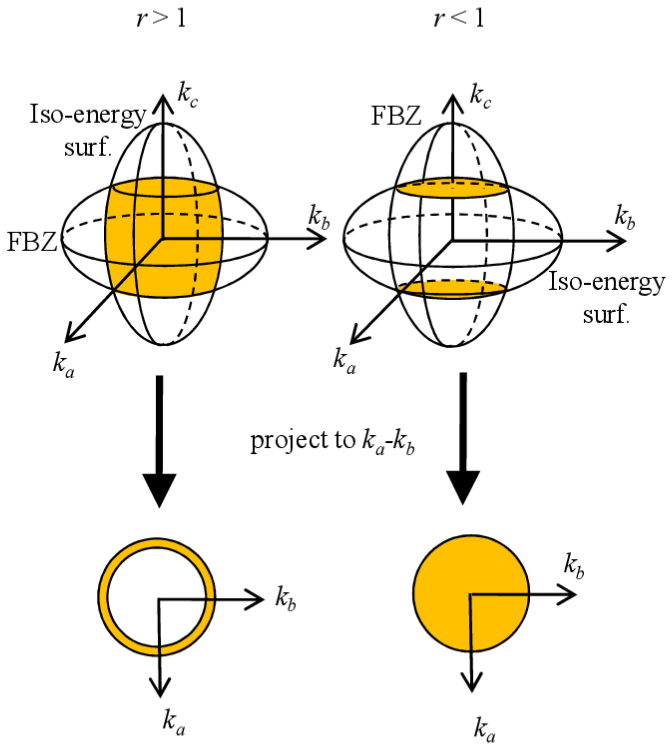

Figure 3-10. Mathematical framework to evaluate Eq. (3-10) for $\min\left(\omega_{D,c}, \omega_{D,ab}\right) < \omega < \max\left(\omega_{D,c}, \omega_{D,ab}\right)$. For materials with anisotropy ratio $r > 1$, the k_a-k_b projection of the iso-energy surface within the FBZ is an annulus. For materials with $r < 1$, the projection of the iso-energy surface becomes instead a disk.

When $\omega < \min\left(\omega_{D,c}, \omega_{D,ab}\right)$, no part of the iso-energy surface has reached the boundary of the FBZ, so $0 \le \rho \le \omega / v_{ab}$. However, when $\min\left(\omega_{D,c}, \omega_{D,ab}\right) < \omega < \max\left(\omega_{D,c}, \omega_{D,ab}\right)$, part of the iso-energy surface lies outside of the FBZ, and it is helpful to consider the domain of ρ in two categories. First, for materials with anisotropy ratio $r > 1$, the k_a-k_b projection of the iso-energy surface within the FBZ is an annulus (Fig. 3-10), with an outer radius $\rho_{\max} = \omega / v_{ab}$ and an inner radius $\rho_{\min} = k_{ab,m} \sqrt{\left(\omega^2 - \omega_{D,c}^2\right) / \left(\omega_{D,ab}^2 - \omega_{D,c}^2\right)}$ which can be obtained by solving the intersection of the two ellipsoids in Fig. 3-10. Second, for materials with $r < 1$, the projection of the iso-energy surface becomes instead a disk (Fig. 3-10), with $\rho_{\max} = k_{ab,m} \sqrt{\left(\omega_{D,c}^2 - \omega^2\right) / \left(\omega_{D,c}^2 - \omega_{D,ab}^2\right)}$, again obtained from the intersection of the two ellipsoids in Fig. 3-10.

Having identified the appropriate domain of ρ, it is straightforward to evaluate the polar-coordinate version of Eq. (3-29), and thus the DOS. For layered materials (r > 1) we find

$$D(\omega)=\begin{cases}\dfrac{\omega^2}{2\pi^2 v_{ab}^2 v_c}, & 0\le\omega\le\omega_{D,c}\\ \dfrac{\omega}{2\pi^2 v_{ab}^2 v_c}\sqrt{\dfrac{\omega_{D,c}^2(\omega_{D,ab}^2-\omega^2)}{\omega_{D,ab}^2-\omega_{D,c}^2}}, & \omega_{D,c}\le\omega\le\omega_{D,ab}\end{cases}. \tag{3-31}$$

For chain-like materials (r < 1),

$$D(\omega)=\begin{cases}\dfrac{\omega^2}{2\pi^2 v_{ab}^2 v_c}, & 0\le\omega\le\omega_{D,ab}\\ \dfrac{\omega^2}{2\pi^2 v_{ab}^2 v_c}-\dfrac{\omega}{2\pi^2 v_{ab}^2 v_c}\sqrt{\dfrac{\omega_{D,c}^2(\omega^2-\omega_{D,ab}^2)}{\omega_{D,c}^2-\omega_{D,ab}^2}}, & \omega_{D,ab}\le\omega\le\omega_{D,c}\end{cases}. \tag{3-32}$$

Following a similar procedure, we evaluate the vDOS also in two categories. For r > 1,

$$h_c(\omega)=\begin{cases}\dfrac{\omega^2}{8\pi^2 v_{ab}^2}, & 0\le\omega\le\omega_{D,c}\\ \dfrac{\omega_{D,c}^2}{8\pi^2 v_{ab}^2}\dfrac{\omega_{D,ab}^2-\omega^2}{\omega_{D,ab}^2-\omega_{D,c}^2}, & \omega_{D,c}\le\omega\le\omega_{D,ab}\end{cases}, \tag{3-33}$$

and for r < 1,

$$h_c(\omega)=\begin{cases}\dfrac{\omega^2}{8\pi^2 v_{ab}^2}, & 0\le\omega\le\omega_{D,ab}\\ \dfrac{\omega_{D,ab}^2}{8\pi^2 v_{ab}^2}\dfrac{\omega_{D,c}^2-\omega^2}{\omega_{D,c}^2-\omega_{D,ab}^2}, & \omega_{D,ab}\le\omega\le\omega_{D,c}\end{cases}. \tag{3-34}$$

3.5.2 2D and 1D phonon gas models

Here we develop simplified 2D and 1D phonon gas models to verify the various intermediate-T limiting behaviors presented above for the specific heat (Table 3-1) and c-axis irradiation (Table 3-2).

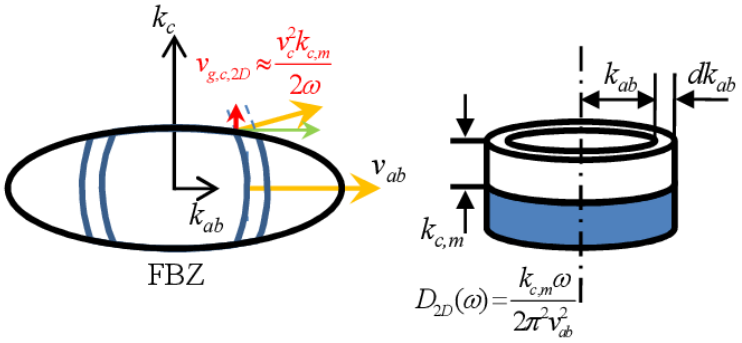

(a) 2D phonon gas

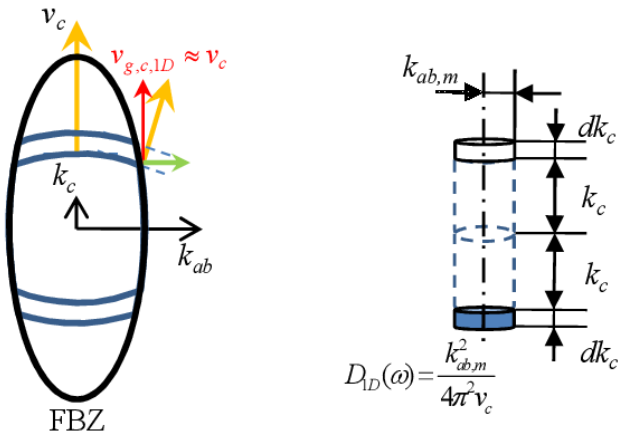

(b) 1D phonon gas

Figure 3-11. 2D and 1D phonon gas models to verify the specific heat and *c*-axis irradiation of strongly anisotropic materials at intermediate temperatures [$\min(\theta_{D,c}, \theta_{D,ab}) = T = \max(\theta_{D,c}, \theta_{D,ab})$]. The two key features are the DOS and the *c*-axis component of the group velocity.

The 2D and 1D DOS (Fig. 3-11) for a single polarization are easily shown to be:

$$\begin{aligned} D(k_{ab}) &= \tfrac{1}{2\pi^2} k_{ab} k_{c,m} \quad \text{(2D)} \\ D(k_c) &= \tfrac{1}{4\pi^2} k_{ab,m}^2 \quad \text{(1D)} \end{aligned} \quad . \tag{3-35}$$

Conservation of the number of modes requires

$$\begin{aligned} D(k_{ab}) dk_{ab} &= D(\omega) d\omega \quad \text{(2D)} \\ D(k_c) dk_c &= D(\omega) d\omega \quad \text{(1D)} \end{aligned} \quad , \tag{3-36}$$

and the group velocity components along the *ab*-plane and *c*-axis are

$$\begin{aligned} v_{g,ab} &= v_{ab}^2 k_{ab} / \omega \quad \text{(2D)} \\ v_{g,c} &= v_c^2 k_c / \omega \quad \text{(1D)}. \end{aligned} \tag{3-37}$$

Combining these we obtain the frequency-dependent DOS

$$\begin{aligned} D_{2D}(\omega) &= \frac{k_{c,m}\omega}{2\pi^2 v_{ab}^2} \\ D_{1D}(\omega) &= \frac{k_{ab,m}^2}{4\pi^2 v_c} \end{aligned} . \tag{3-38}$$

Substituting Eq. (3-38) into Eq. (3-45), we obtain the 2D and 1D specific heat:

$$\begin{aligned} C_{2D} &= \frac{3\zeta_3 k_B^3 k_{c,m}}{\pi^2 \mathrm{h}^2} \sum_{pol} \frac{T^2}{v_{ab}^2} \\ C_{1D} &= \frac{k_{ab,m}^2 k_B^2}{12 v_c \mathrm{h}} \sum_{pol} \frac{T}{v_c} \end{aligned} , \tag{3-39}$$

which agrees with the limiting behaviors in Table 3-1.

The 2D and 1D irradiation along the *c*-axis can be calculated from

$$H_c = \sum_{pol} \int_{\omega} \mathrm{h}\omega f_{BE} \tfrac{1}{2} D \, v_{g,c} d\omega. \tag{3-40}$$

The pre-factor $\frac{1}{2}$ arises because only the states with a wavevector component $k_c < 0$ are involved in this transport process. In the following discussion, we focus on the simplification of $v_{g,c}$.

For the 2D phonon gas [Fig. 3-11(a)], we have

$$\omega \simeq v_{ab} k_{ab} . \tag{3-41}$$

Combining Eqs. (3-37) and (3-41) and averaging $v_{g,c}$ over the range $[-k_{c,m}, 0]$, we find

$$v_{g,c,2D} \approx \frac{v_c^2 k_{c,m}}{2\omega} . \tag{3-42}$$

Substituting Eq. (3-42) into Eq. (3-40), we obtain the 2D irradiation along the *c*-axis

$$H_{c,2D} = \frac{k_{c,m}^2 k_B^2 T^2}{48 \mathrm{h}} \sum_{pol} \frac{v_c^2}{v_{ab}^2}, \tag{3-43}$$

which agrees with the limiting behavior in Table 3-2.

Likewise, for a 1D phonon gas [Fig. 3-11(b)], we have

$$\omega \approx v_c k_c . \tag{3-44}$$

Combining Eqs. (3-37) and (3-44), we find

$$v_{g,c,1D} \approx v_c . \tag{3-45}$$

Substituting Eq. (3-45) into Eq. (3-40), we obtain the 1D irradiation along the *c*-axis

$$H_{c,1D} = \frac{k_{ab,m}^2 k_B^2 T^2}{16\hbar}, \tag{3-46}$$

which again agrees with the limiting behavior in Table 3-2.

3.5.3 Defining an equilibrium temperature

As mentioned in Ref. 18, there are several ways to define an equilibrium temperature $T_{eq.}$ in terms of the opposing emitted temperatures T_+ and T_- used in a two-flux model. The typical strategy is to require conservation of some related quantity such as phonon number density, energy density, or irradiation along the *c*-axis. Here we show that the difference between any of these definitions and a naive definition

$$T_{eq.,naive} = \tfrac{1}{2}(T_+ + T_-) \tag{3-47}$$

is of the order of Δ^2/T_-, where $\Delta = T_+ - T_-$, and thus for low-to-moderate-thermal bias all definitions are practically equivalent.

Here we take the conservation of irradiation along the *c*-axis as an example:

$$H_c\left(T_{eq.}\right) = \tfrac{1}{2} H_c\left(T_+\right) + \tfrac{1}{2} H_c\left(T_-\right). \tag{3-48}$$

In the analytical limiting cases in Table 3-2, we have

$$H_c\left(T\right) = AT^n. \tag{3-49}$$

where A is a function of the velocities and wavevector cutoffs, but not temperature. For intermediate cases not covered by Table 3-2, the numerical results of Fig. 3-6 confirm that H_c is a smoothly-varying function of T, which for small Δ around any T is still well-approximated by the power law form of Eq. (3-49). Therefore n is in the range [1, 4], though not necessarily an integer.

Substituting Eq. (3-49) into Eq. (3-48), the equilibrium temperature can be generalized as

$$T_{eq.}^n = \tfrac{1}{2} T_+^n + \tfrac{1}{2} T_-^n . \tag{3-50}$$

Using a Taylor series Eq. (3-50) can be expanded as

$$T_{eq.} = T_{-}\left[1+\frac{\Delta}{2T_{-}}+\frac{n-1}{8}\left(\frac{\Delta}{T_{-}}\right)^{2}+O\left(\frac{\Delta}{T_{-}}\right)^{3}\right]. \tag{3-51}$$

where O represents higher order terms.

The naive arithmetic average equilibrium temperature can be expressed as

$$T_{eq.,naive} = T_{-}\left(1+\frac{\Delta}{2T_{-}}\right). \tag{3-52}$$

Subtracting Eq. (3-52) from Eq. (3-51) and neglecting higher order terms, we obtain

$$\frac{T_{eq.}-T_{eq.,naive}}{T_{eq.}} \approx \frac{\frac{n-1}{8}\left(\frac{\Delta}{T_{-}}\right)^{2}}{1+\frac{\Delta}{2T_{-}}+\frac{n-1}{8}\left(\frac{\Delta}{T_{-}}\right)^{2}}. \tag{3-53}$$

Considering that $\Delta/T_{-} = 1$, Eqs. (3-51) and (3-53) indicate that $\left(T_{eq.}-T_{eq.,naive}\right)/T_{eq.} = \Delta/T_{eq.}$, and thus the naive definition is adequate to represent the real equilibrium temperature.

Following a similar procedure, we have confirmed that the conclusion above also applies to approaches using conservation of phonon number density and energy density.

3.5.4 Comparing to the phonon irradiation calculation using full-direction-dispersion

As discussed in Section 3.3.5, we believe the discrepancies between the anisotropic DMM model and the experimental TBC seen in Fig. 3-9 are largely due to the crude approximations for the transmission coefficients, not the anisotropic Debye approximation used for the phonon irradiation. To independently check the H_c calculation, here we validate the anisotropic Debye model by comparison with the phonon irradiation of a graphite-like material calculated using the lattice dynamics method [22, 37]. We followed Ref. 22 in detail, including using the optimized Tersoff potential [38] for intra-plane interactions and the Lennard-Jones (LJ) potential [39] for inter-plane interactions. With the resulting all-direction dispersion relation, we calculated the phonon irradiation by modifying Eq. (2) in Ref. 22 from classical to Bose-Einstein statistics.

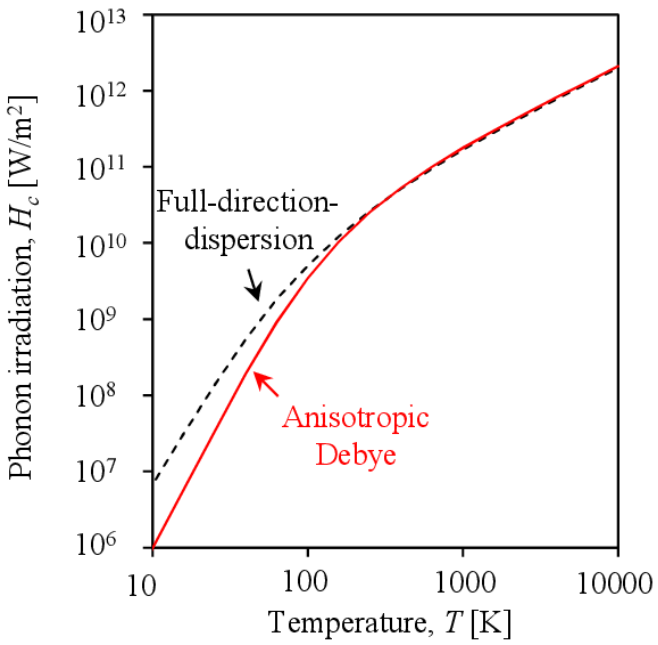

Figure 3-12. Comparison with lattice dynamics calculation (all-direction-dispersion) for phonon irradiation of a graphite-like material, showing errors less than 10% from 200 K – 10000 K. The disagreement at lower temperature is due to the failure to capture the reduced group velocity of ZA phonons at long wavelengths [12]. The Debye model parameters for this graphite-like material are fully determined from the dispersion calculated from the lattice dynamics method [22] without any fitting.

Figure 3-12 shows the comparison between the phonon irradiation calculated using the lattice dynamics dispersion and that calculated using our model with velocities ($v_{ab,TA}$ = 10,100, $v_{ab,TL1}$ = 25,000, $v_{ab,TL2}$ = 5,700; $v_{c,TA}$ = 300, $v_{c,TL1}$ = 300, $v_{c,TL2}$ = 2,500 [m/s]) extracted from the lattice dynamics dispersion along [100] and [001]. The simple Debye ellipsoid results agree with the full lattice dynamics calculation to within ±10% over a wide temperature range from 200 K to 10,000 K. Below 100 K, the Debye ellipsoid approximation deviates from the lattice dynamics results due to the shortcoming described in Section 3.2.1: for the ZA branch, the Debye model cannot capture the dependence of phase velocity on the magnitude of the wavevector.

3.6 References

[1] D. G. Cahill, W. K. Ford, K. E. Goodson, G. D. Mahan, A. Majumdar, H. J. Maris, R.Merlin, and S. R. Phillpot, J. Appl. Phys. **93**, 793 (2003).

[2] E. T. Swartz and R. O. Pohl, Rev. Mod. Phys. **61**, 605 (1989).

[3] W. DeSorbo and W. W. Tyler, J. Chem. Phys. **21**, 1660 (1953).

[4] U. Bergenlid, R. W. Hill, F. J. Webb, and J. Wilks, Philos. Mag. **45**, 851 (1954).

[5] A. J. Schmidt, K. C. Collins, A. J. Minnich, and G. Chen, J. Appl. Phys. **107**, 104907 (2010).

[6] R. Prasher, Phys. Rev. B **77**, 075424 (2008).

[7] K. Komatsu, J. Phys. Soc. Jpn. **10**, 346 (1955).

[8] J. C. Duda, J. L. Smoyer, P. M. Norris, and P. E. Hopkins, Appl. Phys. Lett. **95**, 031912 (2009).

[9] J. C. Bowman and J. A. Krumhansl, J. Phys. Chem. Solids **6**, 367 (1958).

[10] K. Kopinga, P. van der Leeden, and W. J. M. de Jonge, Phys. Rev. B **14**, 1519 (1976).

[11] B. A. Auld, *Acoustic Fields and Waves in Solids* (Wiley, New York, 1973).

[12] L. D. Landau and E. M. Lifshitz, *Statistical Physics* (Pergamon, New York, 1980).

[13] R. Nicklow, N. Wakabayashi, and H. G. Smith, Phys. Rev. B **5**, 4951 (1972).

[14] R. Saito, A. Jorio, A. G. Souza Filho, G. Dresselhaus, M. S. Dresselhaus, and M. A. Pimenta, Phys. Rev. Lett. **88**, 027401 (2001).

[15] G. Savini, Y. J. Dappe, S. Öberg, J. C. Charlier, M. I. Katsnelson, and A. Fasolino, Carbon **49**, 62 (2011).

[16] L. Wirtz and A. Rubio, Solid State Commun. **131**, 141 (2004).

[17] C. Kittel, *Introduction to Solid State Physics* (John Wiley & Sons, New York, 1996).

[18] C. Dames and G. Chen, Journal of Applied Physics **95**, 682 (2004).

[19] T. Klitsner, J. E. VanCleve, H. E. Fischer, and R. O. Pohl, Physical Review B **38**, 7576 (1988).

[20] J. P. Wolfe, *Imaging Phonons: Acoustic Wave Propagation in Solids* (Cambridge University Press, New York, 1998).

[21] N. Zuckerman and J. R. Lukes, J. Heat Transfer **130**, 082402 (2008).

[22] Z. Wei, Y. Chen, and C. Dames, Appl. Phys. Lett. **102**, 011901 (2013).

[23] P. K. L. Hu, S. Shenogin, and D. Cahill (unpublished); cited in Refs. 24 and 25.

[24] C. Chiritescu, D. G. Cahill, C. Heideman, Q. Lin, C. Mortensen, N. T. Nguyen, D. Johnson, R. Rostek, and H. Bottner, J. Appl. Phys. **104**, 033533 (2008).

[25] W.-P. Hsieh, B. Chen, J. Li, P. Keblinski, and D. G. Cahill, Phys. Rev. B **80**, 180302 (2009).

[26] M. F. Modest, *Radiative Heat Transfer* (McGraw-Hill, New York, 1993).

[27] G. Chen, Phys. Rev. B **57**, 14958 (1998).

[28]G. Chen, *Nanoscale Energy Transport and Conversion* (Oxford University Press, New York, 2005).

[29] T. Beechem and P. E. Hopkins, J. Appl. Phys. **106**, 124301 (2009).

[30] J. Krumhansl and H. Brooks, J. Chem. Phys. **21**, 1663 (1953).

[31] F. P. Incropera, D. P. DeWitt, T. L. Bergman, and A. S. Lavine, *Introduction to Heat Transfer* (John Wiley & Sons, New York, 2007).

[32] D. B. Mergenthaler and M. Pietralla, Z. Phys. B **94**, 461 (1994).

[33] S. Shen, A. Henry, J. Tong, R. Zheng, and G. Chen, Nat Nano **5**, 251 (2010).

[34] S. C. Chapra, *Applied Numeical Methods with Matlab* (McGraw-Hill, New York, 2008).

[35] V. P. Carey, *Statistical Thermodynamics and Microscale Thermophysics* (Cambridge University Press, New York, 1999).

[36] M. D. Greenberg, *Advanced Engineering Mathematics* (Prentice Hall, New Jersey, 1998).

[37] M. T. Dove, *Introduction to Lattice Dynamics* (Cambridge University Press, Cambridge, 1993).

[38] L. Lindsay and D. A. Broido, Phys. Rev. B **81**, 205441 (2010).

[39] L. A. Girifalco, M. Hodak, and R. S. Lee, Phys. Rev. B **62**, 13104 (2000).

Chapter 4: A photon thermal diode

4.1 Introduction

Energy is one of the dominant global issues of modern times, and the majority of it passes through the thermal domain [1]. Traditional thermal engineering is based on the paradigm of linear thermal elements, such as thermal resistors (R) and capacitors (C), and in this sense lags many decades behind electrical engineering, which has benefited greatly from ingenious applications of nonlinear elements. The most fundamental such element would be a thermal rectifier. Here we define the thermal rectification as [2]

$$\gamma\left(T_H, T_C\right) = \left(Q_{Fwd} - Q_{Rev}\right) \Big/ Q_{Rev} , \tag{4-1}$$

where Q_{Fwd} and Q_{Rev} are the heat transfers under the same thermal bias $\Delta T = T_H - T_C$ but different directions: Forward (Fwd) and Reverse (Rev).

Regardless of the type of energy carrier, all thermal rectifiers require two key ingredients (Fig. 4-1): asymmetry and nonlinearity [3]. Classical thermal diodes include natural convection in a gravitational field (molecular gases) and a Fourier Law mechanism exploiting temperature-dependent thermal conductivities (electrons, phonons) [3-4]. Within radiation heat transfer (photons), to our knowledge rectification has not been experimentally established by any mechanism, classical or otherwise, although recent theoretical work has suggested far-field [5] and near-field [6-7] mechanisms exploiting temperature-dependent total emissivity, $\varepsilon(T)$.

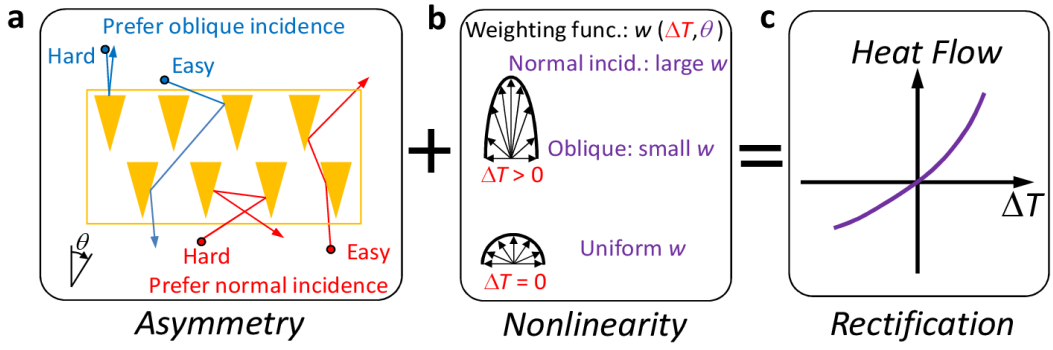

Figure 4-1. The two key ingredients of a photon thermal diode: asymmetry and nonlinearity. (a) Asymmetry arises from angle-dependent transmission through the test section containing pyramidal reflectors: from bottom to top, transmission is higher for energy carriers with normal incidence, while from top to bottom, transmission is favored for carriers of oblique incidence. (b) The nonlinearity arises because the emission from the hot reservoir (not shown) has an angular weighting that is also bias-dependent. At zero thermal bias ($\Delta T = 0$), the angular weighting is nearly uniform (*i.e.* Lambertian), while for non-zero thermal bias ($\Delta T > 0$), the emission becomes increasingly forward-peaked. (c) The combined effect is thermal rectification.

Here we present a new mechanism of photon thermal rectification, inspired by a pioneering ballistic electrical diode [8] and previous proposals for phonon heat transfer [9-13]. Figure 4-1 shows the basic concept. Due to the taper of the pyramidal mirrors, photons of near-normal incidence ($\theta \approx 0°$) have higher transmission for trajectories from bottom-to-top than from top-to-bottom. However, the trend is opposite for trajectories entering the test section at highly oblique incidence (θ approaching 90°). At equilibrium these effects must exactly cancel, a fundamental requirement of the 2nd Law of Thermodynamics (equivalently, conservation of optical etendue [14]). As recently noted by ourselves [11] and others [12] this further implies that the asymmetric structure of Fig. 4-1(a) alone [9-10] cannot show rectification even far away from equilibrium. A nonlinearity is also mandatory [3, 11-12], which we achieve through a "thermal collimator" whose angle-dependent emission distorts as a function of the net thermal flux. Here we experimentally demonstrate both the rectification effect and the necessity of the collimator.

4.2 Experimental design

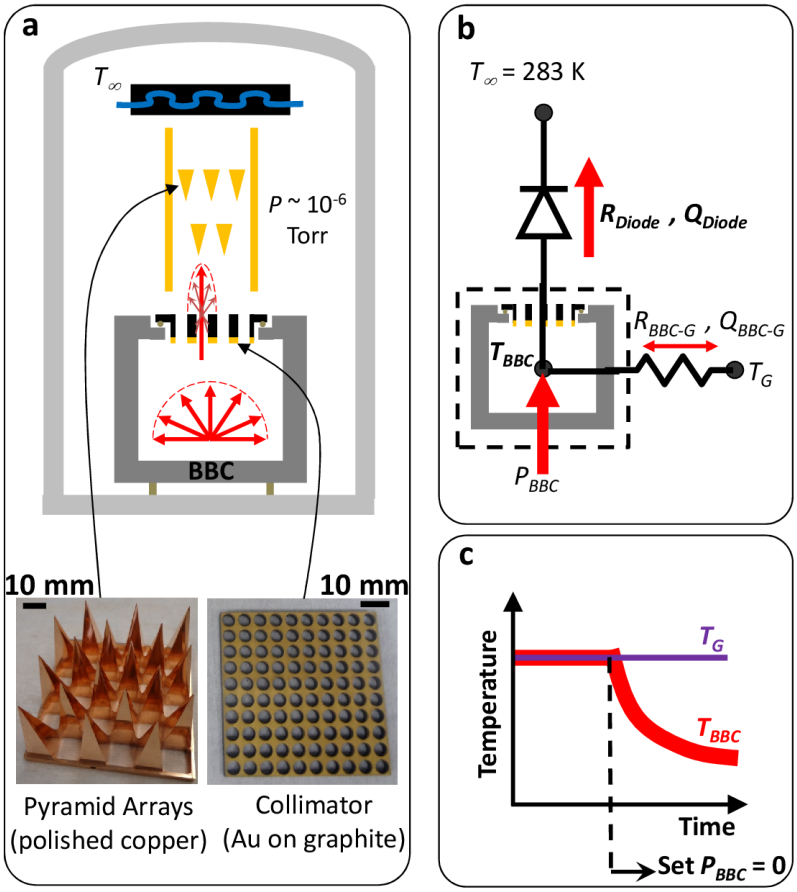

Figure 4-2. Experimental concept. (a) A hot blackbody cavity (BBC; its guard heater and shields omitted for clarity) generates photons with a Lambertian distribution. The key diode components are the thermal collimator and the test

section with pyramidal mirrors. The depicted configuration is forward bias (Fwd), with reverse bias (Rev) obtained by flipping the test section. (b) Energy balance applied to the BBC (dashed line): changes in stored thermal energy are balanced by the electrical heater (P_{BBC}) and heat transfers through the diode (Q_{Diode}) and to/from the guard (Q_{BBC-G}). (c) Lumped cooling scheme: after stabilizing the BBC and guard at $T_{BBC} = T_G = 573$ K, the BBC power is shut down while T_G held constant. Q_{Diode} is extracted from the resulting BBC cooling curve.

Figure 4-2(a) shows our experimental concept. Photons are emitted from a graphite blackbody cavity (BBC) at $T_{BBC} = 573$ K, which offers a well defined boundary condition with a nearly Lambertian emission (for design details see Appendices). The cold side of the radiation field is maintained at $T_\infty = 283$ K using a water-cooled black plate. For asymmetric scatterers we use highly-polished copper pyramids, chosen for their high infrared (IR) reflectivity. As in Fig. 4-1(a), photons incident towards the pyramids' peaks have higher transmission for normal incidence, while photons incident towards their bases have higher transmission for oblique incidence (see Figs. 4-5 and 4-6 in Appendices for further verification).

The second key ingredient is the thermal collimator, which provides bias-dependent angular weighting of emission as depicted in Fig. 4-1(b) and Fig. 4-2(a). To create a suitable nonlinearity, we designed a collimator from a perforated graphite plate coated with gold film as an IR reflector on the side facing the BBC [Fig. 4-2(a)]. The collimator is mounted to the BBC using weak thermal links. These features ensure that, whenever the diode experiences substantial thermal bias, the temperature of the collimator is significantly lower than that of the BBC (for example, $T_{col} \sim 473$ K when $T_{BBC} = 573$ K and $T_\infty = 283$ K). Then, due to the open holes in the collimator, for angles close to $\theta \approx 0°$ many of the photons entering the pyramid test section were emitted from the BBC core at T_{BBC}. However, photons entering at oblique angles are much more likely to have been emitted from the internal cylindrical surfaces of the collimator holes, with lower intensity since $T_{col} < T_{BBC}$. The greater the thermal bias, the larger the difference between T_{col} and T_{BBC}, and thus the greater the angular distortion of the intensity incident on the pyramids (see also Fig. 4-7 in Appendices). The configuration shown in Fig. 4-2(a) is Fwd biased: when the BBC is hot, photons emitted normally have more intensity, and are relatively *easy* to transmit through the pyramidal test section. Similarly, flipping the test section upside down creates Rev bias: the collimator emission is still weighted towards normal incidence, but this is now relatively *difficult* to transmit through the test section. The result is thermal rectification.

The experimental design ensures that convection and conduction losses from the BBC are below 0.1% (see Appendices). To minimize radiation heat losses from the BBC exterior (< 1%), we surround it with 5 concentric radiation shields and an active guard heater (see Appendices). A kinematic coupling between test section and BBC is used to ensure positioning accuracy and repeatability when flipping the test section between polarities. The BBC and its guard each have two independent heater loops [Fig. 4-4(b) in Appendices]. Each is typically stable to within ±0.5 K, with maximum differences of 1.5 K among these four heater zones as measured by six thermocouples.

This experiment requires highly accurate measurements of the heat transfer through the test section, Q_{diode}, under Fwd and Rev biases. Direct evaluation of the steady-state BBC power from the heaters' current I and voltage V was found to be impractical due to the highly oscillatory nature of PWM-switched AC electricity. Instead we implemented the lumped cooling method [15] depicted in Figs. 4-2(b) and (c). First the BBC and guard are both stabilized at 573 K. Then for times $t > 0$, the BBC heaters are turned off ($P_{BBC} = 0$) while the guard is maintained at its original temperature. From the time-dependent cooling curve [Fig. 4-2(c)] we extract Q_{diode} as follows. The excellent shielding between BBC and guard ensures $Q_{BBC-G} << Q_{diode}$. This approaches the perfect shield limit (see Appendices), whereby the BBC energy balance of Fig. 4-2(b) simplifies to

$$C_{BBC}\frac{dT_{BBC}}{dt} = -Q_{diode}, \tag{4-2}$$

where C_{BBC} is the thermal capacitance of the BBC (with SI units J/K). In our experimental regime the perfect-shield approximation of Eq. (4-2) agrees with exact numerical solutions to within 0.1% (see Appendices), and also brings several experimental advantages. Most importantly, the cooling curve becomes independent of T_G and R_{BBC-G}, so the final results are insensitive to drifts or fluctuations in these quantities. Also, Q_{diode} comes directly from the cooling rate, $|dT_{BBC}/dt|$, which is measured with much better accuracy than the electrical power $P_{BBC} = [I \cdot V]_{BBC}$. Furthermore, although quantifying Q_{diode} requires an estimate for C_{BBC} based the BBC's geometry and specific heat capacity [16], C_{BBC} is a common parameter for both Fwd and Rev bias, and thus cancels out in Eq. (4-1). Thus, rectification is calculated directly from the cooling curves using

$$\gamma = \left(\left|\frac{dT_{BBC}}{dt}\right|_{Fwd} - \left|\frac{dT_{BBC}}{dt}\right|_{Rev} \right) \Bigg/ \left|\frac{dT_{BBC}}{dt}\right|_{Rev}, \tag{4-3}$$

where both derivatives are evaluated over the same temperature range.

4.3 Results

We performed two sets of experiments to verify the key predictions [11-12] that both asymmetry and nonlinearity are required. First we confirm that asymmetry alone is insufficient by measuring the pyramidal test section without the collimator. The open points in Fig. 4-3(a) show two such control experiments. The BBC heater is turned off at 573 K, and we allow a 4 K buffer before defining $t = 0$ to ensure the system has fully transitioned to its free-cooling trajectory. To better detect any differences between the curves, in Fig. 4-3(b) we plot the cooling rate, $|dT_{BBC}/dt|$, evaluated numerically over a 10 point (10 minute) moving average. Both panels confirm that these two control experiments are virtually indistinguishable from each other. To describe each trial with a single number, we average the cooling rate from 569 K to 553 K and calculate the corresponding heat flow through the diode using Eq. (4-2). The results for three trials each of Fwd and Rev bias are plotted in Fig. 4-3(c) using the unfilled columns. The

difference (0.3%) between the average Q_{diode} under Fwd and Rev biases for these control experiments is well within experimental uncertainty (Fwd and Rev standard deviations each < 0.8%), making this the first experimental confirmation that ballistic thermal rectification is not possible through asymmetric scattering alone.

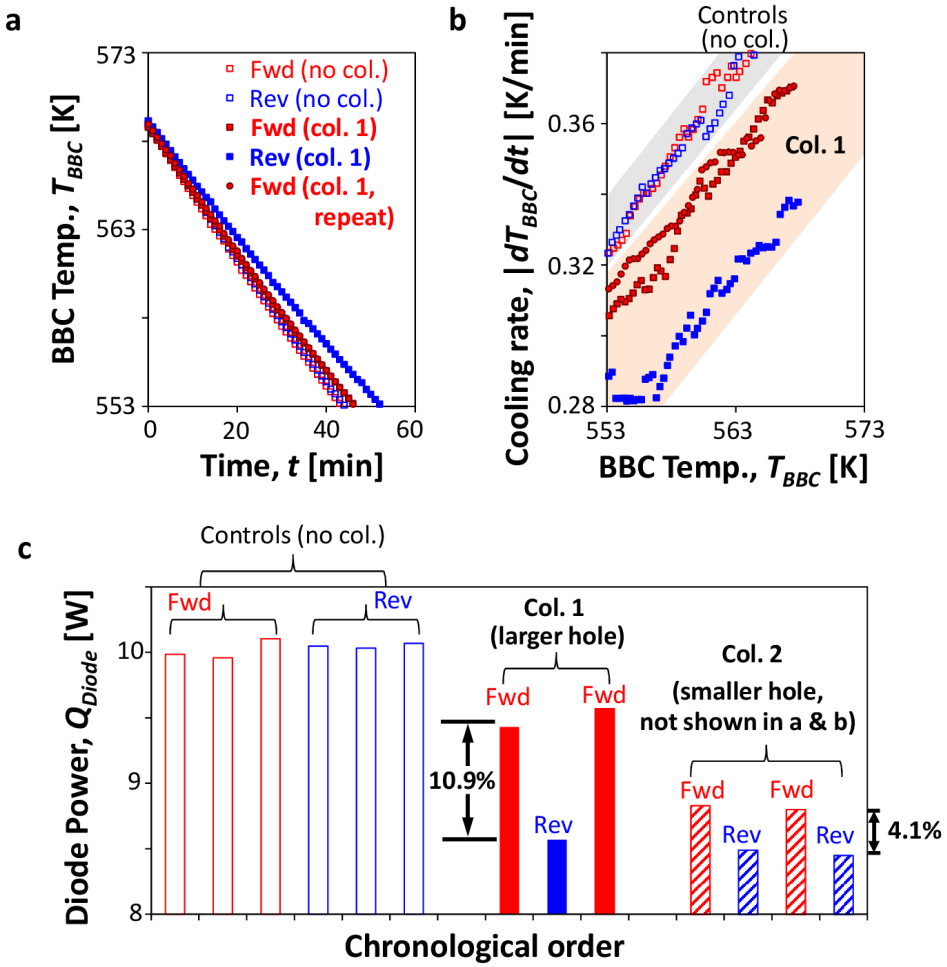

Figure 4-3. (a) Cooling curves for representative experiments without (open points: controls) and with (filled points) the thermal collimator. (b) Cooling rates calculated from a using a 10-point moving average. Symbols as in (a). The two control experiments (shaded in gray) are virtually indistinguishable from each other, while the three experiments with the collimator (shaded in orange) are clearly separated. (c) Diode heat transfers calculated from Eq. (4-2) by averaging the cooling rate in b from 569 K to 553 K, and including additional trials. These key results demonstrate how thermal rectification requires both asymmetry and nonlinearity. Another collimator (Col. 2: striped bars) with narrower holes shows similar results, but degrades the rectification to around 4.1% (Col. 2 data omitted from (a) and (b) for clarity).

Finally, we measure the complete device with pyramidal test section and thermal collimator. Using a collimator optimized by a semi-quantitative guideline (see Appendices), Figs. 4-3(a) and (b) show that the Fwd bias configuration (red filled squares)

now clearly cools faster than the Rev bias case (blue filled squares). For example, at a BBC temperature of 563 K, Fig. 4-3(b) shows that the BBC cooled at 0.352 K/min in Fwd bias, but 0.314 K/min in Rev bias. Repeatability was confirmed after the Rev bias test by flipping the test section again and re-measuring Fwd bias, with very good consistency (red filled circles). Thus, as summarized in Fig. 4-3(c) using the filled columns, this first experimental proof of ballistic thermal rectification showed a rectification γ = 10.9%. To further verify the rectification effect, the experiment was repeated using a collimator with holes of half the diameter but the same thickness and open-area fraction. As shown by the striped columns in Fig. 4-3(c), the resulting heat transfer was again asymmetric and highly repeatable, and as expected (see Appendices) the rectification was reduced (γ = 4.1%).

4.4 Outlook

The results in Fig. 4-3 represent the first experimental demonstration of a photon thermal diode using any mechanism. This is also the first demonstration of the ballistic thermal rectification mechanism [9-12] for any carrier type, and in principle is generalizable to other ballistic carriers including electrons and phonons, for example using pyramidal quantum dots [17], sawtooth nanowires [9-10, 18], or microfabricated structures (see Appendices).

Highly-effective thermal rectifiers could find numerous applications in thermal engineering. Many arise from electrical analogues [19]. For example, in solar-thermal power, a temperature doubler (analogous to a voltage doubler) can exploit nighttime cold temperatures as well as daytime highs to increase the average temperature difference driving a heat engine, increasing both efficiency and power output [11, 20]. A thermal diode's clamping functionality could be used for thermal regulation of building envelopes [21], as well as thermal protection of delicate components as in electrical hardware, spacecraft thermal shielding, and satellite radiators. Thermal diodes are also a fundamental element for logic operations; besides the suggestion of thermal information processing [22] this can also benefit power generation, since an array of diodes can automatically pick out only the hottest of sources and coldest of sinks.

4.5 Appendices

4.5.1 Design of the blackbody cavity (BBC)

Although for simplicity the main text is written as if both reservoirs are perfectly black, all of the fundamental analysis of the ballistic thermal rectification mechanism applies just as well to reservoirs with arbitrary spectral, directional, emissivity functions $\varepsilon(\lambda,\theta,\varphi,x,y)$. Importantly, the analysis predicts that even for an arbitrary asymmetric test section and both reservoirs with their own arbitrary $\varepsilon(\lambda,\theta,\varphi,x,y)$, rectification cannot occur without the introduction of some explicit nonlinearity [11] (here, the thermal collimator). For simplicity in the discussion and interpretation of the experiments, we endeavored to use reservoirs that are approximately black, i.e. $\varepsilon \approx 1$ for all λ, θ, φ, x, and

y across the aperture. Here we followed standard BBC designs to approach this ideal [23]. Graphite was chosen as the BBC material because of its relative high intrinsic emissivity (ε = 0.80 at room temperature, increasing with temperature in the experimental regime [24]), good high temperature stability, and machinability by the supplier (Poco Graphite). The total directional emissivity [$\varepsilon(\theta, \varphi)$] of our resulting design is at least 0.91 from all (x,y) across the aperture [23].

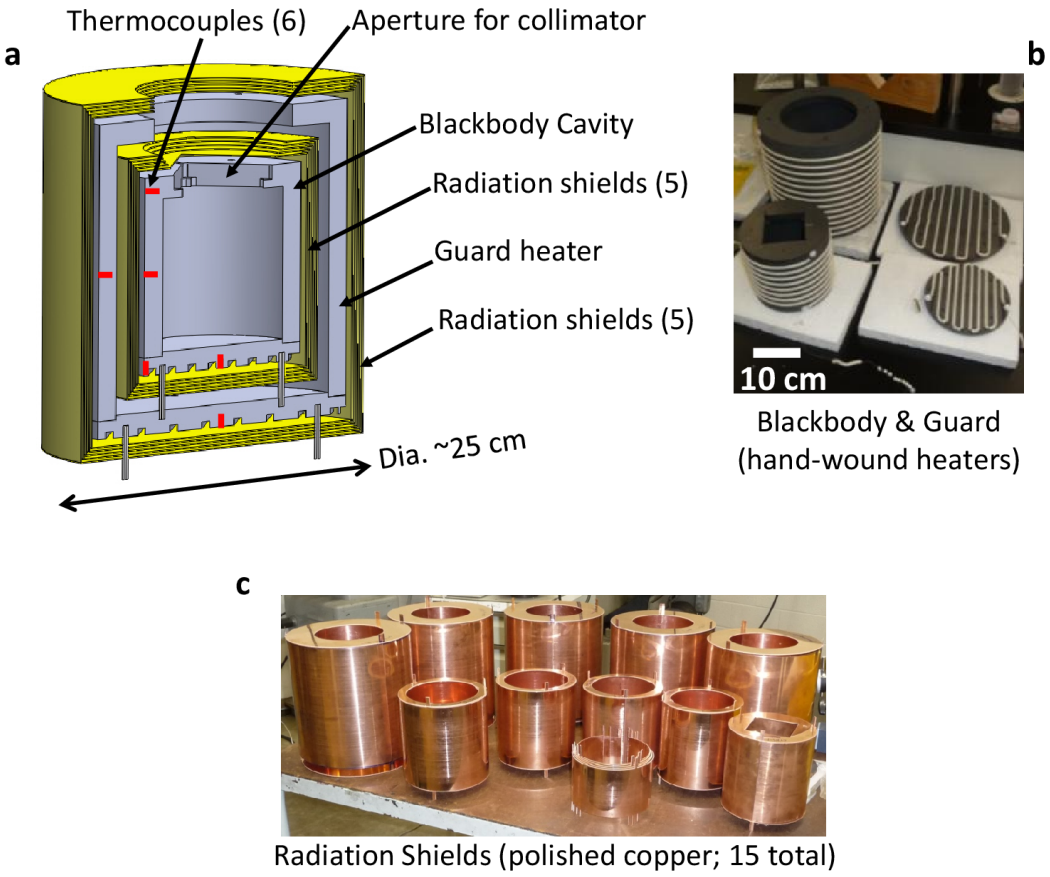

Figure 4-4. Design of Blackbody Cavity (BBC). (a) Guarding + shielding concept (CAD drawing) ensures 99% of the BBC's heater power transmits through the aperture instead of leaking out through the BBC side walls or supports. (b) Home-built BBC and guard with hand-wound heaters ensure good temperature stability and uniformity ($T_{max} - T_{min} < 1.5$ K, as measured by six K-type thermocouples as shown in a). (c) 15 radiation shields made of polished copper: five concentric "cans" for the BBC (middle row), five for the guard (back row), and five for the pyramidal test section (front row, assembled).

One major design criteria for heat transfer is to ensure the large majority of the BBC's heater power transmits through the BBC aperture (and thus the test section) instead of being lost from the exterior of the BBC's side walls. This is difficult because the transmit-to-loss ratio scales with the area ratio of the aperture to the external BBC surfaces, and thus clashes with the design criteria for a high effective emissivity of the

aperture [23]. In other words, a larger aperture increases the transmit-to-loss ratio, but decreases the effective emissivity of the aperture. To overcome this difficulty, a guarding + shielding concept [Fig. 4-4(a)] is implemented. A guard heater (graphite) is designed to create a local surrounding temperature approximately equal (±1 K) to the temperature of the BBC, thus greatly reducing the radiation loss from the BBC. The BBC and guard each have two independent heater loops [Fig. 4-4(b)], made by hand winding heater wires of nickel-chromium alloy (Omega Engineering, NIC80-010-062 and NI80-040; insulated with steatite "fish spine" beads, FS-200-14, $k \approx 5$ W/m-K), and anchored with cement (Resbond-920, $k \approx 2.2$ W/m-K) along 15% of their length. We press fit six K-type thermocouples into the graphite [Fig. 4-4 (a)]: one at the center of each heater zone [Fig. 4-4 (b)] to provide feedback to the PWM controllers; plus one at the edge of each BBC zone to check the temperature uniformity of the BBC. The worst case non-uniformity is found to be 1.5 K from the center to the edge of the BBC side wall.

Five concentric radiation shields [Fig. 4-4 (c); polished copper, $\varepsilon < 0.05$ [16]] are placed between the guard heater and BBC (top, sides, and bottom), with another five radiation shields placed outside the pyramidal test section to further reduce the radiation loss. Five more concentric radiation shields are placed outside the guard heater (top, sides, and bottom) to further reduce the power requirements of the guard heater. With this design, at steady state the heat loss through the BBC side walls is estimated to be < 1% of the heating power $P_{BBC} = [I \cdot V]_{\mathrm{BBC}}$. Finally, to minimize conductive losses we use four hollow ceramic pegs to support the BBC above the guard heater, and another four pegs to support the whole system above the vacuum chamber floor. Each peg has length 1.50", wall thickness 0.039", and outer diameter 0.156"; to accommodate the thermal expansion mismatch between graphite and copper the through-holes on the radiation shields have diameters 0.190". The resulting heat conduction through the ceramic pegs is estimated to be < 0.1% of the power transmitting through the test section.

4.5.2 Asymmetric transmission functions

The starting point of this ballistic thermal rectification mechanism is based on the intuition depicted in Fig. 4-1(a) of the main text: the ballistic trajectories directed towards the peaks of the pyramidal arrays (τ_{12}; here 1 denotes the test section terminal facing the peaks of the pyramids, and 2 denotes that facing the bases) have high transmission for normal incidence, while the ballistic trajectories incident on the bases of the pyramidal arrays (τ_{21}) have high transmission for oblique incidence.

One fundamental question may arise regarding this intuition: is it possible to achieve $\tau_{12} = 100\%$ while $\tau_{21} = 0\%$ for all incident positions and angles? The answer is no. A qualitative argument is based on time reversal symmetry: for each transmitted trial along one direction, there must exist a corresponding trial which follows exactly the same path but in the opposite direction. It's impossible to block one trial without blocking the other. This insight has been quantified using a Landauer-Büttiker approach [11-12]. At thermal equilibrium, for photons emitted with Lambertian distributions from parallel thermal reservoirs with same contact areas (x-y plane), from the 2nd Law of

Thermodynamics it can be shown [11] that for any possible asymmetric test section geometry it must always be the case that

$$\int_0^{\frac{\pi}{2}} \tau_{12}^{\theta} \sin\theta\cos\theta \;\; d\theta = \int_0^{\frac{\pi}{2}} \tau_{21}^{\theta} \sin\theta\cos\theta \;\; d\theta, \tag{4-4}$$

where τ_{12}^{θ} and τ_{21}^{θ} are the transmission coefficients after averaging over the contact area and azimuthal angles φ, thus depending only on the polar angle θ. Thus, the two transmission functions, τ_{12}^{θ} and τ_{21}^{θ}, are not independent but rather are constrained by the 2nd Law of Thermodynamics. Interestingly this constraint is equivalent to the conservation of etendue in optical terminology [14], which also is essentially the reciprocity relation of view factor analysis[25] in radiation heat transfer.

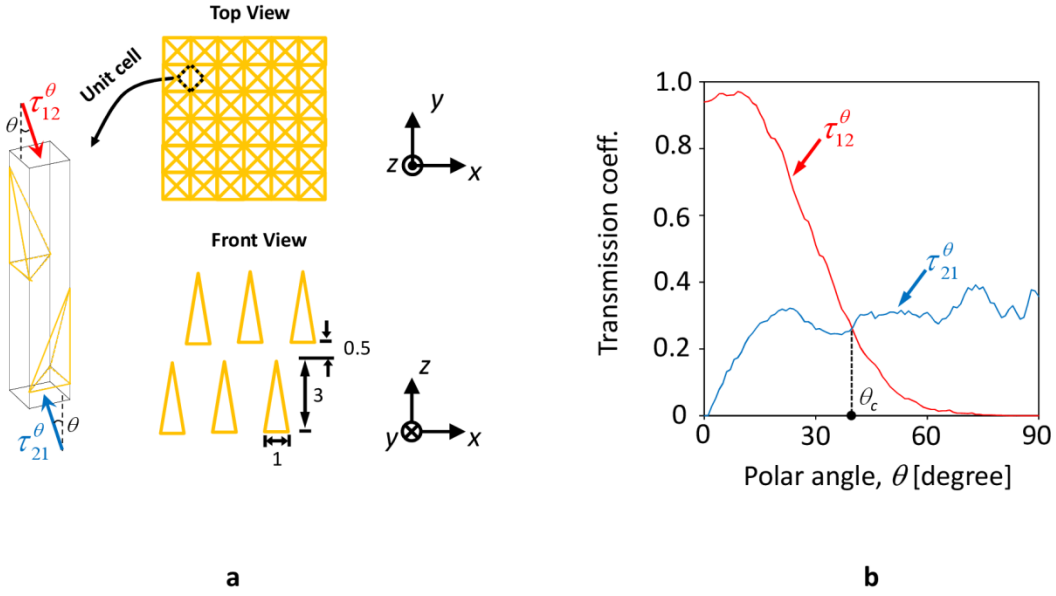

Figure 4-5. Ray tracing simulation to optimize the transmission function. (a) Simulation domain: staggered double-layer pyramidal arrays (each layer a checkerboard) with specular surfaces and high aspect ratio for each pyramid. Mirror symmetries are applied to reduce the simulation domain to the unit cell indicated by the black dashed square. (b) Simulation results for the geometry indicated in (a) and used in the main experiments. For photons launched from the top (τ_{12}^{θ}, red line), as incident angle increases, transmission decreases from ~95% to 0%. On the other hand, for photons launched from the bottom (τ_{21}^{θ}, blue line), as incident angle increase, transmission increases from 0% to ~35%.

In order to guide the design of the experimental test section, we simulated the scattering of photons by asymmetric pyramidal structures using a ray tracing scheme in a three dimensional domain [11, 26]. Figure 4-5 (a) shows the geometry used in the main work, which was crudely optimized using a phenomenological drifted Bose-Einstein model of the thermal collimator [11, 26]. The chosen structure is a double layer of pyramidal arrays. Each layer is a "checkerboard" array, and the first layer is staggered

with respect to the second layer. Each pyramid is treated as perfectly specular, and has an aspect ratio (AR) of 3:1 (height:base). The gap between the tips of the lower layer and the bases of the upper layer is equal to one-half of the base of a pyramid. To improve the computational efficiency, we define our ray-tracing simulation domain using a unit cell (indicated using black dashed lines) by considering the mirror symmetries of the staggered pyramidal arrays. For each polar angle ($\Delta\theta$ mesh of 1 deg.), the transmission coefficient is averaged over 9604 photon trials, in which the x-y position and azimuthal angle φ are randomized with uniform distribution using a Monte Carlo (MC) scheme. Figure 4-5(b) shows the results, with 95% confidence intervals in τ estimated as <1% for all θ. For transport towards the peaks (τ_{12}^{θ}, red line), photons of near-normal incidence (θ = 0°) are largely transmitted, while photons incident from oblique angles are largely reflected. For transport towards the bases (τ_{21}^{θ}, blue line), on the other hand, photons from $\theta = 0°$ are entirely reflected, and photons incident from oblique angles have higher transmission.

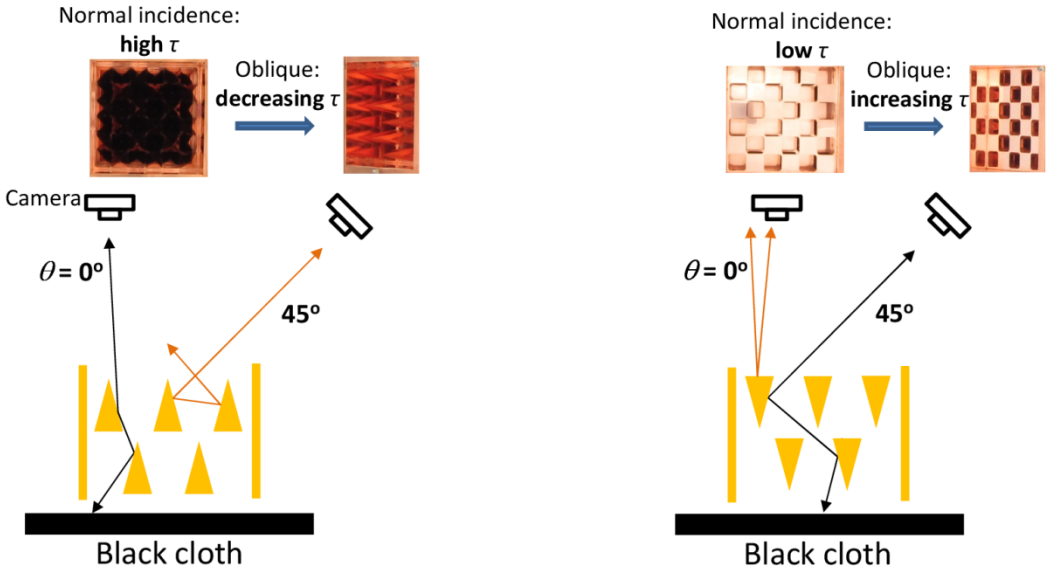

a, View towards points (τ_{12}^{θ}) **b,** View towards bases (τ_{21}^{θ})

Figure 4-6. Visualization to confirm the function of the pyramidal test section. The surrounding environment is white (not shown), and the camera exposure time is the same for all images. (a) View towards points. Mostly black from $\theta = 0°$, indicating high transmission, while much less black from $\theta = 45°$, indicating lower transmission. (b) View towards bases. Mostly shiny from $\theta = 0°$, indicating low transmission, while much more black from $\theta = 45°$, indicating higher transmission.

Our pyramidal test section is designed according to these simulation results. To qualitatively confirm the as-fabricated test section meets its core function of having very different angle-dependent transmission coefficients from its two ends, we imaged the test section from various angles using visible light and a consumer-grade digital camera. This

is a conservative check, since IR has a longer wavelength than visible light, and thus for fixed surface roughness it will perceive the pyramids as being more specular. In addition, the intrinsic reflectivity of copper in the IR is also higher than in the visible [16]. As shown in Fig. 4-6 (a), we first cover the backside of the test section with a black cloth, and place it in a large environment that is otherwise white. The front side of the test section is then imaged with a digital camera located around 25" away (corresponding to a small solid angle of 0.010 sr) with two different angles: normal ($\theta = 0^o$) and oblique ($\theta = 45^o$). The camera exposure time is the same for all four scenarios. For the configuration with pyramid peaks pointing away from the black cloth [Fig. 4-6(a)], the view from $\theta = 0^o$ is almost totally black, indicating the large majority of photons incident from this direction are transmitted through to the black cloth. On the other hand, the image from $\theta = 45^o$ shows much less black, indicating that most photons incident from 45° are reflected. The observations for the configuration with pyramid peaks pointing down towards the black cloth [Fig. 4-6 (b)] are opposite: the photographs are mostly shiny from $\theta = 0^o$, indicating low transmission, and much more black from $\theta = 45^o$ (higher transmission). The trends of this semi-quantitative experiment are consistent with the ray tracing results of Fig. 4-5(b) and confirm that the transmission functions of the fabricated test section indeed have the required angular dependencies.

4.5.3 Nonlinearity of the thermal transport

We emphasize that a static angle-dependence in $\varepsilon(\theta)$, no matter how sharply peaked [27], cannot lead to thermal rectification. This is a direct consequence of the 2nd Law requirement for no net transport at thermal equilibrium, and has been demonstrated theoretically by ourselves [11] and others [12]. For example, using a Landauer-Büttiker framework the effect of the emissivities $\varepsilon_1(\theta)$ and $\varepsilon_2(\theta)$ can be incorporated into effective τ_{12}^{θ} and τ_{12}^{θ} functions and the reservoirs treated as black, and in this case analysis like Eq. (4-4) has already established that rectification is not possible without some additional nonlinearity. Indeed, the key is to introduce some additional bias dependence as well. In our work this is realized through the thermal collimator.

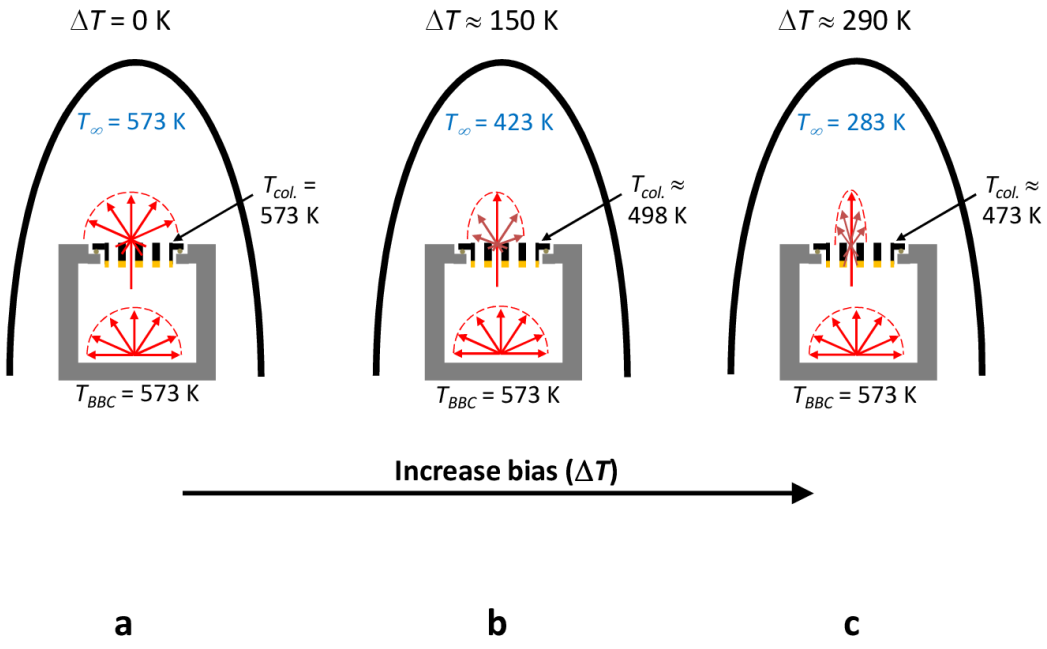

Figure 4-7. Conceptual evolution of the weighting function, $w(\theta)$. (a) Zero bias (ΔT = 0 K): the whole system is in equilibrium at 573 K, so that w does not depend on θ. (b) Moderate bias (ΔT = 150 K): the temperature of collimator, $T_{col.}$, is lower than that of BBC, T_{BBC}, so that w is somewhat distorted. (c) large bias (ΔT = 290 K; this corresponds to the main experiments): $T_{col.}$ is further reduced relative to T_{BBC}, so that w is further distorted.

Figure 4-7 depicts the evolution of the distortions in the weighting function, $w(\theta)$, caused by increasing ΔT. For simplicity here we imagine the graphite of the collimator to be perfectly black; allowing for $\varepsilon_{graphite} < 1$ does not change the major trends. We fix T_{BBC} = 573 K for all three scenarios, but vary the temperature of the surroundings (T_∞), and thus the bias (ΔT). At zero bias (ΔT = 0 K) as depicted in Fig. 4-7 (a), the whole system is in equilibrium and so the temperature of the graphite collimator ($T_{col.}$) is also at 573 K. Thus, the combined effect of BBC + collimator is to emit photons into the pyramid test section with an isotropic Lambertian distribution, characterized by a radiation temperature of 573 K at all angles. For non-zero bias [Fig. 4-7(b) & (c)] however, $T_{col.} < T_{BBC}$. Now, due to the open holes in the collimator, for angles close to $\theta \approx 0°$ many of the photons entering the pyramid test section were emitted from the BBC core at T_{BBC}. But photons at oblique angles are much more likely to have been emitted from the internal cylindrical surfaces of the collimator holes, with lower intensity since $T_{col} < T_{BBC}$. Thus, the photons have a distribution distorted away from Lambertian after passing through the collimator. The higher the bias, the more distorted the distribution.

4.5.4 A semi-quantitative guideline to optimize the thermal collimator

An accurate model for the non-equilibrium collimator is desired but challenging. Instead here we describe a semi-quantitative argument about the maximization of the

thermal rectification, γ, with respect to the ratio D/h, where D and h are the hole diameter and the thickness of the collimator, respectively. In the spirit of distorting the distribution function as depicted in Fig. 4-7, we can conclude that γ vanishes when D/h reaches either 0 or ∞, so the best rectification must occur for some intermediate value of D/h. As described next, a semi-quantitative guideline for the optimal ratio is $(D/h)_{opt.} \approx \tan(\theta_c)$, where θ_c is the angle at which the Fwd and Rev transmission curves cross. For example, for the pyramidal test section used in this experiment we estimate $\theta_c \approx 40$ degrees based on the crossing seen in Fig. 4-5(b).

To obtain this guideline, we invoke the physical picture depicted in Fig. 4-1(a) of the main text: to transmit through the pyramidal test section, Fwd bias favors photons with small incident angles while Rev bias favors photons with large incident angles. We fix the total open-area fraction of the collimator. For the approximate range $0 < D/h < \tan(\theta_c)$, increasing D/h gradually increases the number of hot photons launched directly from the BBC while decreasing the number of cooler photons launched from the collimator. In this regime, these hot photons have small incident angles and thus most are transmitted under Fwd bias but blocked under Rev bias, leading to a significant increase of $Q_{Fwd.}$ but only a slight increase of $Q_{Rev.}$. The overall result is that increasing D/h in this regime thus increases γ. Continuing to $\tan(\theta_c) < D/h < \infty$, increasing D/h further increases the total number of hot photons emitted directly from the BBC. In this regime, however, the additional hot photons have much larger incident angles, most of which are now blocked under Fwd bias but transmitted under Rev bias. This leads to a saturation of $Q_{Fwd.}$ but a significant increase of $Q_{Rev.}$, and thus further increases of D/h cause a decrease of γ. Combining these two regimes, we conclude $(D/h)_{opt.} \approx \tan(\theta_c)$.

Following this argument, we designed our collimator with $D/h = 1$, which is expected to be reasonably well-matched to the value of $\tan(\theta_c) \approx 0.84$ for the pyramidal test section [Fig. 4-5(b)]. This collimator resulted in $\gamma = 10.9\%$, as shown in Fig. 4-3(c) of the main text using filled columns. To test the basic trend of the collimator optimization argument just given, we also measured a second collimator with a smaller $D/h = 0.5$, expected to give inferior rectification. As indicated by the striped columns in Fig. 4-3(c), this Col. 2 indeed resulted in weaker rectification, in this case $\gamma = 4.1\%$. Further support of the basic collimator argument comes from the fact that as compared to Col. 2, the better-optimized Col. 1 significantly increases $Q_{Fwd.}$ while only slightly increasing $Q_{Rev.}$ [Fig. 4-3(c)], consistent with our prediction for the regime $0 < D/h < \tan(\theta_c)$ above.

4.5.5 Lumped cooling model

We explain the lumped cooling model used to develop Eqs. (4-2) and (4-3) of the main text. The lumped cooling problem is the thermal-domain analogy of discharging an electrical RC circuit. The Biot number during the cooling process is estimated to be < 0.01, making the lumped cooling model a good approximation [28]. The basic energy balance on the dashed control volume in Fig. 4-2(b) of the main text yields

$$C_{BBC}\frac{dT_{BBC}}{dt} = P_{BBC} + Q_{BBC-G} - Q_{diode}, \tag{4-5}$$

where C_{BBC} is the thermal capacitance of the BBC estimated from geometry and handbook data, and $P_{BBC} = [I \cdot V]_{\mathrm{BBC}}$ is the electrical power delivered to the BBC. We follow a standard radiation resistor analysis[25], where the driving potential is σT^4 with σ as the Stefan-Boltzmann constant, and resistances carry units of m^{-2}. Thus,

$$Q_{BBC-G} = \left(\sigma T_G^4 - \sigma T_{BBC}^4\right) \Big/ R_{BBC-G} \tag{4-6}$$

is the heat transfer from BBC to guard, and

$$Q_{diode} = \left(\sigma T_{BBC}^4 - \sigma T_\infty^4\right) \Big/ R_{diode} \tag{4-7}$$

is the heat transfer through the test section.

The measurements reported in the main text are obtained as follows. After the whole system stabilizes with $T_{BBC} = T_G = 573$ K (typically 12 hours), we turn off the heaters of the BBC at time $t = 0$ ($P_{BBC} = 0$ for $t > 0$) while maintaining the guard at 573 K [Fig. 4-2(c) of the main text]. Now the energy balance on the BBC simplifies to

$$C_{BBC}\frac{dT_{BBC}}{dt} = \frac{\sigma T_G^4 - \sigma T_{BBC}^4}{R_{BBC-G}} - \frac{\sigma T_{BBC}^4 - \sigma T_\infty^4}{R_{diode}}. \tag{4-8}$$

In the perfect-shield limit ($Q_{BBC-G} \big/ Q_{diode} << 1$, checked below), this further reduces to

$$C_{BBC}\frac{dT_{BBC}}{dt} = -\frac{\sigma T_{BBC}^4 - \sigma T_\infty^4}{R_{diode}}. \tag{4-9}$$

After separating variables and integrating, we obtain a closed-form solution to Eq. (4-9), albeit for $t(T_{BBC})$:

$$t = \frac{R_{diode} C_{BBC}}{4\sigma T_\infty^3}\left[f\left(T_{BBC}(t)\right) - f\left(T_{BBC,0}\right)\right], \tag{4-10}$$

where $f(x) = \ln\left(\dfrac{x + T_\infty}{x - T_\infty}\right) + 2\tan^{-1}\left(\dfrac{x}{T_\infty}\right)$.

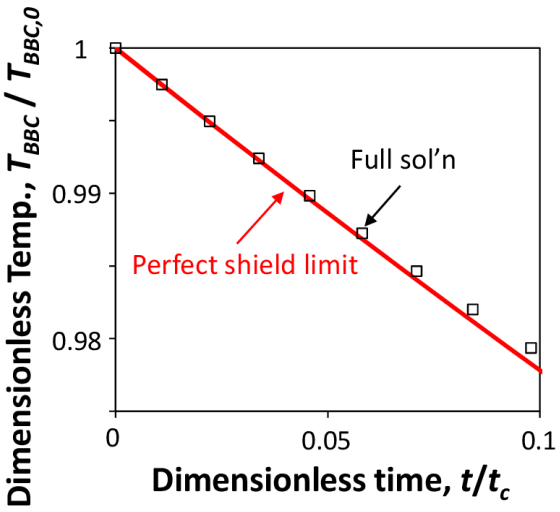

Figure 4-8. Comparing the solution from the perfect shield limit to the full solution of the lumped cooling model. Using realistic parameters, the difference between the perfect shield limit of Eq. (4-10) and the full numerical solution of Eq. (4-8) is estimated to be less than 0.1% over the typical experimental regime $t/t_c < 0.1$, where $t_c \sim 7$ hours (see text).

We first compare this perfect shield limit [Eq. (4-10)] to the full numerical solution of Eq. (4-8). In this calculation we use the following realistic parameters: C_{BBC} = 1700 J/K, $R_{BBC\text{-}G}$ = 600 m^{-2}, and R_{diode} = 640 m^{-2}. Here C_{BBC} is estimated based the BBC's geometry and specific heat capacity[16] averaged over the experimental regime, $R_{BBC\text{-}G}$ is extracted from full-time cooling curves beyond the perfect shield limit, and R_{diode} is averaged over the experimentally extracted Fwd and Rev resistances. In Fig. 4-8, we plot the dimensionless temperature, $\hat{T}_{BBC} = T_{BBC}/T_{BBC,0}$, as a function of a dimensionless time, $\hat{t} = t/t_c$, where $t_c = C_{BBC}R_{diode}/\left(4\sigma T_{BBC,0}^3\right)$ is estimated to be ~7 hours. Within the time regime of the real experiment ($t/t_c < 0.1$), the difference between the two solutions is less than 0.1%, corresponding to a maximum error of 0.55 K for 553 K < T_{BBC} < 573 K. This verifies that the perfect shield limit is appropriate for the experimental regime presented in the main text.

We next compare the cooling rate, $|dT_{BBC}/dt|$, predicted by this perfect shield limit to experiments. We treat R_{diode} as the only free parameter, and fit the experimental cooling curves to Eq. (4-9). As shown in Fig. 4-9(a) for the simplest scenario of no test section or collimator, the model fit (dashed lines) agrees with the experimental cooling rate (points) with maximum error of 1.5% from 553 K to 569 K. We consider this very good agreement. In addition, from the fitting result, R_{diode} = 266 m^{-2}, and based on the aperture area of (2.50")^2 and standard radiation analysis[25], we estimate the total hemispherical emissivity of the aperture to be 0.93, which is consistent with the BBC design value (>0.91) described in Appendices.

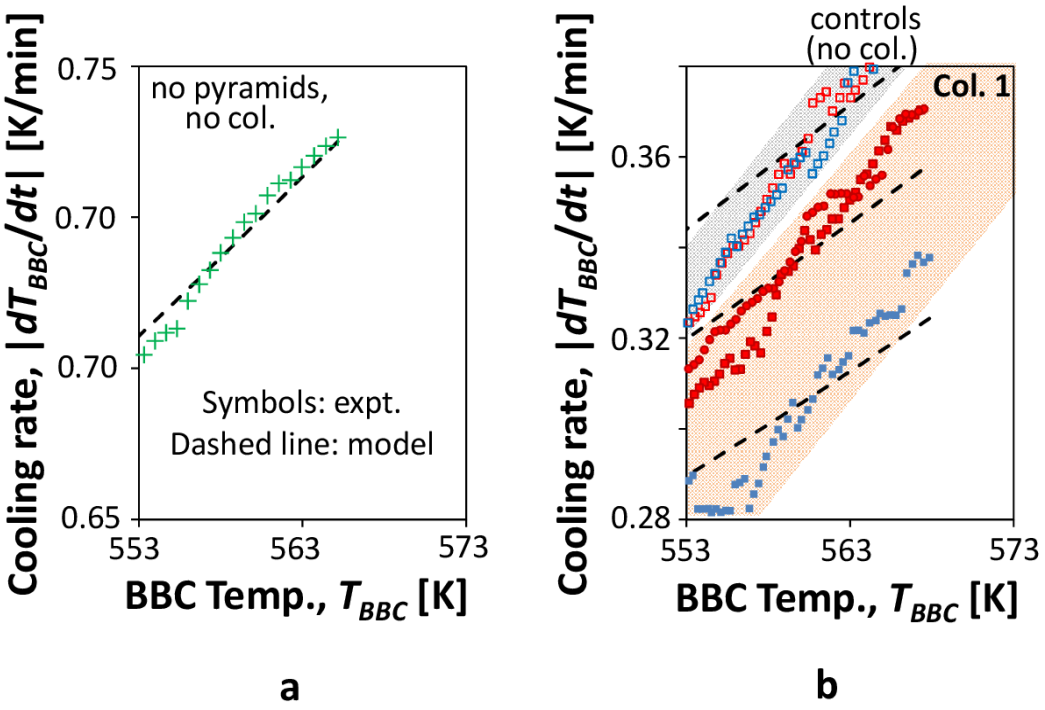

Figure 4-9. Comparing experimental results to the constant radiation resistor model. Each curve has one free parameter. (a) For the simplest scenario of no collimator or pyramidal test section, the model agrees with the experiment to within 1.5%. (b) For experiments involving the test section and collimator, this simple linear model explains the average magnitude of the experimental results. The slopes of b are in error but this may not be surprising considering the additional complexity and nonlinearity involved. For clarity we only fit three of the five cooling curves of Fig. 4-3(b) (see text).

Figure 4-9(b) shows a similar comparison of this model with the measurements from Fig. 4-3(b) of the main text. For clarity, instead of fitting all five of the cooling curves in Fig. 4-3(b), we only performed three fits: the reverse biased experiment, one of the two forward biased experiments, and likewise one of the two control experiments (no collimator). The fits again capture the leading order behavior $|dT_{BBC}/dt|$, but now deviate from the experiments in the higher order behavior $d(|dT/dt|) / dT$. Such deviations may not be surprising considering the additional complexity and nonlinearity introduced by the collimator and test section. We emphasize that in Fig. 4-3(c) of the main text the diode power is calculated using Eq. (4-2) which directly averages the experimental cooling rate in Fig. 3 (b) from 569 K to 553 K, and does not invoke Eq. (4-9). Thus the fact that Eq. (4-9) deviates from the experiment in Fig. 4-9(b) has no effect on the results in Fig. 4-3(c).

4.5.6 Further verification of the need for a thermal collimator: An experiment on phonons in an etched silicon on insultator (SOI) wafer

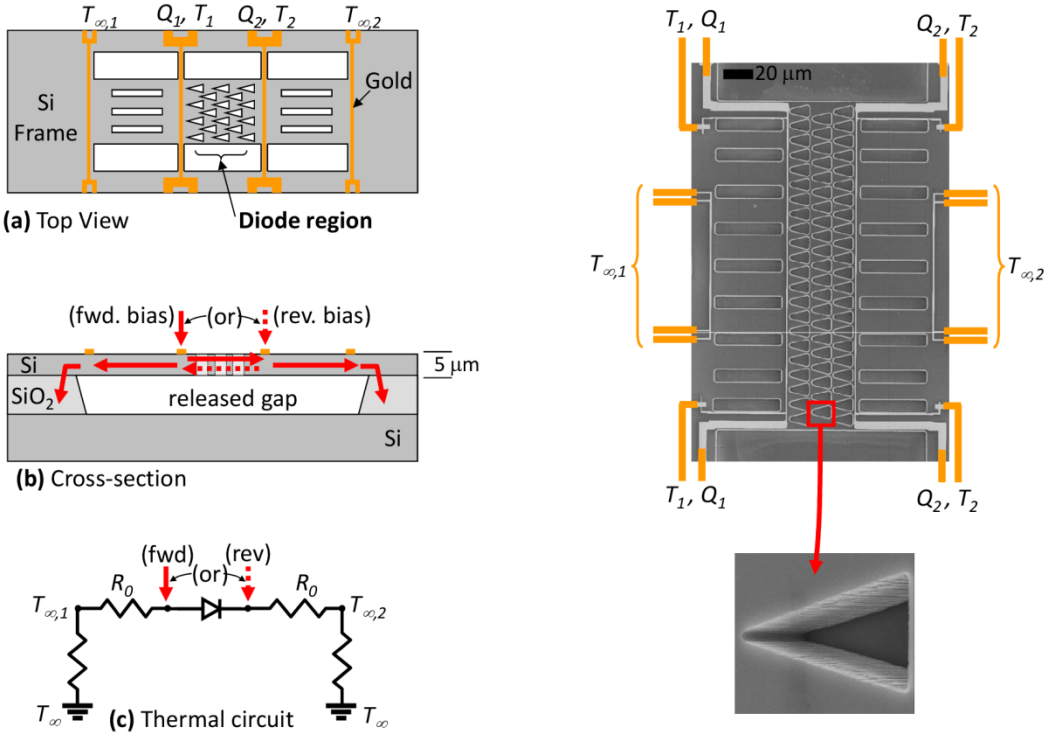

Figure 4-10. An experiment to study thermal rectification of phonons by asymmetric microfabricated pores. Left: Concept and thermal circuit. Right: A fabricated structure (by Dr. Wanyoung Jang). Since this structure lacks a thermal collimator, no rectification is expected.

The success of the *photon* thermal diode reported in the main text builds on lessons learned from an earlier study of ballistic *phonons* in etched SOI. This previous experiment lacked an effective thermal collimator and thus is expected to be unable to provide rectification. Here we briefly summarize this experiment and its main result.

We attempted several variations of the basic concept illustrated in Fig. 4-10. The central test section (between T_1 and T_2 in the figure) contains a ballistic thermal diode made by etching asymmetric triangular pores in the device layer of an SOI wafer. The central test section was then undercut by a selective wet etch to release it from the substrate, for thermal isolation. The experiments were conducted in high vacuum to eliminate convection, and radiation losses were also negligible. Temperatures as low as 10 K were used to maximize the mean free paths (MFPs) of the phonons in Si and ensure ballistic transport. Gold lines were used as heaters and resistance thermometers. All samples were patterned using e-beam lithography.

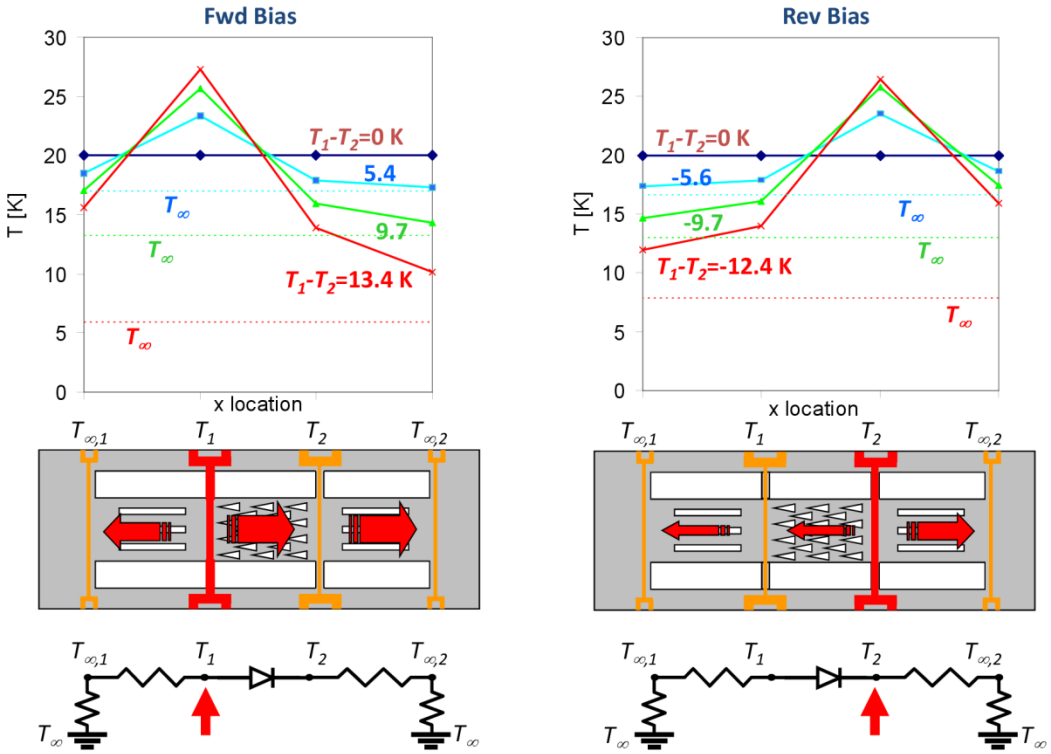

Figure 4-11. Attempted phonon thermal rectification: typical experimental data in forward and reverse bias (left and right columns, respectively). Top: Measurements. Bottom: Corresponding schematics. In each experiment the test section (diode region) is between the points labeled T_1 and T_2. The average temperature was fixed at 20 K, while 4 different thermal biases were applied: $\Delta T \approx \pm$(0, 5.5, 9.7, and 13) K. Rectification corresponds to $(T_2\text{-}T_{\infty,2})_{Fwd} > (T_1\text{-}T_{\infty,1})_{Rev}$. Because the two plots are basically mirror images of each other, there is no clear rectification above the noise threshold. This null result confirms that rectification is not possible without a thermal collimator.

Typical measurement results are shown in Fig. 4-11. The plots show measured temperature at the four positions indicated from left to right as $T_{\infty,1}$, T_1, T_2, and $T_{\infty,2}$. The thermal diode is in the central section between T_1 and T_2. The etched slots between $T_{\infty,1}$ and T_1, and between T_2 and $T_{\infty,2}$, are as symmetric as possible and used to increase the thermal resistance R_0 to be comparable to the expected R_{diode}. In each experiment in this example, the average temperature $\frac{1}{2}(T_1+T_2)$ was held constant at 20 K, while several thermal biases (T_1-T_2) were applied. This required simultaneous tuning of two independent inputs: the background temperature of the cryostat's cold finger, T_∞ (which is different from $T_{\infty,1}$ and $T_{\infty,2}$), and the Joule heating at the hot-side of the device (Q_1 in forward bias, and Q_2 in reverse bias). We used an iterative secant method to optimize both input parameters simultaneously during the experiment.

The raw data in Fig. 4-11 can be understood by considering the different heat flows through the test section in forward and reverse bias. As indicated in the schematics, to maintain the same magnitude of $|\Delta T|=|T_1\text{-}T_2|$, more heat should flow through the

central diode section in forward bias than in reverse bias. In forward bias, this heat must then flow through the neighboring region from the location T_2 to the location $T_{\infty,2}$. In reverse bias, on the other hand, the heat flow exiting the diode section must then flow from $T_1 \rightarrow T_{\infty,1}$. Therefore, when holding $|T_1\text{-}T_2|$ constant but reversing thermal polarity (as in the experiments of Fig. S8), the signature of thermal rectification is $(T_2\text{-}T_{\infty,2})_{\text{Fwd}} > (T_1\text{-}T_{\infty,1})_{\text{Rev}}$. Inspection of the measurements in Fig. 4-11 indicate that no such rectification was evident, because for any given ΔT the measured $(T_2\text{-}T_{\infty,2})_{\text{Fwd}} \approx (T_1\text{-}T_{\infty,1})_{\text{Rev}}$ to within experimental uncertainty. Thus we conclude that the experiment depicted in Fig. 4-11 again confirms one of the key conclusions of the main text: ballistic thermal rectification is not possible through asymmetry alone.

Several other configurations were tried with different temperature ranges, structures, and configurations, including an "H-bridge" concept similar in spirit to what was used in the electrical analogue [8]. In all cases no rectification was detectable, consistent with expectations since there was no thermal collimator.

In light of the understanding developed in the main text, we identify two key issues which would need to be addressed to observe significant ballistic thermal rectification in a phonon system such as Fig. 4-10. First is the fact that calculations predict stronger rectification for specular rather than diffuse surfaces [11, 26]. The structures of Fig. 4-10 were prepared by reactive ion etching (RIE) and exhibit roughness which may not be negligible compared to the characteristic phonon wavelengths even at these low temperatures [29]. Smoother surfaces might be achievable by using focused ion beam (FIB) milling rather than RIE, reflowing Si using a high-temperature hydrogen anneal [30], or exploiting crystallographic anisotropy such the well-known 111 stop planes of KOH-etched Si. The second issue is more fundamental: the need for effective thermal collimation. The experiments of Fig. 4-11 were performed at low temperatures to ensure ballistic phonon transport and specular reflections, but this also quenches the inelastic (umklapp) phonon scattering and thus there is no nonlinearity analogous to the mechanism of Fig. 4-7. We emphasize that strategies based on simply etching slots into the SOI film cannot function as a thermal collimator for phonons, because phonon-surface scattering is elastic and thus linear. In contrast, the photon thermal collimator of the main text involves highly inelastic interactions between the photons and the graphite, which is one of the main advantages of the photon approach for this first demonstration.

4.6 References

[1] S. Chu and A. Majumdar, Nature **488**, 294 (2012).

[2] C. W. Chang, D. Okawa, A. Majumdar, and A. Zettl, Science **314**, 1121 (2006).

[3] C. Dames, Journal of Heat Transfer **131**, 061301 (2009).

[4] A. Jeżowski and J. Rafalowicz, physica status solidi (a) **47**, 229 (1978).

[5] N. A. Roberts and D. G. Walker, International Journal of Thermal Sciences **50**, 648 (2011).

[6] C. R. Otey, W. T. Lau, and S. Fan, Physical Review Letters **104**, 154301 (2010).

[7] L. P. Wang and Z. M. Zhang, Nanoscale and Microscale Thermophysical Engineering **17**, 337 (2013).

[8] A. M. Song, A. Lorke, A. Kriele, J. P. Kotthaus, W. Wegscheider, and M. Bichler, Physical Review Letters **80**, 3831 (1998).

[9] S. Saha, L. Shi, and R. S. Prasher, in *2006 ASME International Mechanical Engineering Congress and Exposition*, Chicago, Illinois, 2006).

[10] N. A. Roberts and D. G. Walker, in *ITherm 2008*, 2008).

[11] J. Miller, W. Jang, and C. Dames, in *2009 ASME Summer Heat Transfer Conference*, San Francisco, 2009).

[12] A. A. Maznev, A. G. Every, and O. B. Wright, Wave Motion **50**, 776 (2013).

[13] S. Markus, M. Judith, S. Elke, and L. Paul, New Journal of Physics **13**, 113027 (2011).

[14] J. Chaves, *Introduction to Nonimaging Optics* (CRC Press, 2008).

[15] J. H. L. IV and J. H. L. V, *A Heat Transfer Textbook* (Phlogiston Press, 2003).

[16] Y. S. Touloukian, *Thermophysical Properties of Matter* (IFI/Plenum, New York, 1970-1979).

[17] T. C. Harman, P. J. Taylor, D. L. Spears, and M. P. Walsh, Journal of Electronic Materials **29**, L1 (2000).

[18] F. M. Ross, J. Tersoff, and M. C. Reuter, Physical Review Letters **95**, 146104 (2005).

[19] P. Horowitz and W. Hill, *The Art of Electronics* (Cambridge University Press, 1989).

[20] Y. Yan and J. A. Malen, Energy & Environmental Science **6**, 1267 (2013).

[21] S. Varga, A. C. Oliveira, and C. F. Afonso, Energy and Buildings **34**, 227 (2002).

[22] N. Li, J. Ren, L. Wang, G. Zhang, P. Hänggi, and B. Li, Reviews of Modern Physics **84**, 1045 (2012).

[23] R. E. Bedford, *Calculation of Effective Emissivities of Cavity Sources of Thermal Radiation*, New York, 1988).

[24] G. Neuer, Quantitative InfraRed Thermography **27**, 359 (1992).

[25] M. F. Modest, *Radiative Heat Transfer* (McGraw-Hill, New York, 1993).

[26] J. Miller, University of California, Riverside, 2009.

[27] E. Rousseau, A. Siria, G. Jourdan, S. Volz, F. Comin, J. Chevrier, and J.-J. Greffet, Nat Photon **3**, 514 (2009).

[28] J. H. Lienhard and J. H. Lienhard, *A Heat Transfer Textbook* (Phlogiston Press, 2003).

[29] C. Dames and G. Chen, *Thermal Conductivity of Nanostructured Thermoelectric Materials* (Taylor & Francis, New York, 2006).

[30] Thareja, Kant, Howe, and Nishi, in *Mat. Res. Soc. Spring Meeting*, San Francisco, California, 2009).

Chapter 5: Summary and outlook

5.1 Summary

We summarize the contributions of this thesis as following:

Chapter 2 measured the thermal properties of graphene encased by silicon dioxide layers, a structure most relevant to microelectronics applications. A heat spreader + FEM method was developed to measure the thermal conductivity. This method was first validated by two control experiments. The first control omitted graphene from the basic stack. The extracted thermal conductivity of silicon dioxide layer agreed to better than 1% with a separate measurement using a 3ω method. The second control used a Pt thin film to mimic graphene. The extracted thermal conductivity of Pt agreed to better than 5% with a separate measurement combining a four-probe resistivity measurement and the Wiedemann-Franz law. We then measured the thermal conductivity of encased graphene as a function of both temperature and the number of graphene layers. These results showed that the thermal conductivity of single-layer-graphene was suppressed below 160 W/m-K at room temperature, while the thermal conductivity of our thickest samples approached that of bulk graphite. We also developed a phenomenological model to capture the physics.

Chapter 2 also measured the thermal contact resistance between graphene and silicon dioxide using a differential 3ω method. Our experiments showed that this thermal contact is significantly better than those contacts involving related carbon systems, which encourages possible future applications of graphene in microelectronics, interconnects, and thermal management structures. In addition, we applied a Bloch- Grüneisen formula to calibrate the resistance thermometer, which improves the accuracy of the experiment. We also applied a Monte Carlo scheme for uncertainty analysis, which relaxes the constraints on the traditional partial derivative method, and is a good option for nonlinear and complicated expressions.

Chapter 3 dealt with heat transfer in anisotropic materials. The first Brillouin zone and the iso-energy surfaces of the Debye dispersion relation are both generalized from spherical to ellipsoidal. This model is checked by comparison with the experimental specific heat capacity of graphite and HDPE, as well as the phonon irradiation of graphite calculated from lattice dynamics. The anisotropic TBC model performs at least six times better than the standard isotropic diffuse mismatch model at explaining the measured TBC between graphite and various metals [1]. The model further reveals an unexpected guideline to engineer the TBC: due to phonon focusing effects, in many cases the TBC across an interface can be increased by reducing a phonon velocity component parallel to the plane of the interface.

Chapter 4 experimentally demonstrated a photon thermal diode. The device is based on a new mechanism exploiting asymmetric scattering of ballistic energy carriers by pyramidal reflectors. Control experiments verify recent theoretical predictions that this mechanism also requires a non-linear thermal collimator element, due to a deep requirement of the 2nd Law of Thermodynamics (equivalent to conservation of optical

etendue). Experiments confirm both effects: With pyramids and collimator the thermal rectification is 10.9 ± 0.8%, while without the collimator no rectification is detectable (< 0.3%). This experiment is the first demonstration of a photon thermal diode, regardless of mechanism; and the first demonstration of the ballistic thermal rectification mechanism, regardless of energy carrier type.

5.2 Outlook

We list below several points that may be worth further investigation in the future:

A. Diffusive-ballistic heat transport in graphene

As proposed in Fig. 1-2(c), it would be interesting to observe the diffusive-ballistic transition by varying the length of graphene flakes. Recent measurements [2] of graphene nano ribbons supported by a substrate show this crossover by varying both the length and width of samples, although the quenching effect of the silicon dioxide supporting layer obscures the physical picture. In addition, it's not consistent to show ballistic effect using a pure diffusive FEM model. In order to show a clean physical picture, it's desirable to measure a freely suspended sample despite of the challenges in microfabrication and in cleaning the sample [3]. A framework based Boltzmann transport equation, instead of the classical diffusion equation is preferred in extracting the thermal conductivity from experimental raw data.

B. Kinetic theory for anisotropic systems

A general framework is developed in Chapter 3 to model the specific heat and thermal boundary conductance of anisotropic materials. The next step is to incorporate different scattering mechanisms (see Fig. 1-4) to model the thermal conductivity. An interesting starting point may be the so-called minimum thermal conductivity model [4]. It is hoped that after considering the anisotropy of the materials, this model can be brought back to serve as the lower bound of experimental results, thus resolving the recent mystery of the highly anisotropic WSe_2 system [5]. A long-term objective is to finally build up a kinetic theory for anisotropic systems, in which a key challenge is to model the direction dependent mean free path, and to incorporate it with the direction dependent phonon group velocity.

C. Thermal transistors

A *passive* photon thermal diode is experimentally demonstrated in Chapter 4. The next objective may be an *active* nonlinear thermal element, for example a thermal transistor. One promising mechanism is the metal-insulator-transition (MIT) of VO_2 [6]. We can directly apply thermal gate to transition between metal and insulator phases, thus switching between high-low (thermal) conducting states with a rectification effect up to 28% [7]. We can also apply electrical gate to modulate the oxygen vacancies in VO_2 [8], and thus the MIT point and thermal conductivity.

5.3 References

[1] A. J. Schmidt, K. C. Collins, A. J. Minnich, and G. Chen, J. Appl. Phys. **107**, 104907 (2010).

[2] M.-H. Bae et al., Ballistic to diffusive crossover of heat flow in graphene ribbons., Nat. Commun. 4, 1734 (2013).

[3] Jang, W. et al., Thermal conductivity of suspended few-layer graphene by a modified T-bridge method ., Applied Physics Letters, **103**, 133102 (2013).

[4] D. Cahill, S. Watson, R. Pohl, Lower limit to the thermal conductivity of disordered crystals., *Phys. Rev. B. Condens. Matter* **46**, 6131–6140 (1992).

[5] C. Chiritescu *et al.*, Ultralow thermal conductivity in disordered, layered WSe2 crystals., *Science* **315**, 351–3 (2007).

[6] F. J. Morin, Oxides Which Show a Metal-to-Insulator Transition at the Neel Temperature, *Phys. Rev. Lett.* **3**, 34–36 (1959).

[7] J. Zhu et al., Temperature gated thermal rectifier for active heat flow control., arXiv:1307.4069.

[8] J. Jeong *et al.*, Suppression of metal-insulator transition in VO2 by electric field-induced oxygen vacancy formation., *Science* **339**, 1402–5 (2013).